

# Multi-scale Modeling of Rechargeable Ion Batteries

by

Ajaykrishna Ramasubramanian  
B.S. Amrita University, 2014

THESIS

Submitted as partial fulfillment of the requirements  
for the degree of Doctor of Philosophy in Mechanical Engineering  
in the Graduate College of the  
University of Illinois at Chicago, 2020

Chicago, Illinois

Defense Committee:

Prof. Farzad Mashayek, Chair and Advisor

Prof. Vitaliy R. Yurkiv, Co-advisor

Prof. Reza Shahbazian-Yassar

Prof. Arunkumar Subramanian

Prof. Ali Khounsary, Illinois Institute of Technology

## ACKNOWLEDGMENTS

Firstly, I would like to express my sincere gratitude to my advisors Prof. Farzad Mashayek and Dr. Vitaliy Yurkiv for their continuous support during my Ph.D. study and related research. Their guidance helped me throughout the research and also in writing this thesis. I could not have imagined having better advisors and mentors for my Ph.D. study.

Besides my advisors, I would like to thank the rest of my thesis committee, for their insightful comments and encouragement throughout my research which incited me to widen my research from various perspectives. I would also like to thank my fellow lab mates for the stimulating discussions, the sleepless nights we were working together before deadlines, and for all the fun we have had in the last four years.

Last but not the least, I would like to thank my family: my parents and my brother for supporting me spiritually throughout writing this thesis and my life in general.

Ajaykrishna Ramasubramanian

## CONTRIBUTION OF AUTHORS

**Chapter 2** provides an overview of the modeling framework used in Chapter 3 and Chapter 4.

**Chapter 3** represents two published papers (Ramasubramanian, A., Yurkiv, V., Najafi, A., Khounsary, A., Shahbazian-Yassar, R., Mashayek, F. “A Comparative Study on Continuum-Scale Modeling of Elasto-Plastic Deformation in Rechargeable Ion Batteries”, *J. Electrochem. Soc.*, 2017, 164 (13), A3418–A3425.) and (Ramasubramanian, A., Yurkiv, V., Nie, A., Najafi, A., Khounsary, A., Shahbazian-Yassar, R., Mashayek, F. “A Numerical Study on Striped Lithiation of Tin Oxide Anodes”, *Int. J. Solids Struct.*, 2019, 159, 163–170.) in which I am the first author. Dr. Farzad Mashayek and Dr. Vitaliy Yurkiv supervised the research and assisted with writing and reviewing the manuscripts. Dr. Reza Shahbazian-Yassar leads the experimental group and Dr. Reza Shahbazian-Yassar and Dr. Anmin Nie provided the TEM measurements for the experimental comparison and validation of the modeling framework. Dr. Ali Najafi and Dr. Ali Khounsary assisted with writing and reviewing the manuscripts. I contributed to implementing and testing of the modeling framework, running the numerical examples capturing the Li diffusion mechanisms and writing the manuscripts.

**Chapter 4** represents a published paper (Ramasubramanian, A., Yurkiv, V., Foroozan, T., Ragone, M., Shahbazian-Yassar, R., Mashayek, F., “Lithium Diffusion Mechanism through Solid-Electrolyte Interphase (SEI) In Rechargeable Lithium Batteries”, *J. Phys. Chem. C*, 2019.) and a paper under consideration (Ramasubramanian, A., Yurkiv, V., Foroozan, T.,

## CONTRIBUTION OF AUTHORS (Continued)

Ragone, M., Shahbazian-Yassar, R., Mashayek, F., “Stability of SEI on Lithium Metal Surface on Lithium Metal Batteries (LMBS)”, *Electrochimica Acta*, Under Review) in which I am the first author. Dr. Farzad Mashayek and Dr. Vitaliy Yurkiv supervised the research and assisted with writing and reviewing the manuscripts. All the other co-authors provided assistance in writing and reviewing the manuscript. I contributed to performing the density functional theory calculations for the Li diffusion coefficients through SEI and the stability of triple-phase boundary structures. I also contributed in writing the manuscript.

## TABLE OF CONTENTS

<u>CHAPTER</u>		<u>PAGE</u>
<b>1</b>	<b>INTRODUCTION AND BACKGROUND . . . . .</b>	<b>1</b>
1.1	Introduction . . . . .	1
1.2	Motivation . . . . .	3
1.3	Rechargeable-ion Batteries – Degradation Phenomena . . . . .	6
1.4	Literature Overview . . . . .	8
1.4.1	Particle Scale . . . . .	8
1.4.2	Interphase Scale . . . . .	11
1.5	Scope and Organization of Thesis . . . . .	14
<b>2</b>	<b>COMPUTATIONAL METHODS AND METHODOLOGIES . . . . .</b>	<b>17</b>
2.1	Particle scale Modeling of Li-ion Battery Degradation . . . . .	17
2.1.1	Coupled Diffusion/Structure Mechanics Model . . . . .	18
2.1.2	Phase-Field Model . . . . .	21
2.2	Interphase Scale Modeling of Li-ion Battery Degradation . . . . .	24
2.2.1	Density Functional Theory . . . . .	24
<b>3</b>	<b>PARTICLE SCALE DEGRADATION STUDIES . . . . .</b>	<b>30</b>
3.1	Chemo-Mechanics of Li Insertion in Si Anodes . . . . .	30
3.1.1	Isotropic Lithiation of Si Nanowire . . . . .	31
3.1.1.1	Problem Definition and Parametrization . . . . .	32
3.1.1.2	Model Validation . . . . .	36
3.1.2	Model Comparison . . . . .	40
3.1.2.1	Discussion on Modeling Parameters . . . . .	41
3.1.2.2	Comparison of Model Accuracy and Physics . . . . .	44
3.1.2.3	Comparison of Models’ Ease of Use . . . . .	45
3.1.3	Model Extension - Anisotropic Swelling in Si . . . . .	46
3.2	Chemo-Mechanics of Li Insertion in SnO <sub>2</sub> Anodes . . . . .	50
3.2.1	Problem Definition and Parametrization . . . . .	51
3.2.2	Stress Induced Diffusion in SnO <sub>2</sub> Anodes . . . . .	58
3.2.3	Parametric Study . . . . .	62
3.2.3.1	Effect of $\kappa$ on Diffusion Coefficient . . . . .	62
3.2.3.2	Effect of the Distance Between the Stressed Zones . . . . .	64
3.3	Summary and Conclusions . . . . .	66
<b>4</b>	<b>INTERPHASE SCALE DEGRADATION STUDIES . . . . .</b>	<b>70</b>
4.1	Diffusion of Li Through SEI Grain Structures . . . . .	72
4.1.1	GB Creation . . . . .	72

## TABLE OF CONTENTS (Continued)

<u>CHAPTER</u>		<u>PAGE</u>
4.1.1.1	LiF/LiF GB Creation . . . . .	74
4.1.1.2	Li <sub>2</sub> O/Li <sub>2</sub> O GB Creation . . . . .	75
4.1.1.3	LiF/Li <sub>2</sub> O GB Creation . . . . .	77
4.1.2	Li Diffusion Through GB . . . . .	79
4.1.2.1	Li Diffusion Through LiF/LiF GB . . . . .	79
4.1.3	Li Diffusion Through Li <sub>2</sub> O/Li <sub>2</sub> O GB . . . . .	81
4.1.4	Li Diffusion Through LiF/Li <sub>2</sub> O GB . . . . .	82
4.2	Stability of SEI GB on the Li Surface . . . . .	84
4.2.1	LiF/Li <sub>2</sub> O GB on Li Surface . . . . .	86
4.2.2	Li <sub>2</sub> O/Li <sub>2</sub> O GB on Li Surface . . . . .	88
4.2.3	LiF/LiF GB on the Li Surface . . . . .	90
4.2.4	Stability of SEI Grain Structures on the Li Surface . . . . .	91
4.2.5	Excess Energy and Stability of TPB . . . . .	96
4.3	Summary and Conclusions . . . . .	98
<b>5</b>	<b>SUMMARY AND FUTURE WORKS . . . . .</b>	<b>100</b>
	<b>APPENDICES . . . . .</b>	<b>105</b>
	<b>Appendix A . . . . .</b>	<b>106</b>
	<b>Appendix B . . . . .</b>	<b>115</b>
	<b>Appendix C . . . . .</b>	<b>120</b>
	<b>CITED LITERATURE . . . . .</b>	<b>126</b>
	<b>VITA . . . . .</b>	<b>136</b>

## LIST OF TABLES

<u>TABLE</u>		<u>PAGE</u>
I	Simulation parameters with their dimensional and normalized values. . . . .	34
II	Qualitative comparison of the CDSM (implemented in ANSYS) and the PFM (implemented in MOOSE Framework). . . . .	46
III	Simulation parameters with their dimensional and normalized values. . . . .	57
IV	Surface orientations and surface energies of different SEI components . . . . .	73
V	Summary of all the GB structure properties. First column shows the GB composition and notation, second column shows the stoichiometry, third column lists k-point used in the present DFT calculations, fourth column shows the calculated GB energies, fifth column reports the GB density and the last sixth column reports the calculated bulk modulus . . . . .	78
VI	Summary of all activation energies and Diffusion coefficients . . .	85
VII	Binding energy based overpotential for different SEI grain structures on Li surface . . . . .	92
VIII	Surface orientations and GB energies of different SEI GB on Li surface . . . . .	97

## LIST OF FIGURES

<u>FIGURE</u>		<u>PAGE</u>
1	Schematic of a LIB with its components. Left – cross-section of cylindrical battery depicting layered structure, right – illustration of battery’s repeat unit (i.e., anode, electrolyte and cathode together with two current collectors). . . . .	3
2	Multiple scales of modeling for LIB. Interphase/atomistic scale – resolution to atom-atom interaction taking into account relativistic effects; Particle/surface scale – mean-field averaging at microscale and Cell/battery pack scale – continuum modeling with a purpose of system integration. . . . .	5
3	Schematic of particle scale and interphase scale modeling approaches.	6
4	Schematic illustration of the computational domain. . . . .	33
5	Concentration plots showing narrow reaction front of Si lithiation process and the respective geometries at four different times. (a) Results obtained with the PFM; (b) Results obtained by using the CDSM. Symbols are the data taken from [1] . . . . .	37
6	Stresses modeled in the radial direction at 10% lithiation (a–c) and 50% lithiation (d–f) progress, where (a) and (d) are Hoop stresses, (b) and (e) are radial stresses and (c) and (f) are von-Mises stresses. The solid lines depict the results from the CDSM elasto-plastic model and the dashed lines depict results from the PFM. All the stress components are normalized by Young’s modulus of Si, $E_{Si}$ . Symbols represent data from [1]. . . . .	38
7	Plastic strain plots at 10%, 30%, 50% and 80% lithiation. Results from (a) PFM and (b) CDSM models. Symbols are the data taken from [1]. . . . .	39
8	Equivalent plastic strain history in radial direction $r$ . . . . .	40
9	Comparison of the computational times of the CDSM and the PFM models. Both models are simulated with the same mesh structure on a single-core Intel Xeon 2.80 Ghz processor. . . . .	42
10	Variations of the normalized diffusivity coefficient Equation 2.1 for different values of the parameter $\alpha$ . . . . .	43
11	Variations of the chemical free energy (Equation 2.10) for different values of the parameter $\omega$ . . . . .	44
12	Lithium concentration distribution in (a) x and (b) y directions of the Si nanowire and (C) the respective geometries for three different times. . . . .	48

## LIST OF FIGURES (Continued)

<u>FIGURE</u>		<u>PAGE</u>
13	Radial, von-Mises and Hoop stresses measured in the direction R3-x and R3-y using CDSM framework at 10% ((a) and (c)) and 50% ((b) and (d)). All the stress components are normalized by Young's modulus of Si . . . . .	49
14	TEM image of lithiation in SnO <sub>2</sub> nanowire (NW), clearly showing the formation of striped diffusion regime followed by bulk diffusion with minimal contrast change on the surface of the NW. (a) shows the presence of surface carbon coating on pristine SnO <sub>2</sub> , (b) shows the initial diffusion through the striped region (long-range pipe diffusion) and (c) shows lithium diffusing through the bulk of the NW (short-range diffusion). . . . .	51
15	Schematic of initial and intermediate structures of striped diffusion during simulation. Geometrical changes are not to scale, merely for illustrative purpose. . . . .	53
16	Schematic representation of the 2D rectangular computational domain . . . . .	54
17	Simulation results showing concentration profile of Li diffusion along the SnO <sub>2</sub> nanowire for times 5 s, 350 s, 550 s and 950 s . . . . .	59
18	Stress evolution during lithiation of SnO <sub>2</sub> for 0%, 10%, 40% and 90% lithiation (times 5 s, 350 s, 550 s and 950 s). The values of stress are normalized using Young's modulus of elasticity . . . . .	60
19	The simulated strain development at the time of 350 s. The zoom-in insertion further highlights the bottom part of the nanowire shown in the left. . . . .	61
20	(a) Variation of the diffusivity with concentration for different values of parameter $\kappa$ . The underlined value of $\kappa$ is used in this work. (b) Variation of diffusivity with concentration and hydrostatic stress for $\kappa=0.36$ . . . . .	63
21	Concentration contours at 550s for different values of $\kappa$ : (a) $\kappa = 0$ (b) $\kappa = 0.33$ (c) $\kappa = 0.36$ . . . . .	64
22	Simulation results showing concentration (top panel) and hydrostatic stress (bottom panel) contours of Li diffusion along the SnO <sub>2</sub> nanowire at t=550 s for initial distances between stressed points (a) 75 nm (b) 37.5 nm and (c) 25 nm. The values of stress are normalized using Young's modulus of elasticity. . . . .	65
23	Schematic of SEI grain structures in LMBs and DFT analysis of diffusion pathways in SEI grain structure. . . . .	71

## LIST OF FIGURES (Continued)

<u>FIGURE</u>		<u>PAGE</u>
24	Grain boundary structures formed by LiF and Li <sub>2</sub> O grains. (a) Compact LiF/LiF (310) GB ( $\Sigma$ 3), (b) open LiF/LiF (310) GB ( $\Sigma$ 5). (c) Li <sub>2</sub> O/Li <sub>2</sub> O $\Sigma$ 3 GB with (111) oriented surface towards the interface, (d) Li <sub>2</sub> O/Li <sub>2</sub> O $\Sigma$ 15 GB with (210) surface. (e) LiF(001)/Li <sub>2</sub> O(111) GB structure. Pink colored spheres depict Li atoms, red colored spheres show F atoms, and red colored spheres illustrate O atoms. . . . .	76
25	a) Compact LiF/LiF (310) GB ( $\Sigma$ 3) with Li ad-atom (marked in blue). b) Open LiF/LiF (310) GB ( $\Sigma$ 5) with Li ad-atom (marked in blue). c) migration barrier for Compact LiF/LiF (310) GB ( $\Sigma$ 3). d) migration barrier for Compact LiF/LiF (310) GB ( $\Sigma$ 3). . . . .	80
26	a) Li <sub>2</sub> O/Li <sub>2</sub> O (210) GB ( $\Sigma$ 15) with Li ad-atom (marked in blue). b) diffusion direction and migration barrier for Li <sub>2</sub> O/Li <sub>2</sub> O (310) GB ( $\Sigma$ 15). . . . .	81
27	a) LiF/Li <sub>2</sub> O GB with Li ad-atom (marked in blue). b) c) Diffusion direction (path 1) and migration barrier for LiF/Li <sub>2</sub> O GB. d) Diffusion direction (path 2) and migration barrier for LiF/Li <sub>2</sub> O GB. e) Diffusion direction (path 3) and migration barrier for LiF/Li <sub>2</sub> O GB. . . . .	83
28	(a) Initial and final optimized structures of LiF/Li <sub>2</sub> O GB on Li surface with no added Li at the TPB, (b) Initial and final optimized structures of LiF/ Li <sub>2</sub> O GB on Li with added Li at TPB. Pink colored spheres depict Li atoms; red colored spheres show O atoms and green colored spheres show F atoms. The added Li atoms are shown in blue. . . . .	87
29	(a) Initial and final optimized structures of Li <sub>2</sub> O/Li <sub>2</sub> O GB on Li surface with no added Li atom at the TPB, (b) Initial and final optimized structures of Li <sub>2</sub> O/Li <sub>2</sub> O GB on Li with added Li at TPB, (c) Initial and final optimized structures of Li <sub>2</sub> O/Li <sub>2</sub> O GB on Li with added Li at other sites in the interface. Pink colored spheres depict Li atoms, and red-colored spheres show O atoms. The added Li atoms are shown in blue. . . . .	89
30	(a) Initial and final optimized structures of LiF/LiF GB on Li surface with no added Li at the TPB, (b) Initial and final optimized structures of LiF/LiF GB on Li with added Li at TPB (c) Initial and final optimized structures of LiF/LiF GB on Li with added Li at other sites in the interface. Pink colored spheres depict Li atoms, and green colored spheres show F atoms. The added Li atoms are shown in blue. . . . .	90
31	Charge density difference maps of LiF/Li <sub>2</sub> O GB on Li surface, (a) with no added Li (b) with added Li at the TPB. Purple colored spheres depict Li atoms; red colored spheres show O atoms and green colored spheres show F atoms. The isosurface scale is chosen as 0.001 e/A <sup>3</sup> . . . . .	94

## LIST OF FIGURES (Continued)

<u>FIGURE</u>		<u>PAGE</u>
32	Charge density difference maps of Li <sub>2</sub> O/Li <sub>2</sub> O GB on Li surface (a) with no added Li (b) with added Li at the TPB (c) with added Li at other interfacial sites. Purple colored spheres depict Li atoms and red colored spheres show O atoms. The isosurface scale is chosen as 0.001 e/A <sup>3</sup> . . . . .	95
33	Charge density difference maps of LiF/LiF GB on Li surface (a) with no added Li (b) with added Li at other interfacial sites (c) with added Li at the TPB. Purple colored spheres show Li atoms and green colored spheres show fluorine atoms. The isosurface scale is chosen as 0.001 e/A <sup>3</sup> . . . . .	95
34	Bulk structures of individual components in the SEI. (a) LiF, (b) Li <sub>2</sub> O and (c) Li <sub>2</sub> CO <sub>3</sub> (Pink colored spheres depict Li atoms, red colored spheres show F atoms, and red colored spheres illustrate O atoms)	115
35	Vacuum slab structures of minimum energy surfaces: (a) LiF, (b) Li <sub>2</sub> O and (c) Li <sub>2</sub> CO <sub>3</sub> (Pink colored spheres depict Li atoms, red colored spheres show F atoms, and red colored spheres illustrate O atoms)	116
36	Multi-atom hopping mechanism of Li diffusion through the GB of LiF/Li <sub>2</sub> O. . . . .	116
37	(a) Initial and final optimized structures of LiF/Li <sub>2</sub> O GB on Li surface with no added Li at the TPB. (b) Initial and final optimized structures of LiF/ Li <sub>2</sub> O GB on Li with one added Li at TPB. (c) Initial and final optimized structures of LiF/Li <sub>2</sub> O GB on Li with two added Li at TPB. (d) Initial and final optimized structures of LiF/Li <sub>2</sub> O GB on Li with two added Li at TPB. Pink colored spheres depict Li atoms; red-colored spheres show O atoms and green colored spheres show F atoms. The added Li atoms are shown in blue. . . . .	117
38	(a) Initial and final optimized structures of Li <sub>2</sub> O/Li <sub>2</sub> O GB on Li surface with no added Li atom at the TPB. (b) Initial and final optimized structures of Li <sub>2</sub> O/Li <sub>2</sub> O GB on Li with one added Li at TPB. (c) Initial and final optimized structures of Li <sub>2</sub> O/Li <sub>2</sub> O GB on Li with one added Li at TPB. (d) Initial and final optimized structures of Li <sub>2</sub> O/Li <sub>2</sub> O GB on Li with two added Li at other sites in the interphase. Pink colored spheres depict Li atoms, and red-colored spheres show O atoms. The added Li atoms are shown in blue. . . . .	118
39	(a) Initial and final optimized structures of LiF/LiF GB on Li surface with no added Li at the TPB. (b) Initial and final optimized structures of LiF/LiF GB on Li with one added Li at TPB. (c) Initial and final optimized structures of LiF/LiF GB on Li with one added Li at TPB. (d) Initial and final optimized structures of LiF/LiF GB on Li with two added Li at other sites in the interphase. Pink colored spheres depict Li atoms, and green colored spheres show F atoms. The added Li atoms are shown in blue. . . . .	119

## SUMMARY

Rechargeable Li-ion batteries (LIBs) play a crucial role in fulfilling our energy needs during our everyday residential and commercial activities. Thus, there is a growing demand for next-gen LIBs' with more robust, reliable and long-term operation. One of the ways of advancement in this technology is through the development of high-capacity electrodes with long cycle-life. However, such an advancement is severely hindered, since almost all the high capacity electrodes are accompanied with rapid mechanical degradation due to large volume changes and crack development in the electrodes during charge and discharge cycles. Therefore, a fundamental understanding of the origin of degradation mechanisms, individual processes, and their interplay is necessary to further improve this technology for a reliable and long-term operation.

Mechanical deformation and stress are responsible for most degradation mechanisms and ultimate failure of cells. In this regard, the present work addresses the theory, mathematical formulation, numerical implementation, and application of fully-coupled diffusion and structural mechanics theories aimed at capturing the ion transport and the chemo-mechanics both from a particle and interface scales. The multi-scale approach followed in the present work covers atomistic (sub-nanometer) levels through the interface scale (nanometer) up to a particle (meso-scale) scale. The multi-physics approach couples physics between the scales using the calculated and/or derived inter-domain parameters exchange. Thus, this framework allows for physical multi-scale modeling of fundamental processes occurring in rechargeable LIBs.

## SUMMARY (Continued)

At the particle scale, a continuum scale coupled diffusion-structural mechanics model (CDSM) of a single NW is proposed. The effect of large strains and the concentration-dependent elastic properties are considered, which has been proved in this work to have a great impact on the Li diffusion and the phase separation. From a materials standpoint, two types of nanowires (NW), i.e., silicon (Si) and tin oxide  $\text{SnO}_2$  are considered. The results from the CDSM simulations provide a good understanding of the induced stress due to Li insertion and the plastic deformation. possible locations where the electrode material could start to fail. Through the results, it could be understood that the lithiation induced stress leads to formation of dislocations or necking in these high-capacity electrodes, which further translates into degradation and mechanical failure upon further cycling.

At the interface scale, random Li electrodeposition, stress generation and dendrites formation in Li-metal batteries are understood by analysing the electrode/electrolyte interfaces. Since the length scales are much smaller compared to the particle scale, an atomistic scale ab-initio density functional theory (DFT) calculation is employed. The results from the DFT calculations identify the dominant diffusion pathways, energetics and the corresponding diffusion coefficients associated with Li diffusion through the polycrystalline SEI. This crucial information provides important physical insights about the localized Li diffusion and dendritic nucleation through the SEI. In addition to providing physical insights into rate-limiting processes occurring in LMBs, further DFT calculations were conducted to understand the stability of these grain structures on Li surface.

## CHAPTER 1

### INTRODUCTION AND BACKGROUND

#### 1.1 Introduction

Technological advancements and globalization have rapidly increased the global energy requirements in the last few decades across different industrial sectors. This increase in energy demand has subsequently led to an extensive use of fossil fuel based resources [2]. The consequences of this utilization pose a huge risk of dramatic climate change and extreme weather events, due to excessive emission of greenhouse gases and degradation of air quality [3]. Furthermore, the depleting fossil fuel resources have fastened the exploration towards the development of new energy sources. Also, more stricter regulations have been imposed to improve fuel efficiency and minimize emissions in automobiles. Efforts to meet current and future goals of regulation have resulted in the advent new technologies. Almost every automotive industry is now investing on vehicle electrification with a primary focus on the development of better energy storage technologies.

Rechargeable ion batteries have always been considered the most preferred for automotive and grid storage technologies due to their ability to be charged and discharged repeatedly. Some of the other desired attributes of such batteries in these applications, include long cycle and shelf life, high energy density, light weight, and low cost [4–6]. Compared to the other battery technologies, LIBs provide the best energy densities, exhibit no memory effect, and

possess high shelf-life when not in use. These advantages, as well as their decreasing costs, have established LIBs as an attractive candidate for the next generation of automotive and other electronics applications.

The key components in a rechargeable-ion battery include a cathode, an anode, and an electrolyte [7]. The cathode, or the positive electrode, is typically made of metal oxides. The anode is the negative electrode. These batteries can be classified by ion that is transported through the electrolyte. If Li ion is the intercalated between the electrodes during charge and discharge cycles then the battery is termed as Li ion battery. In the recent years, research interests have peaked up in Na ion and Mg ion batteries as well. Although, they have some differences with the Li ion batteries the underlying principle is identical to Li ion batteries and the modeling strategies used to understand their functioning are very similar.

Most commercially available Li-ion batteries have graphite anodes [7]. The transport medium for Li-ions is provided by the electrolytes. The basic functioning of the battery is defined as follows: When the battery is charged, the Li ions from the cathode move through the electrolyte into the anode. When the battery discharged, Li ions travel through the electrolyte from the anode back to the cathode. This cycle is repeated for every charge and discharge until the battery completely degrades. A schematic of LIB is as shown in Figure 1.

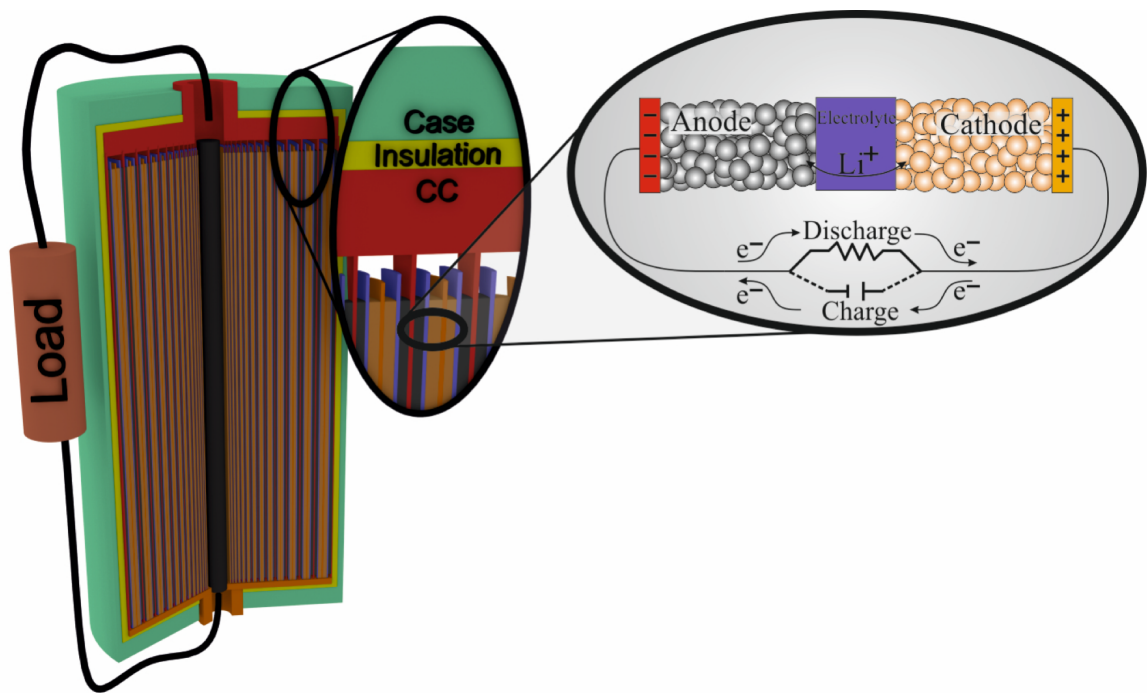


Figure 1. Schematic of a LIB with its components. Left – cross-section of cylindrical battery depicting layered structure, right – illustration of battery's repeat unit (i.e., anode, electrolyte and cathode together with two current collectors).

## 1.2 Motivation

'Lithium-ion battery' represents a wide variety of chemistries and cell designs [8, 9]. One of the major issues with most of these chemistries in LIBs is the mechanical deformation and the associated stresses development, which involve complex chemo-mechanic processes and it plays a critical role at all the different length scales [10]. A lack of precise knowledge of such degradation behaviors across different environments and operational parameters makes ex-

tracting their best performance challenging. Significant trade-offs are currently being made to optimize battery performance in automotive applications, including over-sizing and under-utilization. Therefore, modeling and identifying the degradation mechanisms are highly relevant. However, the approaches for such an extensive understanding are spread out at different length scales, due to the multi-physics and multi-scale nature of the electrochemical processes in the nanostructured electrode materials which leads to the degradation. Thus, to understand these processes and to translate molecular-scale insights into improved design and a thorough understanding of the degradation behavior across a range of length and time scales is required.

The transport processes in LIBs consist of coupled mechanical and chemical phenomena from nanometer scale to centimeter scale as shown in Figure 2. Therefore, to describe, design and control complex electrochemical systems successfully, modeling approaches in each of these scales should be utilized to understand the degradation due to molecular level diffusion, SEI evolution, dendritic growth, etc and their influence macroscopic level phenomena such as stress evolution, concentration distribution and heat generation.

The goal of this research is to develop an integrated multi-scale modeling framework to significantly increase the understanding of the fundamental process occurring during the operation of LIBs and address the degradation mechanisms in LIBs. A complete understanding of LIBs will invariably require models covering all the different scales as described in Figure 2; however, in this work, the focus is limited to the single active particle scale (e.g., single NW) and the interphase scale (e.g., SEI at the electrode- electrolyte interphase), as shown in Fig-

ure 3. To this extent, the mechanistic based models at the continuum and atomistic scales for predicting the chemo-mechanical processes are developed. The modeling studies are tightly coupled with in-situ TEM experiments, provided by our experimental collaborators, so as to gain unprecedented mechanistic insights into the electrochemically driven structural evolution and damage processes in the electrodes.

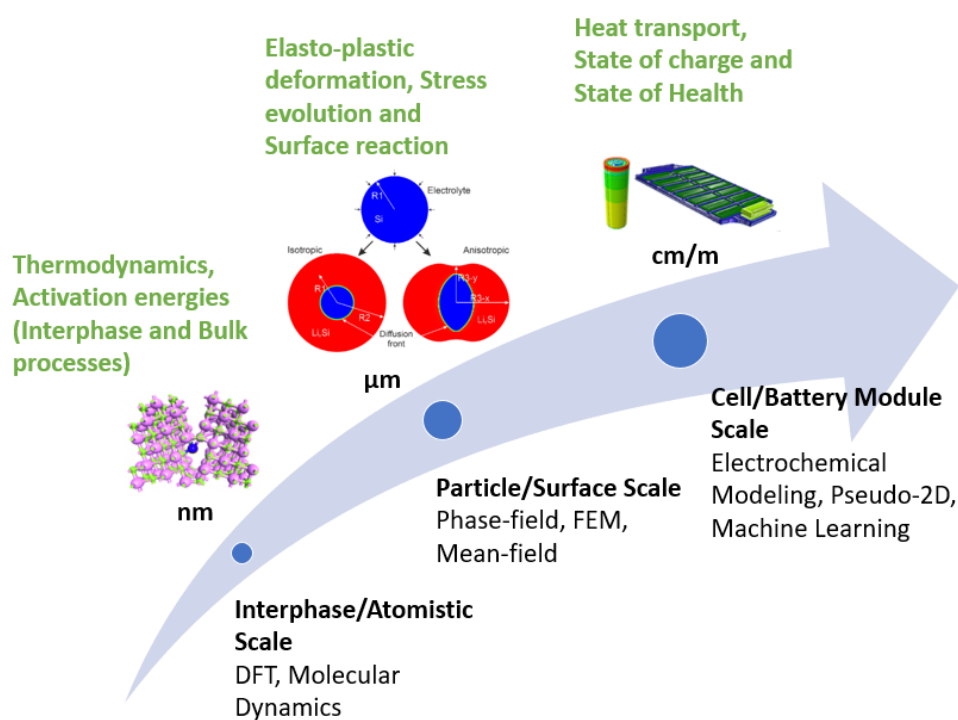


Figure 2. Multiple scales of modeling for LIB. Interphase/atomistic scale – resolution to atom-atom interaction taking into account relativistic effects; Particle/surface scale – mean-field averaging at microscale and Cell/battery pack scale – continuum modeling with a purpose of system integration.

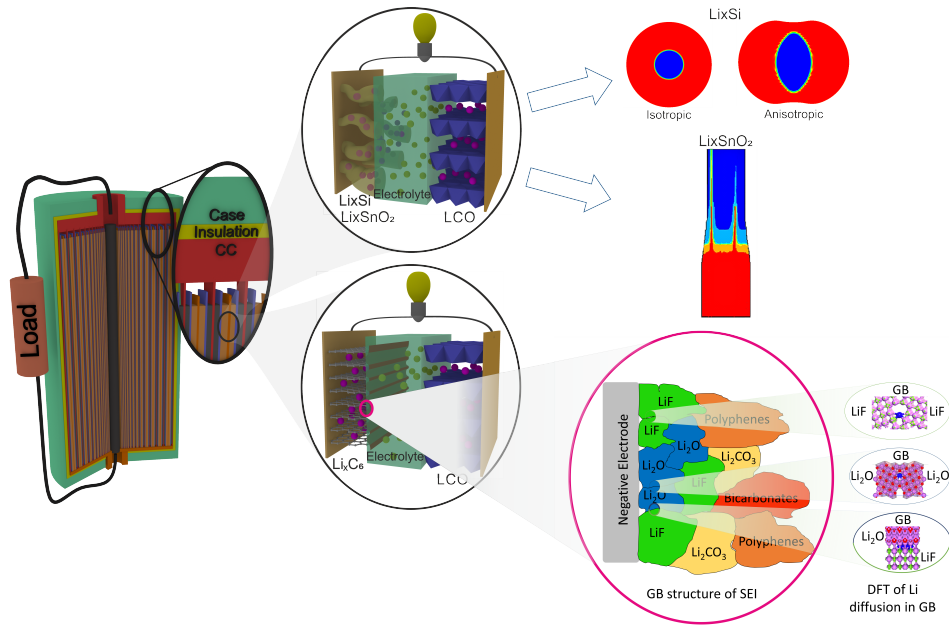


Figure 3. Schematic of particle scale and interphase scale modeling approaches.

### 1.3 Rechargeable-ion Batteries – Degradation Phenomena

Most of the commercially available, rechargeable-ion batteries that have high energy density are LIBs. Almost all commercial LIBs have graphite as their anode. However, to further enhance the capacity of these batteries, researchers seek new materials for the anodes. Some of the most promising anode materials are Si,  $\text{SnO}_2$ , etc. This is due to their low discharge potential and high theoretical charge capacity. However, such a high capacity of Li in these anode materials during charging and discharging is accompanied by a large and irreversible volume changes, which results in crack formation, or in some cases pulverization and capacity fade, thereby leading to performance degradation at a particle scale [11–13]. To mit-

igate this performance degradation in anode materials, researchers have developed nanostructured anode materials. The nanostructures have short Li diffusion distances, and can reduce lithiation-induced stress to avoid pulverization. Hence, these novel materials are able to withstand longer cycles with less degradation in electrochemical performance [10,13,14]. Although there are a number of significant contributions in the literature on the electrochemical behavior of these materials, the mechanical behavior and failure mechanisms associated with these materials remains largely unknown. Also, since the degradation mechanisms for cells of different chemistries follow different paths there is a lot of misinformation about the modes of failure.

The other forms of degradation include growth of a SEI layer, that forms between the anode and electrolyte due to the decomposition of electrolyte on the electrode surface. This layer, initially protects the anode surface, by keeping the anode physically separated from the electrolyte, which reduces side reactions along the anode surface, and maintains stability between the anode and electrolyte [15–17]. However, some reactants from the electrolyte will still reach the surface and continued growth of the SEI layer will occur with further cycling. This increases the resistivity of the cell and reduces the active lithium in the system. This process lowers the energy and power capacity of the battery.

Therefore, improving the overall performance of these nanostructured electrode materials requires an understanding of interplay between mechanical behavior and electrochemical processes, as well as physical mechanisms at various length scales.

## 1.4 Literature Overview

Modeling and simulating the coupling of concurrent multiple physics phenomena at various length scales have attracted tremendous research efforts in the recent times. A wide range of modeling and simulation methods have been applied to investigate the physical mechanisms for improving the reliability and performance of the novel electrode materials. This section provides an overview on some of the literature across these different modeling strategies, both at the particle and the interphase scales.

### 1.4.1 Particle Scale

At the particle scale, the issues such as under-utilization, capacity fade, thermal runaways, and low energy density are addressed. Although a tremendous research effort is dedicated to improving LIB's electrochemical performance and durability, its practically obtained energy density is still fairly limited due to its limitations in terms of energy density and capacity fade. Over the last two decades, the tremendous efforts of researches brought the LIB, based upon the intercalated graphite electrode, to its theoretical energy density limits. Thus, to achieve a higher energy density in LIBs, new anode materials, such as silicon and its composites, Sn based materials, etc are being intensively studied as potential replacements for the currently used graphite [18–20]. One of the critical issues associated with these high-capacity electrodes is the large volume change (e.g., 300% for Si) during Li insertion and extraction. Recent experiments indicate that this plastic deformation can readily occur in high-capacity electrodes during lithiation [21, 22]. The high value of the resulting stresses causes fracture and, in some cases, completely pulverizes of the electrode. This leads to a loss of electrical

contact and limits the cycle life of LIBs [11, 12]. To address this issue, it is essential to understand how the stresses arise and evolve in the lithiated electrodes. Despite the significant advancement of experimental procedures, such as the in-situ transmission electron microscopy (TEM) methods, computational modeling is of crucial importance as a complementary technique to draw quantitative conclusions and shed more light on the mechanisms, origin and progress of chemo-mechanical phenomena in LIBs [23].

In the prior literature, the macroscopic modeling of Li intercalation into the electrodes at the particle scale and their elasto-plastic deformation has primarily followed two approaches. One is based upon a coupled temperature-displacement model, which is analogous to the diffusion-expansion process occurring during the lithiation. The second is based upon phase-field model (PFM) using Ginzburg-Landau formalism, where different evolution equations are used, in particular, the Cahn-Hilliard equation for conserved variables, and the Cahn-Allen equation for non-conserved variables. In the PFM, the so-called diffuse-interface model uses continuous order parameters (e.g. Li concentration) between two neighboring phases. These order parameters are coupled to mechanical stresses avoiding the need to trace the arbitrarily moving interface [24].

Zhao et al. [25] adopted a detailed model of stress evolution in a single spherical particle, where an initial boundary value problem was developed using nonlinear thermodynamics to show diffusion-induced plasticity. Other cohesive zone models of fracture in materials during lithiation of nanowires [26] or thin films, [27, 28] as well as detailed models that consider the collective behavior of a microstructure have been theorized. However, most of these mod-

els introduce various approximations which make these models often less accurate. One of the most advanced and complete modeling studies using the first approach (i.e. a coupled temperature-displacement model) was performed by Liu et al. [27] who developed a model to capture anisotropic swelling and fracture of Si nanowire during lithiation. In the cited work, the anisotropic expansion is ascribed to the interfacial processes of accommodating significant volumetric strains at the lithiation reaction front in Si, which strongly depends on the Si crystallographic orientation.

There has been a tremendous increase in the studies related to the investigation of lithiation of battery's electrode using PFM in the recent years. The PFM has been successfully applied to the investigation of LIBs by simulating the effect of various parameters on the lithiation processes. In particular, Li diffusion dynamics in the  $\text{LiFePO}_4$  cathode [29,30], size-dependent phase separation [31], solid electrolyte interface formation [32] and diffusion-induced crack propagation [33] have been studied using the PFM framework. However, only a few studies have included elasto-plastic effects in the modeling of the lithiation processes [1]. Among these work, the most detailed quantitative study has been performed by Chen et al. [1]. Chen et al. developed a PFM to account for the large elasto-plastic deformation and investigate the evolution of phase, morphology and stress in crystalline silicon electrodes. [1] In their work, the Li concentration profiles and deformation geometries have been solved concurrently using a set of coupled phase-field and mechanics equations in a finite element formulation. In addition, the authors have performed a detailed study on the influence of the plastic contribution to the stress development.

### 1.4.2 Interphase Scale

At the interphase scale, battery researchers attribute majority of the undesired phenomena such as random Li electrodeposition and dendrites formation in Li-metal batteries and anisotropic diffusion/reaction and exfoliation in case of Li-ion batteries, etc to the nature of Li diffusion through Solid-Electrolyte Interphase (SEI). These undesired phenomena often results in the degradation of performance or possible failure of LIBs. Though, composition, structure and the formation mechanism of the SEI in lithium-based (e.g., Li-ion, Li-metal) batteries have been widely explored in the literature, very little is known about the ions transport through the SEI and their associated stresses. Therefore, the fundamental understanding of the underlying ions diffusion processes and the evolution of stresses across the SEI could lead to a significant progress, enabling the performance increase and improving safety aspects of batteries.

The concept of the SEI was first introduced by Peled et al. [34] in 1979 and further improved in their later works [35–37]. With further contributions to the field of the SEI understanding [38–40], two major models have emerged explaining the SEI structure and composition. The first model is called “multi-component, multi-layer structure,” the second model, developed by Shi et al. [41], called “two-layer-two-mechanism diffusion.” Both models describe the SEI as a two-layer film consisting of organic (outer layer – close to the electrolyte) and inorganic (inner layer – close to the electrode). The main difference between these two models is in the structure of the inner layer. In particular, the first model describes it as a grain-structured layer, where ions can diffuse through the grains (i.e., the individual components

of the SEI) and the GB formed between those individual components. The second model considers the inner layer as one structured sub-layer, where ions diffuse through it via the knock-off mechanism [41]. Since the inner (inorganic) layer is located directly at the surface of the negative electrode, the ions diffusion through this last layer directly affects the morphology of Li electrodeposition and governs the cycling performance of the battery.

As discussed above, there have been many studies in literature, which provides a good understanding parameters such as composition, morphology and thickness of the SEI and their growth mechanisms, but very little effort has been dedicated towards understanding the SEI as an ion transport media and the role of GB diffusion in Li intercalation/electrodeposition. This is due to the fact that the experimental verification of such theories is very challenging. Thus, computational simulations have become a valuable tool to study the properties, stability and diffusion characteristics of the SEI.

Before developing the detailed concept of the Li diffusion model through the SEI, it is helpful to review the aspects of the Li diffusion through the SEI individual components. The major components of the inner inorganic layer of the SEI in both Li metal and graphite negative electrodes are LiF, Li<sub>2</sub>O and Li<sub>2</sub>CO<sub>3</sub> at temperatures in the range of 250 K to 400 K. Benitez et al. [42] have used the classical molecular dynamics (MD) simulations to study the Li ion diffusivity in three main inorganic components of the SEI. The findings in this work suggests that, in LiF and Li<sub>2</sub>CO<sub>3</sub>, Li diffuses through vacancy-assisted and knock-off mechanisms and in Li<sub>2</sub>O a direct ion exchange mechanism is preferred. Soto et al. [43] employed ab initio molecular dynamics (AIMD) to better understand both Li and Na ions diffusion in the

SEI components such as LiF,  $\text{Li}_2\text{CO}_3$ , NaF and  $\text{Na}_2\text{CO}_3$ . They showed that the Li ions in Na-based SEI components prefer an interstitial ion diffusion through the knock-off or direct hopping mechanism, while the Na ions in Li-based SEI components show a preference for the vacancy diffusion and knock-off mechanisms [43].

Liu et al. [44] have performed DFT calculations to evaluate the influence of two major SEI components (LiF and  $\text{Li}_2\text{CO}_3$ ) on the Li surface energy. This study shows that the energy barrier for electron tunneling in LiF/Li interface is higher than the  $\text{Li}_2\text{CO}_3$ /Li interface. In the other study, Chen et al. [45] calculated the Li migration energy barriers for the bulk structures of the three main components ( $\text{Li}_2\text{CO}_3$ ,  $\text{Li}_2\text{O}$  and LiF) of the inner SEI layer using DFT. Yildirim et al. [46] have applied first-principles calculation to study defect thermodynamics, the dominant diffusion carriers, and the diffusion pathways in crystalline LiF and NaF components of the SEI. They showed that in both LiF and NaF vacancy defects form more readily than interstitials, since both compounds have a FCC crystal structure. However, when compared to defect mediated diffusion process, vacancy concentration are very small [46].

The works of Peled et al. [37], Christensen et al. [47] and recently Leung et al. [48] are the only studies providing information on details of diffusion through GB in the SEI. Peled et al. [37] provided evidence for Li transport via the SEI grain boundaries through impedance analysis and calculation of the apparent SEI ionic resistance. Christensen et al. [47], on the other hand, developed a model to simulate the SEI growth and transport of lithium and electrons in SEI film via vacancy diffusion and interstitials but also concluded that diffusion through

grain boundary might be an important factor. Leung et al. [48] have used the DFT calculation to reveal that  $\text{Li}_2\text{O}$  grain boundaries of the SEI with sufficiently large pores can accommodate Li atoms. Also, they showed that Li metal nanostructures as thin as 12 Å are thermodynamically stable inside  $\text{Li}_2\text{O}$  cracks. Subsequently, these Li nanostructures become Li filaments.

### **1.5 Scope and Organization of Thesis**

Mechanical deformation and stress play a crucial role in the operation of LIBs, and they are responsible for most degradation mechanisms and ultimate failure of cells. In this regard, the present work addresses the theory, mathematical formulation, numerical implementation, and application of fully-coupled diffusion and structural mechanics theories aimed at capturing the ion transport and the chemo-mechanics both from a particle and interface scales. At the particle scale, a continuum level coupled diffusion-structural mechanics model (CDSM) of a single NW is proposed. The effect of large strains and the concentration-dependent elastic properties are considered, which has been proved in this work to have a great impact on the Li diffusion and the phase separation. At the interface, since the length scales are much smaller compared to the particle scale, an atomistic scale ab-initio DFT calculation is employed. The results from the DFT calculations identify the dominant diffusion pathways, energetics and the corresponding diffusion coefficients associated with Li diffusion through the polycrystalline SEI. This crucial information is further utilized in mesoscale modeling frameworks such as the phase-field model (PFM) to understand the diffusion, electrodeposition and stress generation through the grained structure SEI. In addition to providing physical insights

into rate-limiting processes occurring in LIBs utilizing a variety of computational techniques, this work deals to a great extent with development and numerical implementation of computational techniques.

The rest of this thesis is structured into four chapters. First a detailed overview of the implemented modeling frameworks in this work is provided in **Chapter 2**. This includes both the frameworks used in particle scale and the interphase scale modeling of the degradation mechanisms and chemo mechanics of the LIBs. The different sections in Chapter 2 describe, with the help of the mechanics and quantum chemistry frameworks, the analytic formulation and the associated numerical procedures for ANSYS [49] based finite element method, MOOSE [50, 51] based phase-field method and VASP based Quantum chemical calculations used in this work.

In **Chapter 3** the particle scale simulations of elasto-plastic deformation in LIB electrodes due to Li insertion are discussed in detail, starting from the model assumptions and validation using Li diffusion through Si and then further extension of the work to capture anisotropic expansion in Si and stress effects on diffusivity in other materials such as SnO<sub>2</sub>. The results shown in Chapter 3 are published in two research articles (Ramasubramanian, A., Yurkiv, V., Najafi, A., Khounsary, A., Shahbazian-Yassar, R., Mashayek, F. “A Comparative Study on Continuum-Scale Modeling of Elasto-Plastic Deformation in Rechargeable Ion Batteries”, *J. Electrochem. Soc.*, 2017, 164 (13), A3418–A3425.) and (Ramasubramanian, A., Yurkiv, V., Nie, A., Najafi, A., Khounsary, A., Shahbazian–Yassar, R., Mashayek, F. “A Numer-

ical Study on Striped Lithiation of Tin Oxide Anodes”, *Int. J. Solids Struct.*, 2019, 159, 163–170.) and the copyright information from the journal is provided in Appendix A.

In **Chapter 4** the interphase scale, quantum chemical calculations of Li insertion through SEI, specifically through the GBs of SEI and their stability on electrode surface in detail, starting from the formation of the grain structured SEI and nudged elastic band (NEB) calculations for diffusivity and further explaining the stability of these grain structures by forming interfaces with Li electrode surface. The results shown in Chapter 4 are published in a research article (Ramasubramanian, A., Yurkiv, V., Foroozan, T., Ragone, M., Shahbazian-Yassar, R., Mashayek, F., “Lithium Diffusion Mechanism through Solid-Electrolyte Interphase (SEI) In Rechargeable Lithium Batteries”, *J. Phys. Chem. C*, 2019.) and an article under consideration (Ramasubramanian, A., Yurkiv, V., Foroozan, T., Ragone, M., Shahbazian-Yassar, R., Mashayek, F., “Stability of SEI on Lithium Metal Surface on Lithium Metal Batteries (LMBS)”, *Electrochimica Acta*, Under Review).

**Chapter 5** provides a detailed summary of conclusions drawn from these modeling efforts and possible future directions of the current research.

## CHAPTER 2

### COMPUTATIONAL METHODS AND METHODOLOGIES

This chapter elaborates upon the development of a multi-scale framework that describes the phenomenological changes due to the transport of lithium in the electrode and electrolyte phases both at the particle scale and at the interphase scale. Starting with a formulation at the particle scale, the CDSM and the PFM models described in this section capture the Li-ion transport through the core-shell structures of Si and SnO<sub>2</sub> and identify the physics-based conditions under which the morphological changes and the failure due to stress development occurs in these electrodes. The PFM model shown in this work is implemented by Dr. Vitaliy Yurkiv in [52, 53] and is used for comparison of the implementation of the physics-based conditions and further extension of the CDSM model. At the interphase scale the formulation for the quantum chemical calculations using the first principles (*ab-initio*) DFT using Vienna ab-initio simulation package (VASP) are provided.

#### **2.1 Particle scale Modeling of Li-ion Battery Degradation**

The present work develops two computational models to mimic ions intercalation and the resulting mechanical changes in battery electrodes at a particle scale notwithstanding shape and chemistry. For example, both lithiation and sodiation could be modeled with circular or square electrode geometry consisting of different compositions such as Si, Sn, SnSb, etc. In this work, to capture ions intercalation process and associated with it stress generation,

we make the following modeling assumptions: (i) Although, ion transport in a battery electrode can proceed through the formation of several intermediate phases, we model such a diffusion/intercalation process, in the CDSM model, in a unified manner using non-linear diffusion. The intercalated species concentration, which progresses as a result of diffusion, is marked with the letter ‘ $c$ ’. (ii) In both models the plastic flow is captured using the stress distribution due to intercalation transformation strain. (iii) A 2D plane strain model is assumed to be a good representative model for a solid three-dimensional structure undergoing ions intercalation.

### 2.1.1 Coupled Diffusion/Structure Mechanics Model

In this section, the CDSM model that numerically implements both the diffusion model and the elasto–plastic model for the ions intercalation of the nanowire electrode is described. A concurrent coupled field element is used, which has both translational and concentration degrees of freedom. The model captures the coexistence of ions-poor and ions-rich phases, which are formed during the intercalation. In order to capture their coexistence and a very thin reaction front that separates them, the ions diffusivity,  $D(c)$ , is assumed to be nonlinearly dependent on the local intercalated ions concentration

$$D(c) = D^0 \left[ \frac{1}{(1-c)} - (2\alpha c) \right], \quad (2.1)$$

where  $D^0$  is the constant diffusivity coefficient at zero concentration, and  $\alpha$  is a parameter used to control the concentration profile near the reaction front. An elasto-plastic model with

perfect plasticity is used to describe the intercalation-induced deformation. The total strain,  $d\varepsilon$ , is given by three major components.

$$d\varepsilon = d\varepsilon^e + d\varepsilon^p + d\varepsilon^c, \quad (2.2)$$

where,  $d\varepsilon^e$ ,  $d\varepsilon^p$ , and  $d\varepsilon^c$  are the elastic, plastic, and chemical strains, respectively. In Equation 2.2, the increment of chemical strain,  $d\varepsilon^c$ , is directly proportional to the normalized ions concentration,  $d\varepsilon^c = \beta \dot{d}c$ , where  $\beta$  is the expansion coefficient. The expansion equation due to concentration is critical to relate the physics of diffusion process to deformation. Then, the stress evolution is captured using appropriate constitutive equations that relate the strains to the stresses. In the elastic region, the stress is related to the increment of strain,  $d\varepsilon^e$ , by the generalized Hooke's law. In order to account for material property evolution due to the intercalation process, material properties, such as the Young's modulus of elasticity is considered to linearly decrease with increase in concentration.

A bilinear isotropic hardening model is adopted to describe the elasto-plastic transition of the intercalated Li in electrode. In the plastic region, the increment of strain,  $d\varepsilon^p$ , is assumed to follow  $J_2$  plastic associative flow rule based on von Mises stress yield surface, where von Mises stress,  $\sigma_{eq}$ , becomes equal to the instantaneous yield stress,  $\sigma_y$ , based on the linear hardening law. The strain and stress rates are related by the following expression:

$$\tau^{\nabla p} = \frac{E}{1 + E} \left[ \varepsilon^p + \frac{\nu}{1 - 2\nu} \text{tr}(\varepsilon^p) I \right], \quad (2.3)$$

where,  $E$  and  $\nu$  are the Young's modulus and the Poisson's ratio, both of which change linearly with concentration; "tr" denotes the trace of a tensor;  $I$  denotes the identity matrix and  $\tau$  denotes the Kirchoff's stresses.

The species concentration and stress-strain fields are solved with an implicit, coupled temperature-displacement procedure in ANSYS. Since the governing equations of the slow chemical stress are mathematically analogous to those of thermal stress, they are solved by treating the chemical source as a thermal source. The species ion diffusion is considered analogous to heat diffusion, and the expansion coefficient is equivalently treated as the thermal expansion coefficient. An 8-node quadratic coupled field element is used to accommodate both the structural and thermal degrees of freedom. The element has eight nodes with four degrees of freedom per node. The finite deformation effects due to diffusion, geometric non-linearity and material non-linearity are considered by using a large deformation formulation and bilinear isotropic hardening material model respectively. The finite element equations of the coupled field problem as utilized by the element type are given by,

$$\begin{bmatrix} [M] & 0 \\ 0 & 0 \end{bmatrix} \begin{Bmatrix} \ddot{u} \\ \ddot{c} \end{Bmatrix} + \begin{bmatrix} [C] & 0 \\ 0 & [C^{Diff}] \end{bmatrix} \begin{Bmatrix} \dot{u} \\ \dot{c} \end{Bmatrix} + \begin{bmatrix} [K] & 0 \\ 0 & [K^{Diff}] \end{bmatrix} \begin{Bmatrix} u \\ c \end{Bmatrix} = \begin{Bmatrix} \{F\} + \{F^{Diff}\} \\ \{Q\} + \{Q^{ted}\} \end{Bmatrix}, \quad (2.4)$$

where,  $[M]$  denotes the mass matrix,  $[C]$  and  $[K]$  denote, respectively, the damping and the stiffness matrices for structural and diffusion (with superscript Diff) terms,  $u$  denotes the displacement.

### 2.1.2 Phase-Field Model

The PFM based numerical simulations are performed using the software package MOOSE. The modeling framework and implementation is explained in detail in [52] and [53] and is used here as a comparison to the CDSM model. The finite element solution of the phase-field equations is achieved by employing Jacobian-Free Newton Krylov (JFNK) [51] method. To discretize the Cahn-Hilliard equation (Equation 2.5), using a finite element formulation a weak form of the equation is constructed. Since it has a fourth-order gradient, the equation is split into two second-order equations, such that two variables are solved, the concentration,  $c$ , and the chemical potential,  $\mu$

$$\frac{\partial c}{\partial t} = \nabla \cdot M \nabla \mu, \quad (2.5)$$

$$\mu = \frac{\partial f_{ch}(c)}{\partial c} - \frac{1}{2} \kappa_c (\nabla c)^2 + \frac{\partial f_{els}(\varepsilon, c)}{\partial c}, \quad (2.6)$$

In this case, the weak forms of the two residuals of Equation 2.7 and Equation 2.8 are

$$\left( \frac{\partial c}{\partial t}, \psi_m \right) = (M \nabla \mu, \nabla \psi_m) - \langle M \nabla \mu \cdot \vec{n}, \psi_m \rangle, \quad (2.7)$$

$$(\mu, \psi_m) = \left( \frac{\partial f_{ch}(c)}{\partial c} + \frac{\partial f_{els}(\varepsilon, c)}{\partial c}, \psi_m \right) - (\kappa_c \nabla c, \psi_m) - \langle \kappa_c \nabla c \cdot \vec{n}, \psi_m \rangle, \quad (2.8)$$

where  $\psi_m$  is the test function. In these equations, parentheses represent the volume integral and chevrons indicate the surface integral. The displacement and the corresponding strains

are calculated using a tensorial form of solid mechanics as implemented in the MOOSE Framework. Subsequently, the elastic energy is computed using the computed strains and passed to the PFM.

In the framework of the PFM, a total free energy functional for an isothermal system is defined as,  $F(c, \varepsilon)$

$$F(c, \varepsilon) = \int_V \left[ f_{ch}(c) + \frac{1}{2} \kappa_c (\nabla c)^2 + f_{els}(\varepsilon, c) + f_{pls}(\varepsilon) \right] dV, \quad (2.9)$$

where,  $\varepsilon$  denotes the strain,  $f_{ch}(c)$  the chemical,  $f_{els}(\varepsilon, c)$  the elastic, and  $f_{pls}(\varepsilon)$  the plastic energy contribution to the local energy density.  $\frac{1}{2} \kappa_c (\nabla c)^2$  is the contribution due to the ions concentration gradient. The parameter  $\kappa_c$  is the gradient energy coefficient, which plays a critical role in controlling the thickness of the reaction front. Chemical free energy density is given by a double-well function which is a function of just the concentration.

$$f_{ch}(c) = c^{\max} RT [(c \ln c + (1 - c) \ln(1 - c) + \Omega c(1 - c)], \quad (2.10)$$

Equation 2.10 applies only to a regular solution model for the free energy functional.  $\Omega$  is a dimensionless parameter (barrier height), which controls the profile of the double-well energy function. The elastic and plastic contributions to the energy functional (the last two terms in Equation 2.9) arise from the lattice mismatch between pure material and ion-intercalated material. Thus, the elastic free energy is a function of concentration. This is calculated us-

ing compositional strains based on the Hooke's law. The local elastic free energy is given by Equation 2.11

$$f_{els}(\varepsilon, c) = C_{ijkl} [\varepsilon_{kl} - \varepsilon_{kl}^0], \quad (2.11)$$

Here,  $C_{ijkl} = \frac{E}{2(1+\nu)} (\delta_{il}\delta_{jk} + \delta_{ik}\delta_{jl}) + \frac{E\nu}{(1+\nu)(1-2\nu)} \delta_{ij}\delta_{kl}$  is the stiffness constant and  $\delta$  is the Kronecker's delta.  $\varepsilon_{kl}$  is the strain and  $\varepsilon_{kl}^0$  is the swelling strain caused by Li diffusion. The value of  $\varepsilon_{kl}^0$  is evaluated as  $\varepsilon_{kl}^0 = \beta dc$  with  $\beta$  being the chemical expansion coefficient. The plastic contribution is concentration independent, given by Equation 2.12

$$\frac{\partial f_{pls}}{\partial c} = 0, \quad (2.12)$$

Similar to the CDSM, in the PFM the plastic stretch rate obeys the associated J2-flow rule and we modeled the intercalated material as an isotropic elasto-plastic material by a linear hardening rule. In order to extend the model to capture such a behavior, the following mobility coefficient matrix is used as shown in Equation 2.13

$$M_{Li} = \begin{bmatrix} M_{Li}^x & 0 & 0 \\ 0 & M_{Li}^y & 0 \\ 0 & 0 & M_{Li}^z \end{bmatrix}, \quad (2.13)$$

where, the diagonal components represent mobility coefficients in different directions. In order to reproduce the anisotropic expansion of the Si nanowire as a result of the anisotropic

mobility of the Li, we use the appropriate eigenvalue tensor of the eigenstrain based on Equation 2.13

## **2.2 Interphase Scale Modeling of Li-ion Battery Degradation**

One of the main computational tools employed at the interphase scale is DFT. Over the past few decades, DFT has been the most successful, widely used method in condensed-matter physics, computational physics and quantum chemistry to describe properties of condensed matter systems, which include not only bulk crystal structures but also complex materials such as molecules, interfaces and nanoparticles. Since, the length scales of degradation at the interface scale are within few nanometers, it is the most suited method for analyzing this phenomena.

### **2.2.1 Density Functional Theory**

As mentioned in the previous chapter, in this study we focus on the components of SEI with the help of ab-initio Density Functional Theory (DFT), in an effort to understand SEI as a transport medium and evaluate the diffusion pathways through the grain structure of SEI and its energetics. The present DFT calculations are performed using the VASP code. [54] The goal for most quantum chemical calculations is to solve the time-independent, Schrodinger's equation (Equation 2.14)

$$\hat{H}\Psi_i(\vec{r}_1, \dots, \vec{r}_N, \vec{R}_1, \dots, \vec{R}_N) = E_i\Psi_i(\vec{r}_1, \dots, \vec{r}_N, \vec{R}_1, \dots, \vec{R}_M), \quad (2.14)$$

where  $\hat{H}$  is Hamiltonian operator,  $\Psi$  is the wave-function,  $E$  is the energy eigen value,  $M$  is the number of nuclei and  $N$  is the number of electrons. To solve this equation numerically, Kohn and Hohenberg [55] suggested that the ground-state energy from Schrödinger's equation is a unique functional of the electron density. This electron density that minimizes the energy of the overall functional is the true electron density corresponding to the full solution of the Schrödinger equation (Equation 2.14). However, it is impossible to solve it in practice. To overcome this challenge the Kohn-Sham theorem [55] is used which replaces the original many-body system by an equivalent independent-particle system and assume that the two systems have exactly the same ground state electron density. It mimics the original interacting system with real potential by replacing it with an assumed non-interacting system where the electrons move within an effective Kohn-Sham single-particle potential  $V$  as shown in Equation 2.15.

$$\left(-\frac{\hbar^2}{2m}\nabla^2 + V(r)\right)\psi(r) = E\psi(r), \quad (2.15)$$

where,  $E$  is the orbital energy of the corresponding Kohn–Sham orbital,  $\psi$ , and the density for an  $N$ -particle system is

$$\rho(r) = \sum_1^N \left| \psi(r) \right| \quad (2.16)$$

The total energy of a system is expressed as a functional of the charge density as

$$E(\rho) = T_S(\rho) + E_H(\rho) + E_{XC}(\rho) + \int dr \cdot \nu_{ext}(r)\rho(r) \quad (2.17)$$

where,  $T_s$  is the Kohn-Sham kinetic energy,  $E_H$  is the Hartree energy,  $E_{XC}$  is the exchange correlation energy and  $\nu_{ext}(r)$  captures the effect of external potential. It is crucial to have an accurate exchange correlation energy functional  $E_{XC}$  in order to provide a more accurate description of the system. The most widely used approximations are the local density approximation (LDA) and the generalized-gradient approximation (GGA) [56]. Compared with LDA, GGA, specifically the Perdew-Burke-Ernzerhof sol(PBESol) [57] functional, contains the gradient of electron density and is one of the most accurate functionals in DFT calculations. Another important aspect in quantum chemical calculation is the basis sets. There are two main categories of basis sets: 1) atomic orbital basis sets and, 2) Plane wave basis sets. Since, a variety of pseudopotentials are currently available to enhance the efficiency of plain-wave calculations a plane wave basis is set with projector augmented wave (PAW) [58] pseudopotentials is chosen for the systems that are analyzed in this work.

The migration barriers are calculated using the Nudged Elastic Band (NEB) [59] method as implemented in VASP. The NEB method is an established technique to identify the minimum energy path (MEP) between the given initial and final states of an electronic transition. Depending upon the configuration, there are five to nine images (structures) describing ion migration coordinates in the NEB calculations. The maximum energy difference among all images is considered as the migration barrier for ionic diffusion. All images are simultaneously optimized along the diffusion path until the forces convergence of  $0.1 \text{ eV}/\text{\AA}$  is reached.

To perform the NEB calculations the ground-state lattice constants of the bulk structures are first calculated. Then using a slab method, where the k-point samplings are set based on the

geometry of each structure for surface structure optimization, with one k-point in the surface normal direction defined with at least 15 Å vacuum region and same number of k-points on the other two directions as in the bulk calculations, the surface energies of different possible surfaces are calculated. Additionally, in order to ensure that the slab thickness is chosen properly and represents the properties of the macroscopic crystal structure, the GB energy was calculated for two different slab thicknesses. In general, depending upon the system, the GB energy changed by ca. 2 % comparing the increase of the slab thickness by ca. 10 %. Thus, the minimum reasonable slab thickness is used.

The surface energy per unit area of a slab is the difference between the total energy of the relaxed slab structure and the bulk energy with the same number of atoms. The surface energy is given by

$$\gamma^A_{surf} = \frac{E^A_{slab} - N_A E_{bulk}}{2S} \quad (2.18)$$

where,  $\gamma^A_{surf}$  is the surface energy of slab A,  $E^A_{slab}$  is the total energy of the relaxed slab,  $E_{bulk}$  is the energy of the bulk structure of A,  $N_A$  is the number of unit cells of A and  $S$  is the surface area.

Since the minimum energy surfaces are generally the most stable and naturally formed surfaces in the grain structure, these surfaces are then cleaved to form the GBs and optimized. With the optimized ground state GB structure, the GB energy is evaluated. The GB energy is calculated as follows,

$$\gamma_{GB} = \frac{E^{AB}_{GB} - N_A E_A - N_B E_B}{2S} \quad (2.19)$$

where,  $\gamma_{GB}$  is the GB energy,  $E^{AB}_{GB}$  is the total energy of the relaxed GB structure,  $E_A$  and  $E_B$  are the bulk energies of structures A and B,  $N_A$  and  $N_B$  are number of unit cells of A and B respectively and  $S$  is the surface area of the interface.

Since, the knowledge of elastic properties allows to assess the mechanical stability of the studied systems [60], it is imperative to evaluate the elastic properties of the GB systems. The elastic constants were computed by the stress-strain method outlined in Yu et al [61] and all atomic positions were fully relaxed when simulating the application of external strains.

After identifying both the thermodynamically and mechanically stable GBs, the lithium diffusion channels are through them are identified, and the NEB calculations are performed to obtain the migration barrier for Li to diffuse in that channel. The calculated values of the migration barriers are then used as the activation energies to calculate the diffusion coefficients.

The diffusion coefficient is given by,

$$D = D_0 \exp(-E_{act}/\kappa_B T) \quad (2.20)$$

where, the pre-exponential factor  $D_0 = ga^2\nu$ ;  $g$  is the dimensionality;  $a$  is the migration distance and  $\nu$  is the vibrational frequency.  $E_{act}$  is the activation energy;  $\kappa_B$  Boltzmann constant and  $T$  is temperature. To evaluate the effect of the SEI layer on suppression of the Li dendrite, the favorability criterion for the Li dendrite growth along the TPB is defined based on the energy analysis. When the Li dendrite grows along the grains of brittle SEI, work is needed to form new interface while the strain energy at the tip of the grain boundary will be

released. Since, the TPBs are the weakest points in SEI structures the excess energy due to TPB is the energy required by the dendrites to nucleate through the SEI grain structures.

$$\gamma_{\text{TPB}} = \frac{E_{\text{TPB}} - \sum_{i=1}^3 n_i E_{i,\text{coh}} - \sum_{i=1}^3 \gamma_{i,\text{GB}} S_{i,\text{GB}}}{l_{\text{TPB}}} \quad (2.21)$$

where,  $E_{\text{TPB}}$  is the total energy of the TPB structure;  $E_{i,\text{coh}}$  is the cohesive energy per unit atom of each component in the TPB structure;  $n_i$  is the number of atoms in each component;  $\gamma_{i,\text{GB}}$  is the grain boundary energy density along each of the GBs;  $S_{i,\text{GB}}$  is the surface area of the interface in the TPB structure and  $l_{\text{TPB}}$  is the TPB length. The TPB length is defined as the length measured across the Li/SEI interface along the TPB. The greater is the value of  $\gamma_{\text{TPB}}$ , the higher is the stability of the SEI grain structure on Li surface.

## CHAPTER 3

### PARTICLE SCALE DEGRADATION STUDIES

This chapter provides a detailed discussion on the particle scale degradation studies of LIBs, in specific during Li insertion through high capacity anodes such as Si and SnO<sub>2</sub>. Multiple continuum-scale modelling techniques (CDSM and PFM), as described in the previous section, are used in this work to simulate and compare the elasto-plastic deformation in these high capacity electrode materials during intercalation. The detailed discussion in this work identifies the merits and limitations of the models in the context of the assumptions in their theoretical formulations and their influences on the physics of diffusion/intercalation and deformation. Hence, this chapter delivers new insights regarding the ranges of applicability and helps to understand similarities and differences between the two models.

#### **3.1 Chemo-Mechanics of Li Insertion in Si Anodes**

*Previously published as: (Ramasubramanian, A., Yurkiv, V., Najafi, A., Khounsary, A., Shahbazian-Yassar, R., Mashayek, F. "A Comparative Study on Continuum-Scale Modeling of Elasto-Plastic Deformation in Rechargeable Ion Batteries", J. Electrochem. Soc., 2017, 164 (13), A3418-A3425.)*

Silicon (Si) is a very promising candidate as the anode material for next-generation lithium (Li)-ion batteries due to its high theoretical capacity [62]. However, the commercial use of Si is severely hampered due to its poor cycling stability and large volume expansion during

charging and discharging processes. The large expansion causes crack formation and pulverization of the anode which results in a loss of electrical contact and sudden fading of capacity. Recent research has revealed that the problems caused by the electrode deformations can be remedied through better electrode design and numerical models will greatly facilitate this design process [63–65]. Although from a theoretical perspective, different macroscopic scale models have been proposed regarding the stress evolution in these electrodes, the effect of stress on the kinetics of lithium diffusion is poorly understood. Thus a clear understanding of the stress evolution in such electrodes is very crucial. In this work, we have developed a coupled mass diffusion and expansion model using ANSYS finite element code and captured the effect of stress on the rate of diffusion using a non-linear diffusivity parameter as a function of stress. In this section, the effects of stress evolution and mechanical properties of nanostructured Si anodes on the kinetics of lithiation is well captured and discussed in great detail.

### **3.1.1 Isotropic Lithiation of Si Nanowire**

In this section, first the models are validated through comparison of the two models' predictions with the published data of isotropic lithiation of Si nanowire. Next, to demonstrate our models' capabilities, we compare the models in both qualitative and quantitative aspects. We consider an electrode (Si nanowire) surrounded by an electrolyte that undergoes lithiation in time. During the lithiation processes, the lithium insertion into the nanowire changes the material properties (because of chemical reaction) and forms a moving phase boundary separating Li-rich from the Li-poor phases. Correspondingly, Si nanowire expands with elastic

and plastic contributions. In this system, a Li concentration variable,  $c$ , describes both the Li-rich and the Li-poor phases.

### 3.1.1.1 Problem Definition and Parametrization

The computational domain for the generic framework is shown in Figure 4. It consists of two domains, namely the pristine Silicon nanowire (grey color), which undergoes lithiation and correspondingly expands, surrounded by the Li containing electrolyte (the outer region), which is accounted for by applying a constant lithium concentration on the boundaries. Following the modeling assumptions stated in previous sections, the initial circular geometry of pristine Si (grey color), with a radius of  $R1$  undergoes lithiation-expansion where circular geometry is retained for an isotropic swelling (right picture of Figure 4). This problem is solved in an axisymmetric domain as a function of the radial coordinate  $r$ , and the initial radius increases to  $R2$  in all directions. The lithiated system is comprised of two phases, as shown in Figure 4, namely, a Li-rich phase (red color) and a Li-poor phase (purple color) separated by a thin interface (phase boundary). In the course of time, this boundary moves towards the center of the nanowire forming a diffusion front. For the structural characteristics of the Si nanowire we have followed the approach by Chen et al. [1]. The appropriate scales for length, time and concentration are chosen to non-dimensionalise the governing equation. The initial radius of the nanowire which is 70 nm, is taken as the length scale ( $R1$ ) and the time is normalized using the diffusion time,  $t_d$ . In the PFM model, the diffusivity,  $D$ , is represented by mobility,  $M_{Li}$ . The initial diffusion coefficient ( $D^0$ ) of Li in Si is  $2 \times 10^{-17} \text{ m}^2 \cdot \text{s}^{-1}$ , which corresponds to an initial mobility value ( $M^0$ ) of  $2.186 \times 10^{-26} \text{ m}^5 \cdot \text{J}^{-1} \cdot \text{s}^{-1}$ . The con-

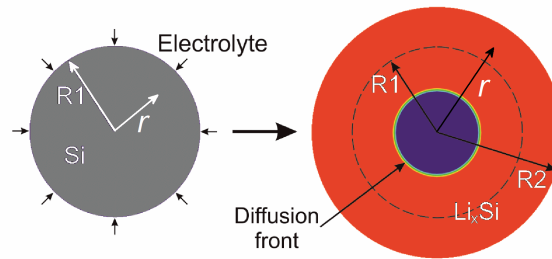


Figure 4. Schematic illustration of the computational domain.

centration is normalized using the maximum theoretical concentration ( $c$ ) which corresponds to the concentration of  $\text{Li}_{4.4}\text{Si}$ . Previous experimental measurements [27] [22] indicate that Li-rich phase has composition of  $a\text{-Li}_{4.4}\text{Si}$ , which is also confirmed by the apparent volume expansion close to that of  $a\text{-Li}_{3.75}\text{Si}$  as described by Chen et al. [1] in details. Therefore, in the present model the maximum value of the normalized lithium concentration for the Li-rich phase is set to 0.872 ( $=3.75/4.4$ ). As it is experimentally and theoretically reported,  $\text{Li}_x\text{Si}$  phase expands by 300% in volume comparing to the unlithiated structure, thus the chemical expansion coefficient,  $\beta$ , is set to 0.5874 to obtain 300% expansion.

The Young's modulus and Poisson's ratio are assumed linearly dependent on lithium concentration ranging from 160 GPa and 0.24 at zero concentration of lithium to 40 GPa and 0.22 at maximum lithium concentration, respectively. As reported by Chen et al. [1], there is no clear evidence on the actual material properties in the plastic range during the expansion process. Thus, following Chen et al. [1], the value of 1.5 GPa is adopted for yield strength

TABLE I

Simulation parameters with their dimensional and normalized values.

Parameter	Dimensional value	Normalized value	Reference
Lithium concentration	$0 - 3.125 \times 10^5 \text{ mol} \cdot m^{-3}$	$0 - 1$	[27]
Si radius, R1	70 nm	1	[27]
Mobility (PFM), $M_{Li}$	$2.186 \times 10^{-26} m^2 J^{-1}$	10	[1]
Young's modulus	160 Gpa (min conc.) to 40 Gpa (max conc.)	175 (min conc.) to 44 (max conc.)	[1]
Yield stress	1.5 Gpa	1.924	[1]
Tangent modulus	1 GPa	1.092	[1]
Expansion coefficient	0.5874	0.5874	[1]

and 1 GPa for hardening modulus. All the elasto-plastic constants (Young's modulus, Poisson's ratio, yield strength and strain hardness) are normalized by and the value of  $c^{max} RT$  and are given in Table I.

In the CDSM, the value of the dimensionless parameter,  $\alpha$ , which controls the sharpness of the reaction front, is kept at 1.75, since for values of  $\alpha$  between 1.75 to 2 the thickness of the reaction front starts to increase. For values greater than 2 the diffusivity coefficient turns

negative within the operating concentration limits, which is not physical. On the basis of the chemical free energy function, that is derived based on the regular solution model, the nonlinear function of diffusivity,  $D$ , is derived such that the diffusion rate is sharply increased at high Li concentrations, hence allowing for the formation of a sharp reaction front, as shown in Figure 4. In addition, for numerical stability, the maximum of  $D$  is capped at  $10^4$  times the value at zero concentration. In this study, due to the extensive expansion of the Si nanowire, nonlinear large strain and large rotation formulation is utilized. The nanowire is fixed at the center to maintain the static equilibrium in translational degrees of freedom. In the CDSM, the normalized computational time step size is initially set to  $10^{-8}$  which is  $24.5 \mu\text{s}$  in actual time and is set to be adaptive.

In the PFM, the gradient energy coefficient is normalized as  $= 0.0005$ . The dimensionless parameter,  $\Omega$ , controls the profile of the double-well energy function and the value of  $\Omega$  is taken as 2.6. During the PFM simulation, the time step size is initially set to 0.001 s and is set to be adaptive. Since, the Cahn-Hilliard equation involves both the concentration and mechanical terms, solution of this coupled system, as shown in Equation 2.7 and Equation 2.8, requires boundary conditions for both of these contributions. As shown in the experiments, Li quickly covers the outer surface of Si, thus the lithium concentration boundary condition at the outer surface is set to the maximum possible value of 0.872. In addition to lithium concentration, the displacements in  $x$  and  $y$  directions are set to zero at the center as displacement boundary conditions.

### 3.1.1.2 Model Validation

As described above, we performed calculations of isotropic expansion of the Si nanowire and compared our findings with the results reported by Chen et al. [1]. Figure 5 shows the representative results of the radial distribution of the normalized Li concentration for both models in comparison to the results from Chen et al. [1]. For the normalized times of 0.5, 5 and 9, we have compared the predicted Li concentration with the previously published data and we have extended the results to the time of 17. It shall be noted that these four times correspond to 10%, 30%, 50% and 80% of the progress in lithiation front, thus forming a full picture of the lithiation phenomenon of the Si nanowire.

Figure 5 shows a quantitative agreement between our simulation and Chen et al. [1] results over the complete investigated time range. There are no results available for the last time ( $t=17$ ); however, following the far left blue curve in Figure 5 it could be concluded that the Li concentration distribution, predicted by our model is physically binding. For both the models, since the slopes of the concentration curves are almost equal, the migration of the lithium front is much faster initially (from 10% to 50%), when compared to the later stage (from 50% to 80%), which is consistent with the experimentally observed fact of self-limiting lithiation phenomenon. The representative Si geometries obtained during the simulation are also shown in Figure 5.

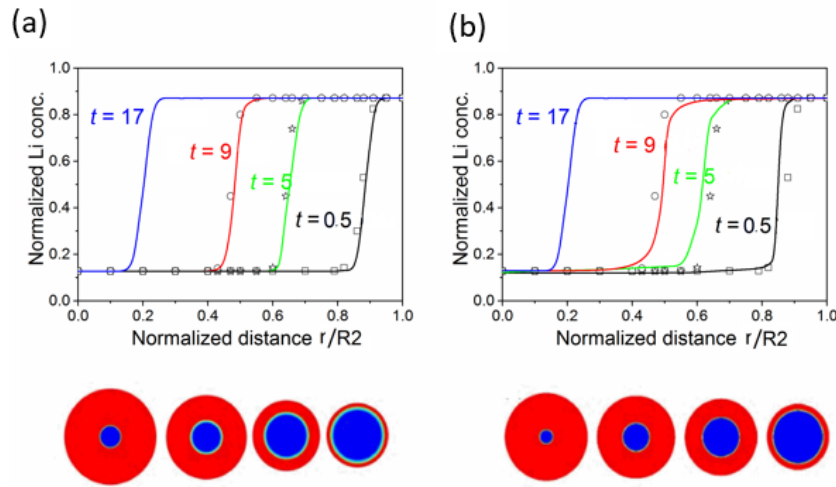


Figure 5. Concentration plots showing narrow reaction front of Si lithiation process and the respective geometries at four different times. (a) Results obtained with the PFM; (b) Results obtained by using the CDSM. Symbols are the data taken from [1]

Based on Figure 5 it can be observed that, the results obtained using the PFM (Figure 5(a)) are closer to published simulation data than the results of the CDSM model (Figure 5(b)). In particular, there is a slightly smeared interface, which is present just before of the reaction front in the CDSM model prediction. This occurs due to the slope of the nonlinear diffusivity parameter. To further validate and compare the models we have plotted stress fields originated from the lithiation. As described by Chen et al. [1], three different stress components (Hoop, radial and von Mises) were monitored at two different times ( $t = 0.5$  and 9) during the lithiation simulation as shown in Figure 6.

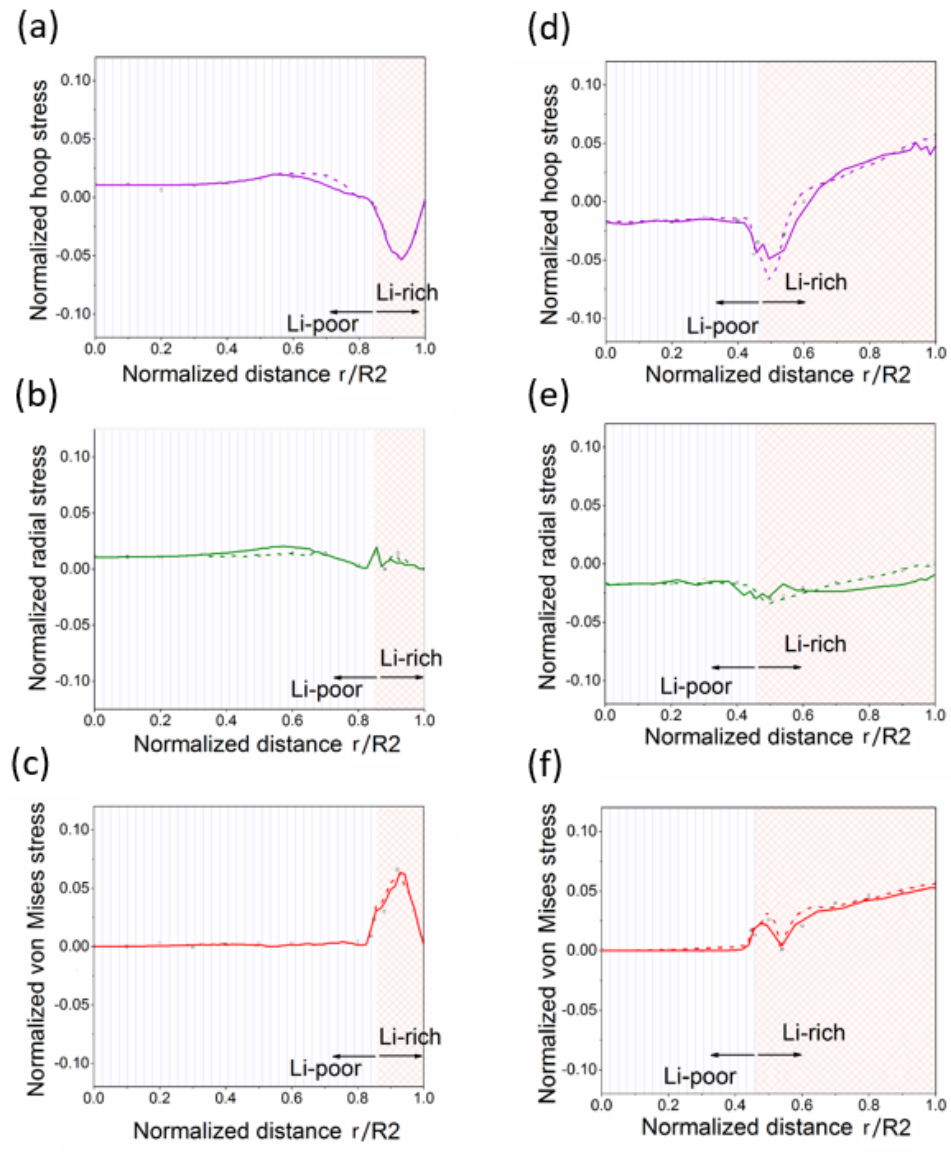


Figure 6. Stresses modeled in the radial direction at 10% lithiation (a–c) and 50% lithiation (d–f) progress, where (a) and (d) are Hoop stresses, (b) and (e) are radial stresses and (c) and (f) are von-Mises stresses. The solid lines depict the results from the CDSM elasto-plastic model and the dashed lines depict results from the PFM. All the stress components are normalized by Young’s modulus of Si,  $E_{Si}$ . Symbols represent data from [1].

The results are shown and compared to our results using the CDSM (solid lines) and the PFM (dashed line). There is a qualitative agreement between our modeling results and the results reported by Chen et al. [1] concerning both the trend and the magnitudes of the stresses over the investigated time range.

The predicted equivalent plastic strain is plotted in Figure 7, where the plastic strain at different lithiation times are compared to the findings of Chen et al. [1]. The results suggest that the lithium poor phase always remains in its elastic region since there is no load or in other words, it has near zero strains but as lithium diffuses the material properties change (because a chemical reaction has happened). This is captured through concentration dependent material properties. The material softens as a result of lithiation along with the expansion, allowing the phase to reach plasticity very quickly.

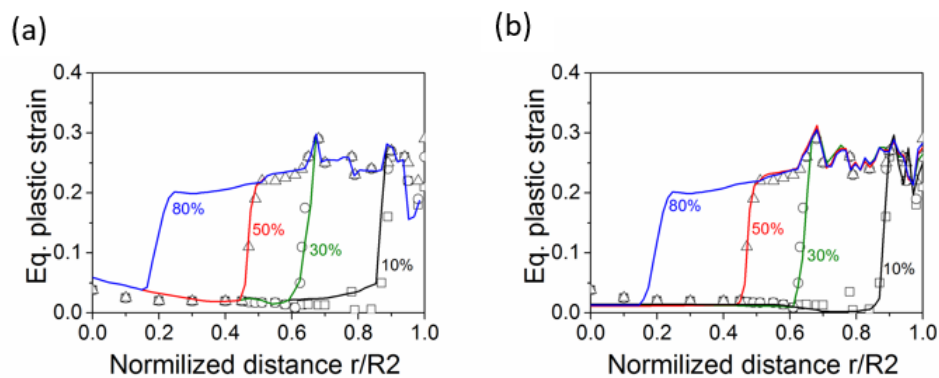


Figure 7. Plastic strain plots at 10%, 30%, 50% and 80% lithiation. Results from (a) PFM and (b) CDSM models. Symbols are the data taken from [1].

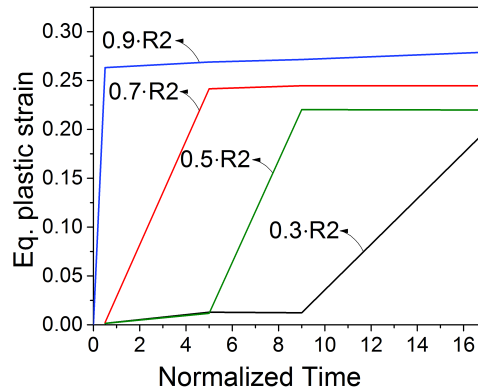


Figure 8. Equivalent plastic strain history in radial direction  $r$

Figure 8 shows the time evolution of the plastic strain over time, at different points along the radial direction. It is evident from Figure 8 that the plastic strain monotonically increases as the lithiation progresses, and the region closer to the surface that is lithiated first reaches the maximum plasticity much earlier than the region away from the surface. It also suggests that behind the reaction front the plastic strain remains fairly constant at the maximum value.

### 3.1.2 Model Comparison

In the previous sections, quantitative comparisons of the CDSM and the PFM models are made, which shows good agreement for many parameters. In this section, a detailed discussion is performed to identify the merits and drawbacks in the context of assumptions in the theoretical formulations and the influence on the physics of diffusion/intercalation and deformation.

### 3.1.2.1 Discussion on Modeling Parameters

The dimensionless parameters with which the governing equations are solved are discussed in this section. The actual and normalized values of all the parameters that are used in the CDSM and the PFM models are listed in Table I. Even though most of the parameters are set similarly in both models, some of the key parameters are handled differently, which makes the CDSM model different than the PFM.

The difference in parameterization of the diffusion coefficients has a strong impact on their time step sizes for both models. In the CDSM model, the diffusivity parameter is a highly non-linear function of concentration and it is normalized using the initial diffusivity value of  $2 \times 10^{-17} m^2 \cdot s^{-1}$  (diffusivity of Li in pristine Si). The normalized value of the diffusivity varies nonlinearly between 1 to  $10^4$  according to Equation 2.1 in order to reproduce the sharp interface development between the Li-poor and the Li-rich phases. Large values of the diffusivity coefficient lead to very small diffusion time scale, thus the time step size should be extremely small to capture tiny changes of concentration across the interface. In contrast, in the PFM the mobility parameter, which is analogous to the diffusivity parameter in CDSM, is a constant value, since the interfacial width is controlled by gradient energy coefficient. For the CDSM simulation, the normalized computational time step size is initially set to 10 ( $24.5 \mu$  s) and varies over time. In the PFM simulation, the time step size is considerably larger and is initially set to 0.001. Although, the PFM model starts with a relatively larger time step size, it quickly adapts to the smaller value in the order of  $10^{-8}$ . This difference in time step

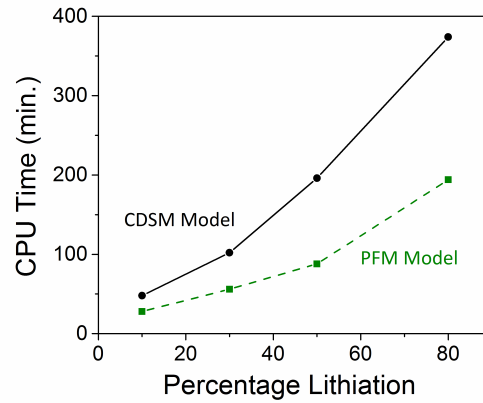


Figure 9. Comparison of the computational times of the CDSM and the PFM models. Both models are simulated with the same mesh structure on a single-core Intel Xeon 2.80 Ghz processor.

sizes makes the CDSM model more computationally expensive compared to the PFM. The comparison of the respective CPU times is as shown in Figure 9.

It is often reported in the prior literature that the value of the dimensionless parameter  $\Omega$  (Equation 2.10), which controls the profile of the double-well function in the PFM, is used for the parameter  $\alpha$  in Equation 2.1 in the coupled diffusion and structure mechanics models. However, the parameter  $\Omega$  has somewhat different physical meaning than the parameter  $\alpha$  in the CDSM model. In the CDSM simulation, the nonlinear form of the diffusivity parameter (Equation 2.1) is obtained by taking the second derivative of the chemical free energy. The resultant Equation 2.1, of the CDSM model, contains the parameter  $\alpha$ , which is used to con-

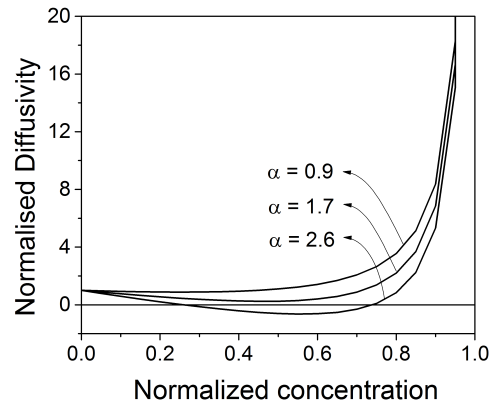


Figure 10. Variations of the normalized diffusivity coefficient Equation 2.1 for different values of the parameter  $\alpha$

control the sharpness of the reaction front by controlling the slope of the increase in diffusivity.

Figure 10 shows the variations of the normalized diffusivity values as a function of the normalized concentration using Equation 2.1 for different values of  $\alpha$ . As it is revealed from the Figure 10, the increase of the parameter  $\alpha$  drives the diffusivity towards the negative values, and vice versa if the  $\alpha$  is decreased diffusivity values are increased. Also, as the value of diffusivity increases the thickness of the reaction front decreases since the gradient becomes sharper. In the PFM, the dimensionless parameter,  $\Omega$ , controls the profile of the double-well energy function, as shown in Figure 11. In the present study, we use  $\Omega$  value of 2.6, which creates two minima in the chemical free energy corresponding to the Li-poor phase (0.128)

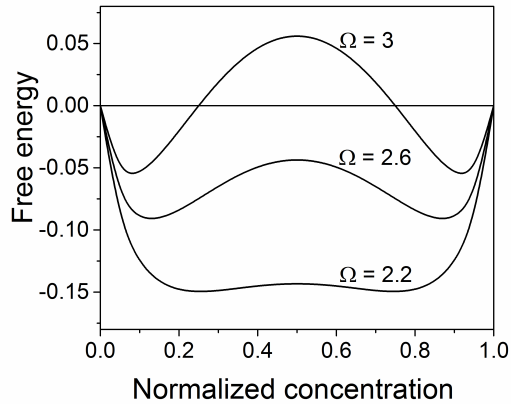


Figure 11. Variations of the chemical free energy (Equation 2.10) for different values of the parameter  $\omega$

and to the Li-rich phase (0.872). An increase of  $\Omega$  leads to an increase of the barrier height, as well as changes in the Li-poor and the Li-rich phase concentration (0.08 and 0.92 respectively). In contrast, if the parameter  $\Omega$  is reduced, the barrier height decreases significantly and the new energy minima changes the value of Li concentration in the Li-poor phase to 0.25 and in the Li-rich phase to 0.75. Thus, from the discussion above, the parameters  $\alpha$  and  $\Omega$  have somewhat different physical meanings, although they mathematically originate from the same energy function equation.

### 3.1.2.2 Comparison of Model Accuracy and Physics

In this section, the models are compared for their accuracy in capturing the lithiation process. As it is revealed by Equation 2.11, the elastic energy functional in the PFM is a func-

tion of the concentration. Thus, during lithiation, the stress has a direct effect on the values of concentration during lithiation. However, for the CDSM model, there is no direct relationship between the stress and the concentration. To capture this effect, the material is softened linearly with the increase in concentration. This provides a reasonable approximation for the case of isotropic Si lithiation, since the effect of stress on lithiation is not significant due to a large expansion of the Si. Both the models seem to capture the results with reasonable accuracy, on estimating the error percentage. In the calculated values using both the CDSM and the PFM models, as shown in Figure 5 and Figure 6, it is observed that the PFM has a slightly better accuracy (about 1% error) than that of the CDSM model (about 4% error).

### **3.1.2.3 Comparison of Models' Ease of Use**

The CDSM modeling based upon ANSYS software is certainly easier to perform since it is less complex and has extensive documentation. On the contrary, the PFM modeling with MOOSE software requires significantly more effort for adding and coupling the different physics modules. In addition, mesh generation in the MOOSE framework is usually performed with the help of external software (e.g. Gmesh, Cubit, etc.). In the ANSYS software, mesh generation is performed within the program with many possibilities for the mesh structures and re-meshing tools.

Table II summarizes the qualitative comparison between the two models. This information provides a better understanding on the applicability of each model under different circumstances. It should be emphasized that these conclusions are drawn based on the implementation of CDSM in ANSYS and implementation of PFM in MOOSE, using the PFM results of

TABLE II

Qualitative comparison of the CDSM (implemented in ANSYS) and the PFM (implemented in MOOSE Framework).

Parameter	CDSM	PFM
Complexity of model	Less Complex	More Complex
Ease of implementation	Well documented and easier to implement	More challenging to implement
Accuracy	Error < 4%	Error < 1%
CPU time	8.5 hours	3.5 hours

Chen et al. [1] as the reference data. The results could vary if the models are implemented in other software, or different reference data are used for comparison.

### **3.1.3 Model Extension - Anisotropic Swelling in Si**

After validating the constitutive models and comparing the results using the published data on isotropic lithiation in Si nanowire and then the model is extended to capture the anisotropic swelling of Si. All parameters described in Table I are continued to be used without changes, except those related to the diffusion coefficient. Several previous experimental and theoretical studies have shown that ion diffusion could be much faster in the x-direction than in the y-direction. To this extent, an orthotropic diffusion coefficient is used with x-direction diffu-

sion being 100 times faster than y-direction. Correspondingly the expansion of the electrode would be bigger in x-direction than that in y-direction, producing necking in the middle.

The swelling anisotropy of a nanowire under lithiation may depend on the plastic properties, such as yield strength, strain hardening ratio, as well as the charging rate. However, the plastic properties of the material (i.e. Si), are mostly unknown at the nano- to microscale, and it is challenging to obtain them experimentally, especially when it is alloyed with lithium ions during lithiation. Therefore, we have adjusted these parameters by capturing the electrode's shape morphology that is revealed during the lithiation, which may elucidate indirectly the plastic properties of the material. To ensure accurate results and to capture the high nonlinearity of the diffusion and material properties, a high mesh density (maximum element size less than 0.005 normalized length) and a very small time step size (order of  $10^{-10}$ ) is used.

As described in the literature review, a dumbbell-shaped nanowire cross section is observed by in-situ lithiation experiments, [27] which further leads to necking and crack formation and eventually leading to instabilities in the structure. The current finite element simulation also predicts this dumbbell-shape of Si is predicted (Figure 12). In Figure 12, the results are shown for the Li concentration (two pictures in the upper panel) and for the geometry evolution (lower panel). The Li concentration is represented by the two plots showing lithiation progress in x horizontal (R3-x) and y vertical (R3-y) directions.

The structural changes in lithiated cylindrical Si nanowires are as shown in Figure 13 and it clearly predicts the formation of dumbbell-shaped cross section. By analyzing the observed material evolution and stresses behind the reaction front, the importance of the structural

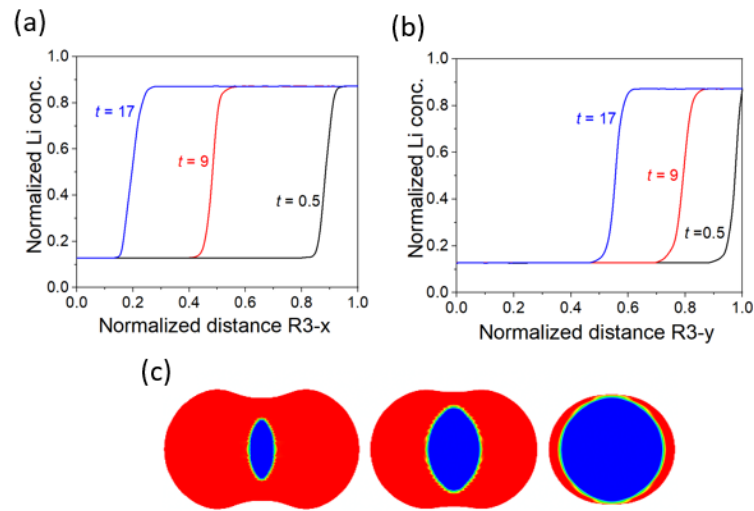


Figure 12. Lithium concentration distribution in (a) x and (b) y directions of the Si nanowire and (c) the respective geometries for three different times.

relaxation, due to the plastic flow behind the moving phase boundary can be understood.

Despite the extensive plastic flow during the lithiation process, due to excessive deformation and anisotropic expansion, high stresses develop inside the lithiated region of the nanowire, leading to cracking or splitting of the single nanowire into sub-wires.

In order to gain more insight into this unusual evolution of morphology, we have analyzed stresses generated during the anisotropic lithiation of Si. As described for the isotropic case, three different stress components (Hoop, radial and von Mises) were monitored at 10% and 50% lithiation. The results are as shown in Figure 13 Plots (a) and (b) show the stresses at 10% and 50% lithiation in the radial x-direction and plots (c) and (d) show the stresses

at 10% and 50% lithiation in radial  $y$ -direction. The results clearly show the anisotropy of stresses as the maximum and minimum induced stresses occur much closer to the surface in  $R3 - y$  direction (radial  $y$ -direction) than in  $R3 - x$  direction (radial  $x$ -direction). The sudden abrupt change in the direction of the Hoop stress is observed right after the reaction front, which is the primary reason for morphological instability, necking and fracture of these electrodes.

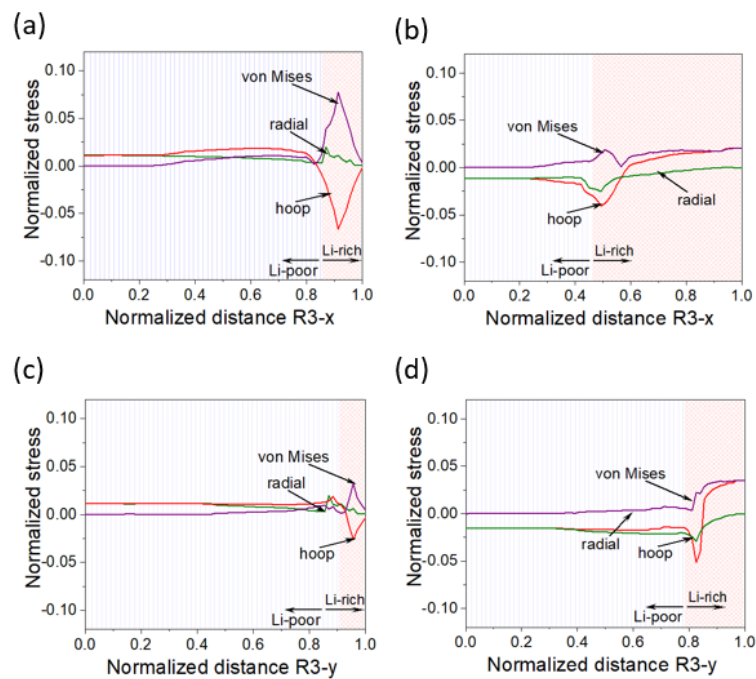


Figure 13. Radial, von-Mises and Hoop stresses measured in the direction  $R3-x$  and  $R3-y$  using CDSM framework at 10% ((a) and (c)) and 50% ((b) and (d)). All the stress components are normalized by Young's modulus of Si

The modelling framework thus provides a firm basis for simulating the morphological evolution, stress generation, and material failure in other high-capacity electrodes.

### **3.2 Chemo-Mechanics of Li Insertion in SnO<sub>2</sub> Anodes**

*Previously published as: (Ramasubramanian, A., Yurkiv, V., Nie, A., Najafi, A., Khounsary, A., Shahbazian-Yassar, R., Mashayek, F. "A Numerical Study on Striped Lithiation of Tin Oxide Anodes", Int. J. Solids Struct., 2019, 159, 163–170.)*

High energy storage capacity of SnO<sub>2</sub> makes it as one of the other promising anode materials for high capacity lithium (Li)-ion batteries besides Si. The model implemented in the previous sections can be effectively utilized to capture the chemo-mechanics in SnO<sub>2</sub> as well. However, in contrast to Si, previous experiments reported by Nie et al. [66] and Huang et al. [67] have shown that SnO<sub>2</sub> lithiation occurs in two stages. The experimental work on Sn-based systems by Zhong et al. [68] reported a peculiarity in Li diffusion and propagation in SnO<sub>2</sub>, which results in a striped diffusion regime. This was further investigated by Nie et al. [66], which confirmed that Li diffuses at low concentration along stripes Figure 14 leading to formation of lithium oxide (Li<sub>2</sub>O) when the SnO<sub>2</sub> nanowire is attached to the Li source. According to these reports, initially the Li diffuses rapidly through distinct narrow stripes along the electrode axis. This is followed by a second stage where the diffusion/amorphization of the nanowire occurs. In order to understand and possibly predict this complex chemo-mechanical phenomenon, a finite element (FE) model is developed in this work. The model captures the formation of the striped diffusion regime and the corresponding expansion of the nanowire during the lithiation of SnO<sub>2</sub> by capturing the effect of the stress on the Li diffusion.

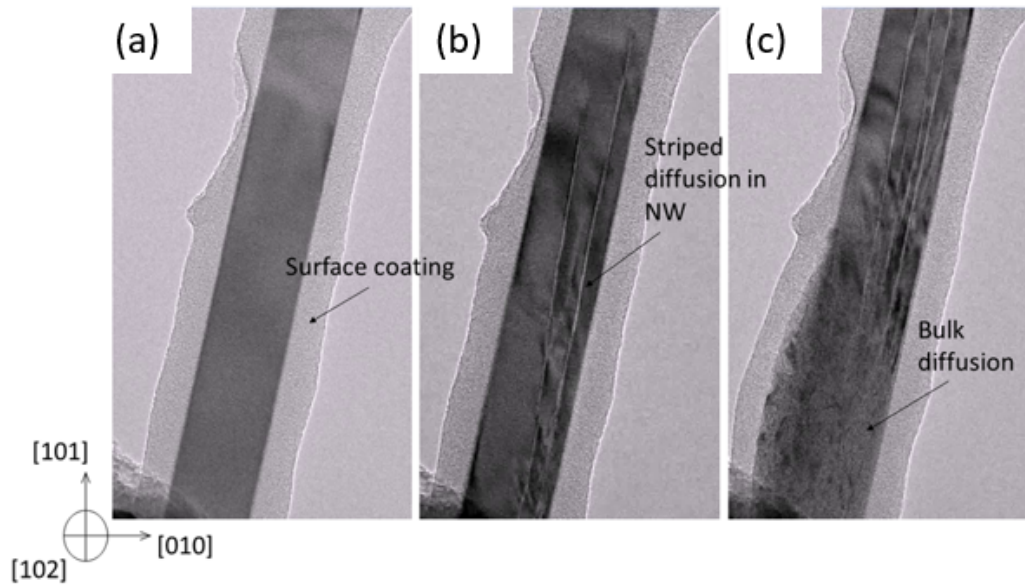


Figure 14. TEM image of lithiation in SnO<sub>2</sub> nanowire (NW), clearly showing the formation of striped diffusion regime followed by bulk diffusion with minimal contrast change on the surface of the NW. (a) shows the presence of surface carbon coating on pristine SnO<sub>2</sub>, (b) shows the initial diffusion through the striped region (long-range pipe diffusion) and (c) shows lithium diffusing through the bulk of the NW (short-range diffusion).

### 3.2.1 Problem Definition and Parametrization

In the current model, the effect of the internal stress field on the activation energy of diffusion is considered, as follows. The present modeling framework is developed to reproduce the ions intercalation and the resulting mechanical changes in the SnO<sub>2</sub> electrodes. At the

atomic scale, diffusion of a solute in a crystal lattice is described as a sequence of movements between two interstitial sites, during which the diffusing particle must overcome the energy barrier. Atomistic simulations have shown that this energy barrier is strongly influenced by the internal stresses acting on the atoms [69, 70]. In most scenarios the stresses in the directions normal to the diffusion process influences the diffusion since the expansion in lateral direction is much larger than the longitudinal direction [71, 72], suggesting a dependence of stresses perpendicular to the direction of diffusion. This effect has been referred to as strain-activated mobility by Aziz et al. [73]. But, in case of SnO<sub>2</sub> nanowires the longitudinal expansion is much larger than the lateral directions, suggesting a dependence on the hydrostatic stress.

The hypothesis in the present work, as shown in Figure 15, is that, when the nanowire is exposed to the Li source, the locally-high contact stress due to the local surface defects on the surface of the nanowire results in a faster diffusion in the longitudinal direction and initiates the stripe formation. Then, as a consequence of the diffusion of lithium along these stripes, high levels of stress are induced. This stress further drives the faster diffusion in the same direction. In order to capture this phenomenon and validate the hypothesis, a FE model is developed, which takes into account the effect of the initial contact stress on diffusion.

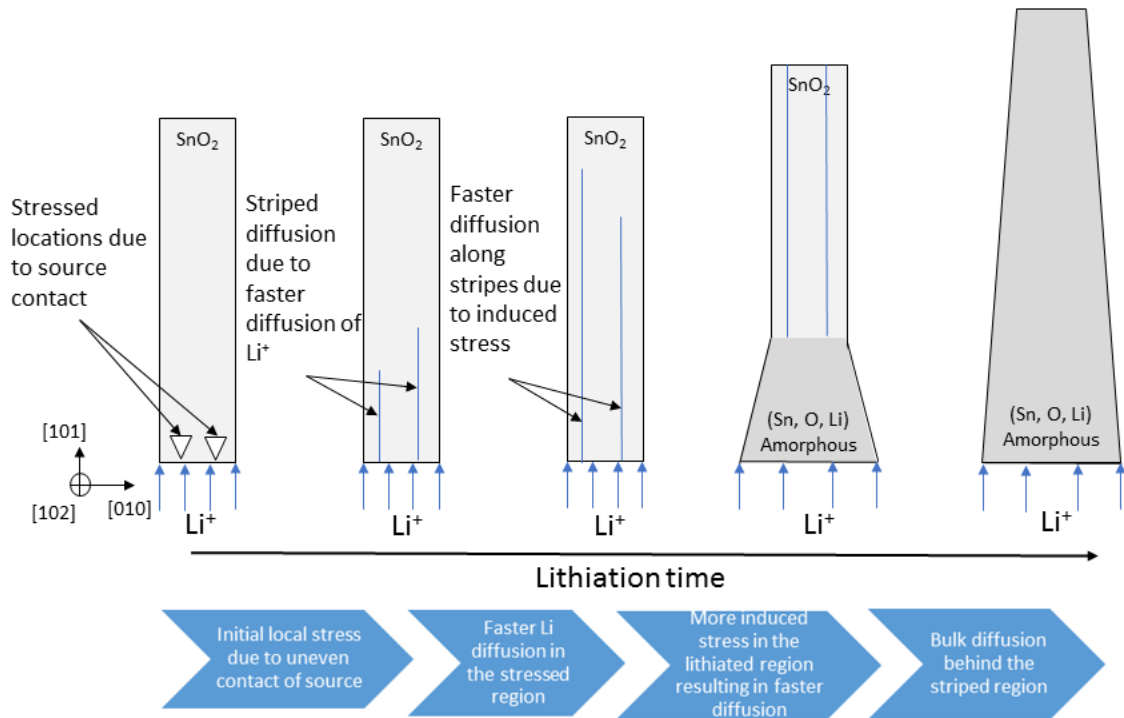


Figure 15. Schematic of initial and intermediate structures of striped diffusion during simulation. Geometrical changes are not to scale, merely for illustrative purpose.

A 2D rectangular shaped strip of tin oxide is simulated in this work to avoid 3D complications. The computational domain and the associated boundary conditions are shown in Figure 16. The dimensions of the 2D rectangular geometry are of  $150 \text{ nm} \times 5 \mu\text{m}$ . The concurrent reaction and diffusion processes are simulated as a coupled problem by treating the interfacial reaction as a nonlinear diffusion across a smeared interfacial domain for numerical convenience, despite the difference in the actual interfacial reaction and bulk diffusion pro-

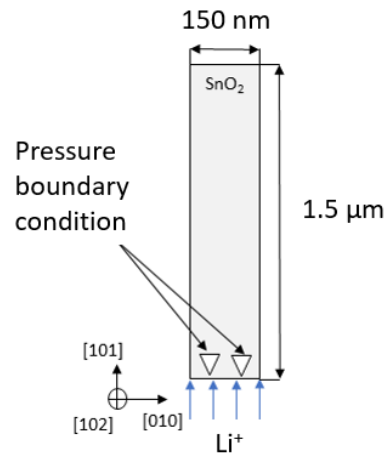


Figure 16. Schematic representation of the 2D rectangular computational domain

cesses [71]. Therefore, the classical nonlinear sharp interface diffusion is adopted to describe the Li transport in the entire domain, as shown in Equation 3.1.

$$\frac{\partial c_{\text{Li}}}{\partial t} = \nabla \cdot (D(c_{\text{Li}}, \sigma_h) \nabla c_{\text{Li}}) \quad (3.1)$$

The model has to capture the formation of the striped diffusion regime in the pristine  $\text{SnO}_2$  phase. In order to achieve this goal, the Li diffusivity,  $D(c_{\text{Li}}, \sigma_h)$ , is assumed to be nonlinearly dependent on the local Li concentration,  $c_{\text{Li}}$  and the hydrostatic stress,  $\sigma_h$ ,

$$D(c_{\text{Li}}, \sigma_h) = D_{\text{Li}}^0 \left[ \frac{1}{(1 - c_{\text{Li}})} - (2\alpha c_{\text{Li}}) \right] \cdot \exp\left(-\frac{E^{\text{act}}}{RT}\right) \exp\left(\frac{\kappa V_m \sigma_h}{RT}\right) \quad (3.2)$$

where  $D_{\text{Li}}^0$  is the pre-exponential factor;  $\alpha$  is a parameter used to control the sharpness of the concentration profile near the reaction front;  $\kappa$  is a positive non-dimensional factor, which takes into account the interaction between Li and  $\text{SnO}_2$ ;  $V_m$  is the molar volume of  $\text{SnO}_2$ ;  $R$  is the universal gas constant and  $T$  denotes the temperature. For numerical stability, the maximum of  $D(c_{\text{Li}}, \sigma_h)$  is capped at  $10^4$ . The pre-exponential factor ( $D_{\text{Li}}^0$ ) multiplied by the term in square brackets represents concentration dependence. The first exponential term describes the activation energy term as in the standard Arrhenius equation and the second exponential term in Equation 3.2, modifies the activation energy based on the hydrostatic stress magnitude and its direction. The particular form of the diffusion coefficient in Equation 3.2 can capture the formation of core shell structures and also capture the effect of stress on the structure and is adopted from the work of Haftbaradaran et al. [74].

The appropriate scales for length, time and concentration are chosen to non-dimensionalize the governing equations. The initial length of the bottom edge of the nanowire (150nm) is taken as the length scale ( $l$ ) and the time is normalized using the diffusion time. The pre-exponential factor ( $D_{\text{Li}}^0$ ) and the activation energy ( $E^{\text{act}}$ ) for the Li diffusion in  $\text{SnO}_2$  are taken from Huang et al. [67] and are  $9.67 \times 10^{-8} \text{m}^2 \text{s}^{-1}$  and 0.4 eV, respectively. The concentration is normalized using the maximum theoretical concentration ( $c_{\text{Li}}$ ) which corresponds to the concentration of  $\text{Li}_4.4\text{Sn}$ . As it is theoretically reported,  $\text{Li}_x\text{Sn}$  phase expands to 300% the original size [75] [76] in volume comparing to the unlithiated structure; thus, the chemical expansion coefficient,  $\beta$ , is set to 60% and 45% in axial and longitudinal directions, respectively [77]. The Young's modulus and Poisson's ratio are assumed linearly dependent on

lithium concentration ranging from 200 GPa and 0.27 at zero concentration of lithium to 80 GPa and 0.24 at maximum lithium concentration, respectively. We adopted the value of 4.9 GPa [77] for yield strength and a hardening modulus of 1 MPa to capture the plastic flow. All the elasto-plastic constants (Young's modulus, Poisson's ratio, yield strength, strain hard-ness) are normalized by  $c^{max}RT$ , which is equal to 1.1 GPa at room temperature and their values are given in Table III.

The value of dimensionless parameter,  $\alpha$ , which controls the sharpness of the reaction front by controlling the slope of the increase in diffusivity, is kept at 1.46. For values of  $\alpha$ , between 1.46 to 2, the sharpness of the reaction front starts to decrease. For values greater than 2, the diffusivity coefficient turns negative within the operating concentration limits, which is not physical. The value of  $\kappa$ , which amplifies the diffusion coefficient based on the hydro-static stress, is taken as 0.38. This value is chosen in such a way that the diffusion coefficient becomes two orders of magnitude higher in the stress region than in the bulk. It should be noted that a similar value of  $\kappa$  was previously reported [74]. Haftbaradaran et al. [74] have reported that the value of  $\kappa$  could be dependent on the stress sign, such that a tensile stress decreases  $\kappa$ , while a compressive stress increases it. However, the  $\kappa$  dependency on the stress sign was observed for the stress value range between -20 GPa and 12 GPa, thus considering stress range obtained in the present study (-0.1 and 0.1) we assume constant  $\kappa$ . During the finite element simulation, the normalized computational time step size is initially set to  $10^{-6}$ , which is 24.5  $\mu$ s in actual time and is set to be adaptive.

TABLE III

Simulation parameters with their dimensional and normalized values.

Parameter	Dimensional value	Normalized value	Reference
Lithium concentration	$0 - 3.125 \times 10^5 \text{ mol} \cdot \text{m}^{-3}$	$0 - 1$	[27]
SnO <sub>2</sub> nanowire length	150 nm	1	
Young's modulus	200 Gpa (min conc.) to 80 Gpa (max conc.)	218 (min conc.) to 88 (max conc.)	[77]
Yield stress	4.9 Gpa	5.422	[77]
Expansion coefficient	0.6 (axial direction) 0.45 (longitudinal)	0.6 (axial direction) 0.45 (longitudinal)	[77]
$\alpha$	1.46		this work
$\kappa$	0.38		[74]
Diffusion Coefficient	$9.67 \cdot 10^{-8} \text{ m}^2 \text{ s}^{-1}$		[67]
Activation energy	0.4 eV		[67]

A constant maximum normalized concentration of 1 is applied on the bottom edge of the nanowire, where the source is attached, and the lithium is allowed to diffuse through the in-

ner core. A constant pressure load of 0.5 MPa is also applied on the edge where the source is more firmly attached to the surface at two different regions of 5 nm each. These two regions are at a distance  $L=75$  nm apart. The nanowire is fixed at the geometrical center of the domain to maintain the static equilibrium in translational degrees of freedom.

### 3.2.2 Stress Induced Diffusion in SnO<sub>2</sub> Anodes

In this section, first the validation of the model's hypothesis is realized by comparison of the model's predictions with the previously published experimental data by Huang et al. [67] and Nie et al. [66]. A detailed sensitivity study is also presented at the end of this section. The diffusion and expansion of the SnO<sub>2</sub> nanowire are calculated and compared against the results reported by Huang et al. [67]. It should be emphasized that the exact experimental conditions are not simulated since they are not available in details in order to set up the problem. The comparison provided here is therefore qualitative.

The representative SnO<sub>2</sub> concentration contours, obtained during the simulation are as shown in Figure 17 Both the progress of the lithiation process and the evolution of the sharp boundary are shown for different times. For the times of 5 s, 350 s, 550 s and 950 s, we compare the predicted Li concentration with the previously published data. It is noted that these five times correspond to 0 %, 10 %, 40 % and 90 % of the progress in lithiation front, thus forming a comprehensive picture of the lithiation phenomenon of the SnO<sub>2</sub> nanowire. A good quantitative agreement is obtained between our simulation and the results published by Huang et al. [67], over the complete investigated time range. The error in lithiation time through

the bulk of the nanowire is estimated to be close to 4 %. The formation of striped diffusion regime can be clearly seen in Figure 17.

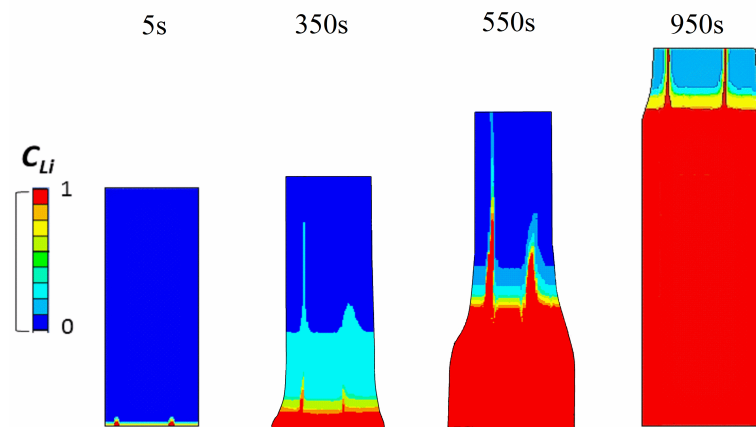


Figure 17. Simulation results showing concentration profile of Li diffusion along the  $\text{SnO}_2$  nanowire for times 5 s, 350 s, 550 s and 950 s

In later discussions in this section, the structural changes and the corresponding stresses are discussed. The stripes are initiated at the points where there is an initial stress defined at the surface of the nanowire. The initial stress facilitates faster diffusion only in that region, which subsequently induces more stress. The induced stress leads to enhanced diffusivity and drives the diffusion further in the same direction, resulting in the formation of stripes. From the results, it can be seen that there is a slight shift from a straight-line path of diffusion.

This is due to the shift in the direction of the induced stresses as lithiation progresses in each stripe. In a later part of this study, the effect of the distance between the stripes on the induced stress build up is analyzed. From Figure 17, it can be clearly seen that multiple-stripe formation process is rather quick. Clear stripe formation starts to occur at around 5s and the thickness of stripes increases with progression of the lithiation. Also from Figure 17 and Figure 18 we can infer that, since the stripe on the left is formed closer to the wall than the stripe on the right it allows for the formation of the stripe to be relatively faster than the stripe on the right-hand side.

In order to shed more lights on the actual influence of lithiation on stresses, the hydrostatic stress contours are plotted in Figure 18.

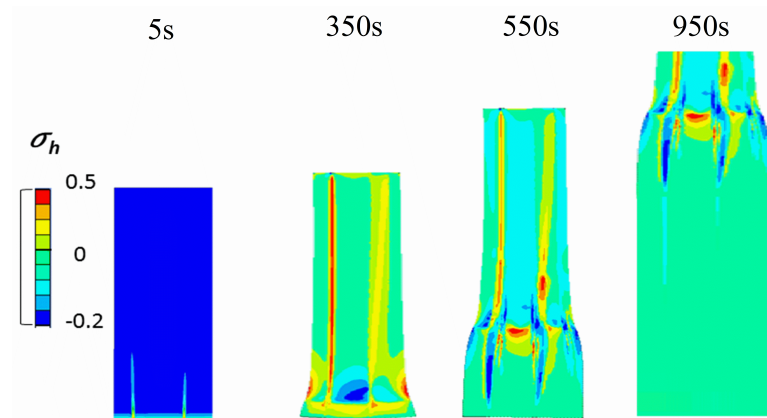


Figure 18. Stress evolution during lithiation of  $\text{SnO}_2$  for 0%, 10%, 40% and 90% lithiation (times 5 s, 350 s, 550 s and 950 s). The values of stress are normalized using Young's modulus of elasticity

From the stress contour, it is evident that the initial stress on the surface induces faster lithiation through a narrow channel, which further induces more stress due to the expansion in these lithiated regions. This induced stress further drives the lithium front to move through these channels.

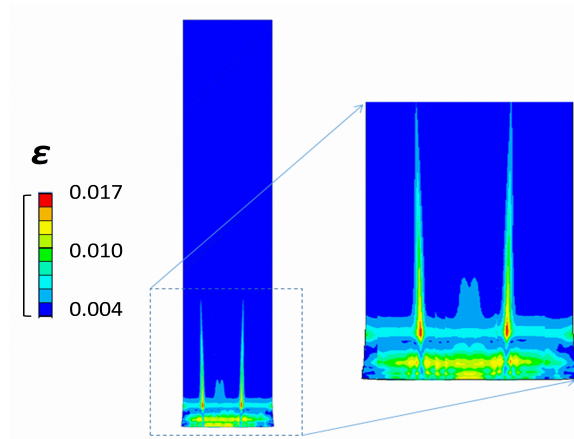


Figure 19. The simulated strain development at the time of 350 s. The zoom-in insertion further highlights the bottom part of the nanowire shown in the left.

The equivalent plastic strain contour at the lithiation time of 350 s is shown in Figure 19, highlighting the bottom part, where the main strain development is observed. As can be seen in Figure 19, closer to the tip of the striped region, the strain is close to 0.0177 while it remains almost zero in other parts of the nanowire, which have not been lithiated yet. The re-

sults show a good quantitative agreement, with a maximum deviation of 4%, to the previously published TEM results by Nie et al. [66], thereby supporting our hypothesis that these striped diffusion regimes form due to the effect of the initial contact stresses. To summarize, the initial lithiation process can be interpreted as follows: Lithiation is initiated at some surface defects or stressed zones and continues along [101] direction. The lithiation induced stress leads to formation of dislocations along the stripes, which further facilitates lithium diffusion into the interior of the nanowire.

### **3.2.3 Parametric Study**

#### **3.2.3.1 Effect of $\kappa$ on Diffusion Coefficient**

The parameter  $\kappa$ , in Equation 3.2, plays a crucial role in the evaluation of the diffusion coefficient. As mentioned above, the product changes activation energy of Li diffusion in  $\text{SnO}_2$ , which reflects the amplification or reduction of the diffusion coefficient. Depending on the magnitude of the stress, parameter  $\kappa$  amplifies the diffusion coefficient in the case of the tensile stress or reduces the diffusion coefficient for the compressive stress. To understand the sensitivity of the diffusion coefficient to  $\kappa$ , the diffusion coefficient is computed for different values of  $\kappa$  as shown in Figure 20(a). Here,  $\kappa$  is first set to zero to capture the change in the diffusivity with no influence of stress (concentration dependency only). The concentration dependency on the diffusivity reduces the diffusivity to a minimum value at a concentration of  $c_{Li} = 0.45$ . To further analyze and understand the dependency of stress on the diffusivity coefficient a surface plot for the diffusivity coefficient, for the entire range of stress in the domain, is generated as shown in Figure 20(b). The result clearly indicates that the value of the

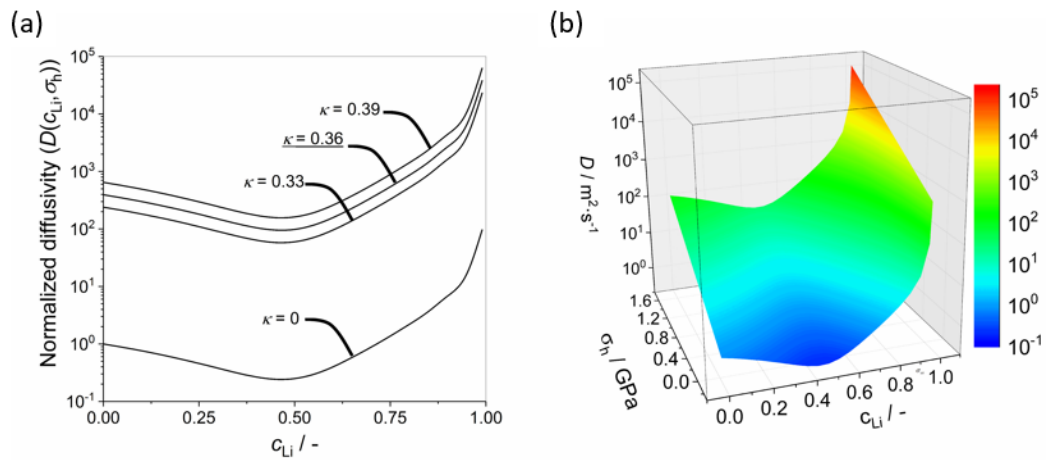


Figure 20. (a) Variation of the diffusivity with concentration for different values of parameter  $\kappa$ . The underlined value of  $\kappa$  is used in this work. (b) Variation of diffusivity with concentration and hydrostatic stress for  $\kappa=0.36$

diffusivity increases by almost two orders of magnitude for a value between the minimum and maximum values of stress. This results in faster ion diffusion that corresponds to the experimental observation by Huang et al. [13].

To quantify the effect of  $\kappa$  on the formation of stripes, simulations were carried out for three different values of  $\kappa$ , starting from zero, which is equivalent to no effect of stress on diffusion. The concentration contours are plotted for the scenarios where  $\kappa = 0$ ,  $\kappa = 0.33$  and  $\kappa = 0.36$  at a time period of 550 s in Figure 21. Based on the results shown in Figure 21, we could see that the rate at which the diffusion happens through the stripes and the diffusion in the bulk changes close to 1% though the change in the value of  $\kappa$  is up to 10%. Also looking at Fig-

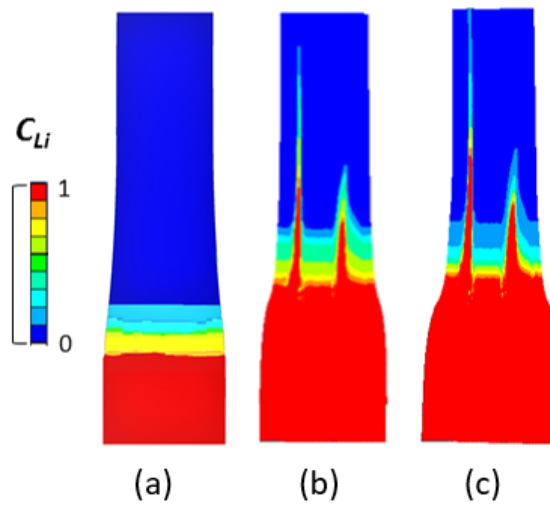


Figure 21. Concentration contours at 550s for different values of  $\kappa$ : (a)  $\kappa = 0$  (b)  $\kappa = 0.33$   
(c)  $\kappa = 0.36$

ure 20(a), it can be seen that the change in value of  $\kappa$  by 10% increases the diffusivity coefficient by much less than an order of magnitude. When the value of  $\kappa$  is zero there is no effect of stress and thus there is no visible formation of stripes, whereas for the case where  $\kappa = 0.33$  the diffusion happens at a much faster rate resulting in clear formation of stripes.

### 3.2.3.2 Effect of the Distance Between the Stressed Zones

The effect of the distance between the stripes is analyzed by reducing the distance between the initial stressed zones, which drive the formation of the stripes, to half the original value. All parameters described in Table III are continued to be used without any changes.

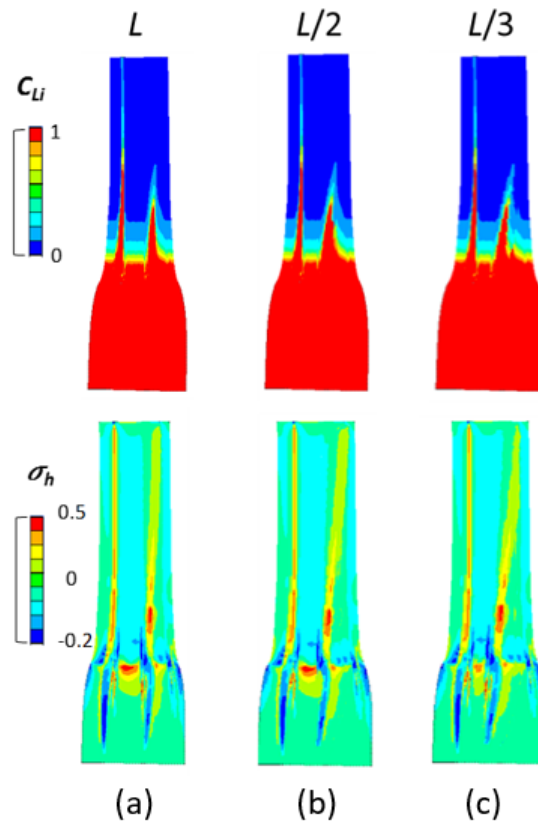


Figure 22. Simulation results showing concentration (top panel) and hydrostatic stress (bottom panel) contours of Li diffusion along the  $\text{SnO}_2$  nanowire at  $t=550$  s for initial distances between stressed points (a) 75 nm (b) 37.5 nm and (c) 25 nm. The values of stress are normalized using Young's modulus of elasticity.

The results from this study, as shown in Figure 22, reveal that though there is still the formation and propagation of stripes, similarly to those shown in Figure 17, there are clear differences. Due to the increase in the build-up of compressive stresses between the striped re-

gions, as a consequence of the expansion of the material in the striped regions, we can observe that the diffusion regime is slightly altered. This development of compressive stresses diminishes the diffusion of lithium into this region.

From the results in Figure 22, it could be observed that the stripes deviate away (at an angle close to 4 degrees) from each other when they are initiated at an initial distance of 37.5 mm instead of 75 mm. This is because the compressive stress buildup between the stripes makes it more difficult for the diffusion closer to the original straight line path. This compressive stress occurs due to the expansion in these stripes resulting in the compression of the region around them. It is also observed that the stripe that is closer to the edge of the nanowire stays almost parallel. This happens due to the lesser compressive stress between the striped region and the edge of the nanowire as the surface or edge is made traction free.

To further analyze and understand the effect of the distance between the initial stressed locations and the effect of the induced stress between the stripes on diffusion, the distance between the stripes is further reduced to 25 nm. Based on the results in Figure 22, we could see that when the distance between the initial stressed locations is further reduced the stripes diverge further away (close to 5 degrees for 37.5nm and close to 7 degrees for 25nm) from each other due to the build up of higher compressive stresses between the stripes.

### **3.3 Summary and Conclusions**

In this work, two widely used physics-based models are implemented to simulate ions intercalation and transport phase transformation and stress generation in the electrode materi-

als. A detailed comparison between the model is presented using the test case of Li diffusion through Si.

The comparisons of the results show that both models provide qualitatively similar accuracy, when concentration gradient is not significant within the electrode. However, concentration field predictions between the CDSM and the PFM models can be significantly different, when there is a large concentration gradient in the narrow reaction front. This is because, in order to create a sharp interface between the two Li-rich and Li-poor phases in the CDSM model, the diffusivity parameter must be a highly non-linear function of concentration. The extent of the non-linearity, however, must be limited in order to prevent non-physical negative values of the diffusivity coefficient. In addition, very large values of the diffusivity coefficient impose severe limitations on the time step size, hence increasing the computational cost. In contrast, in the PFM the interfacial width is controlled by the gradient energy coefficient and the mobility parameter, which is analogous to the diffusivity, is used to describe species diffusion within the phases.

Although both models are found to be appropriate for describing the experimentally observed phenomena (e.g., sharp concentration profile, stress field, etc.), it could be concluded that the PFM is more general and easier to expand than the CDSM. For example, in the alternative battery technologies (e.g., thin films electrodes) there is a need to model several energy minima with varying concentration gradient. This can be easily achieved in the PFM by introducing several gradient energy coefficients and an appropriate free energy functional. Whereas in the CDSM, introducing several highly non-linear diffusivity functions adds to the

complexity of the computational model. However, it should be noted, the CDSM was developed in the ANSYS software, which is well documented, thus its implementation is more straightforward than the PFM.

The present work also extends the CDSM, physics-based finite element model, to investigate the structural evolution during the lithiation of pristine  $\text{SnO}_2$ , since Sn based anodes are other attractive replacements for graphite in high energy density LIBs. The results from the model clearly show formation of striped diffusion regime due to the induced stresses, at low concentrations of Li. To develop the model, it is hypothesized that the formation of striped regimes during the diffusion of Li in the  $\text{SnO}_2$  electrode is due to the local surface defects and localized high contact stresses from the source at the surface of the electrode. The model is developed in the ANSYS Mechanical APDL solver [78] and uses a coupled finite element diffusion and elasto-plastic approach. The results are shown to have a good qualitative agreement with the lithiation time and strain measurements available in the literature. Through the results, it could be understood that the lithiation induced stress leads to formation of dislocations along the stripes, which further facilitates lithium diffusion into the interior of the nanowire validating our hypothesis. The multiple-stripe formation process is rather quick, and the thickness of the stripes increases with the progression of lithiation. Also, the model is tested for the sensitivity of two key parameters and discussed in detail. It could be seen that the rate of formation of the stripes increases with the increase in the value of the parameter  $\kappa$  that controls the effect of stress on the diffusion coefficient. The study further elaborates the effect of distance between the stripes to further elucidate the effect of stress on the diffusion.

It is shown that the stripes diverge from each other because of high compressive stress build up when they are initiated closer to each other. The findings of this study thus provide important insight into the physical basis of micro-structural evolution, morphological changes, and mechanical degradation in SnO<sub>2</sub> electrodes.

## CHAPTER 4

### INTERPHASE SCALE DEGRADATION STUDIES

*Previously published as: (Ramasubramanian, A., Yurkiv, V., Foroozan, T., Ragone, M., Shahbazian-Yassar, R., Mashayek, F., “Lithium Diffusion Mechanism through Solid-Electrolyte Interphase (SEI) In Rechargeable Lithium Batteries”, J. Phys. Chem. C, 2019.)*

The SEI growth rate, structure, composition and resistance significantly depend upon the electrolyte composition. Furthermore, the distribution of intercalated/electrodeposited Li greatly depends on the SEI structure which defines the subsequent electric-potential gradient and the stress field. Thus, the understanding of Li diffusion mechanism and its energetics through the SEI is of imperative importance to understand and improve the performance of Li batteries. For that reason, in this work, we employ the first-principles calculations based on density functional theory to investigate different aspects of Li atoms diffusion through the GB of the SEI. In this work, we consider the most studied, however, not greatly understood SEI of Li-metal batteries (LMBs).

During battery operation, a thin (nanoscale) solid electrolyte interphase (SEI) film grows on the surface of an electrode as a result of the decomposition of an electrolyte. It is generally believed that the SEI provides many beneficial functions to the battery operation, one of which is by controlling Li uniform delivery to the electrode surface, where the charge-transfer reaction occurs. However, as the SEI further grows and expands numerous defects and grain boundaries (GBs) are formed, leading to a significant anisotropic diffusivity of Li towards the

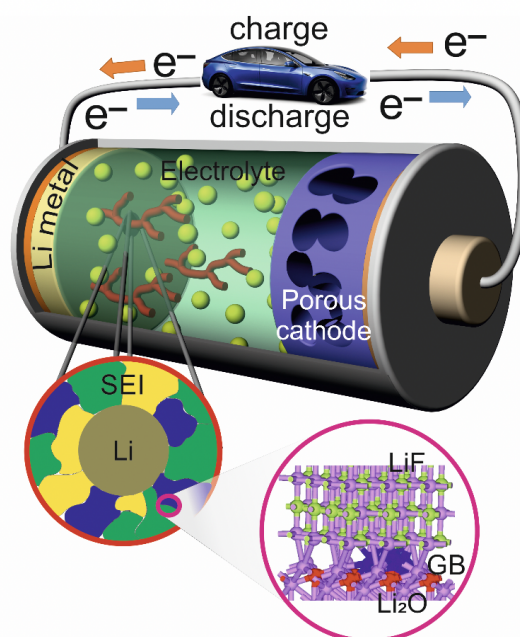


Figure 23. Schematic of SEI grain structures in LMBs and DFT analysis of diffusion pathways in SEI grain structure.

electrode surface. This results in an uneven Li delivery to the electrode/SEI interface leading to undesired phenomena, which cause performance decrease and possibly failure of a battery. These phenomena include random Li electrodeposition and dendrites formation in Li-metal batteries. Figure 23 illustrates the schematic of the SEI GB and provides suitable motivation for current work.

## 4.1 Diffusion of Li Through SEI Grain Structures

In this section, the results of the DFT calculations of Li diffusion through the stable GB are presented. Although many studies have performed to understand parameters such as composition, morphology and thickness of the SEI and their growth mechanisms, very little effort was made to understand the SEI as an ion transport media and the role of GB diffusion. This is due to the fact that the experimental verification of such theories is very challenging. Moreover, almost every SEI component is highly reactive to any form of contaminants. Also, the in-situ experiments require specially designed and precise characterization tools. Thus, computational simulations have become a valuable tool to study the properties and diffusion characteristics of the SEI to understand SEI as a transport media. In this study, we focus on the GB of the SEI employing ab-initio Density Functional Theory (DFT), in an effort to understand and evaluate the stability of SEI, diffusion pathways of Li through SEI and energetics of Li transport.

### 4.1.1 GB Creation

As explained in Section 2.3, first the bulk structures, as shown in Figure 34 (Appendix B), of LiF (8 atoms), Li<sub>2</sub>O (12 atoms) and Li<sub>2</sub>CO<sub>3</sub> (24 atoms) were created and their bulk energies were calculated. Then the slabs with different surface orientations were created, as shown in Figure 35 (Appendix B), to calculate the surface energies and thereby identify the most stable surface for the GB interface. In Table IV, the calculated surface energies of different surface orientations of the SEI components are listed and also compared against the existing literature.

TABLE IV

Surface orientations and surface energies of different SEI components				
Chemical System	Orientation	Surface Energy(meV/Å <sup>2</sup> ) (This work)	Surface Energy(meV/Å <sup>2</sup> ) (From literature)	References
Li <sub>2</sub> O	(100)	75.62	75	[79]
	(110)	56.17	56	[79]
	(111)	31.87	30	[79]
LiF	(001)	21.84	20	[80]
	(110)	51.18	49	[80]
	(111)	54.17	55	[80]
Li <sub>2</sub> CO <sub>3</sub>	(001)	11.85	11.23	[81]
	( $\bar{1}10$ )	18.72	17.47	[81]
	(110)	36.82	35.57	[81]

From the surface energy values, we can infer that the most stable and energetically favorable surfaces for Li<sub>2</sub>O, LiF and Li<sub>2</sub>CO<sub>3</sub> are the (111), (001) and the (001) surfaces respectively.

Though (001)surface of Li<sub>2</sub>CO<sub>3</sub> has a very low energy (11.85 meV/Å<sup>2</sup>), it does not form sta-

ble GBs since they readily reduce electrochemically in the presence of Li [82]. Thus the major GBs of interest are the GBs between LiF/LiF slabs, the GBs in Li<sub>2</sub>O/Li<sub>2</sub>O slabs and the mixed GBs between LiF/Li<sub>2</sub>O slabs. The GBs which contains single crystal structure on either side are created using Coincidence Site Lattice (CSL) theory. The GBs are named using the symbol  $\Sigma$  based on the CSL theory as,

$$\Sigma = \frac{\text{Volume of CSL lattice}}{\text{Volume of unit lattice}} \quad (4.1)$$

Mixed LiF/Li<sub>2</sub>O boundaries are created by joining the minimum energy surfaces of LiF and Li<sub>2</sub>O respectively with minimum possible strain on either slab at the interface. In all cases, the z-direction is perpendicular to the grain boundaries.

#### 4.1.1.1 LiF/LiF GB Creation

The simulation cell containing two LiF (001) ( $\Sigma 3$  and  $\Sigma 5$ ) GBs (Figure 24(a) and Figure 24(b)) is created as follows. First a LiF crystal at optimal lattice constants is rotated 18<sup>0</sup> and cleaved using (001) surface to expose (310) surfaces in the x-direction. A second, mirror-image slab is created by reflecting the first about the x-y plane.

As shown in Figure 24(a) and Figure 24(b), there could be two possible structures based on the location of the mirror plane. The first structure is matched at the lattice point forming a closed GB structure and the second structure is achieved by the mirroring of the slabs slightly (about 1 Å ) away from the coincident lattice points, which forms a slightly open GB structure. It should also be noted that the mirror or junction plane is a (310) plane of atoms

common to both slabs, is found to be energetically less favorable. So, the mirrored slab is shifted by half a lattice constant on the z- direction in order to achieve better stability and more coordination between Li and F atoms on either slab. The z-dimension of the cell is varied to introduce the vacuum of 15 Å .

#### 4.1.1.2 Li<sub>2</sub>O/Li<sub>2</sub>O GB Creation

There are limited electronic structure studies of grain boundaries in anti-fluorite lattice structures of AB<sub>2</sub> stoichiometry relevant to Li<sub>2</sub>O [83–85]. Similar to LiF/LiF GB a simple  $\Sigma 5$  GB is created for Li<sub>2</sub>O by joining (310) facets. But in  $\Sigma 5$  configuration one of its orthogonal surfaces is (001). This is the most stable surface for LiF but is a high energy surface for Li<sub>2</sub>O. The lowest energy facet of Li<sub>2</sub>O is (111). Since the Li<sub>2</sub>O lattice structure is different from that of LiF, the model used in LiF is inapplicable, and the CSL approach has to be reapplied instead.

Based on the CSL theory, taking the (111) direction as the z-axis, the Li<sub>2</sub>O slab was mirrored by a plane that is 60° to the x-y plane and joined to form a  $\Sigma 3$  Li<sub>2</sub>O that has maximum Li-O contacts. This angle is chosen to give a modest system size with best lattice matching with the metal surface supercell. Similar to the  $\Sigma 3$  LiF GB, another structure could be achieved for the Li<sub>2</sub>O GB using the (210) surface, mirrored with x-y plane, forming a  $\Sigma 15$  GB. Figure 24 (c) and (d) show both the achieved GB structures. Both GB structures are then optimized to their respective ground state energies to evaluate the respective GB energies.

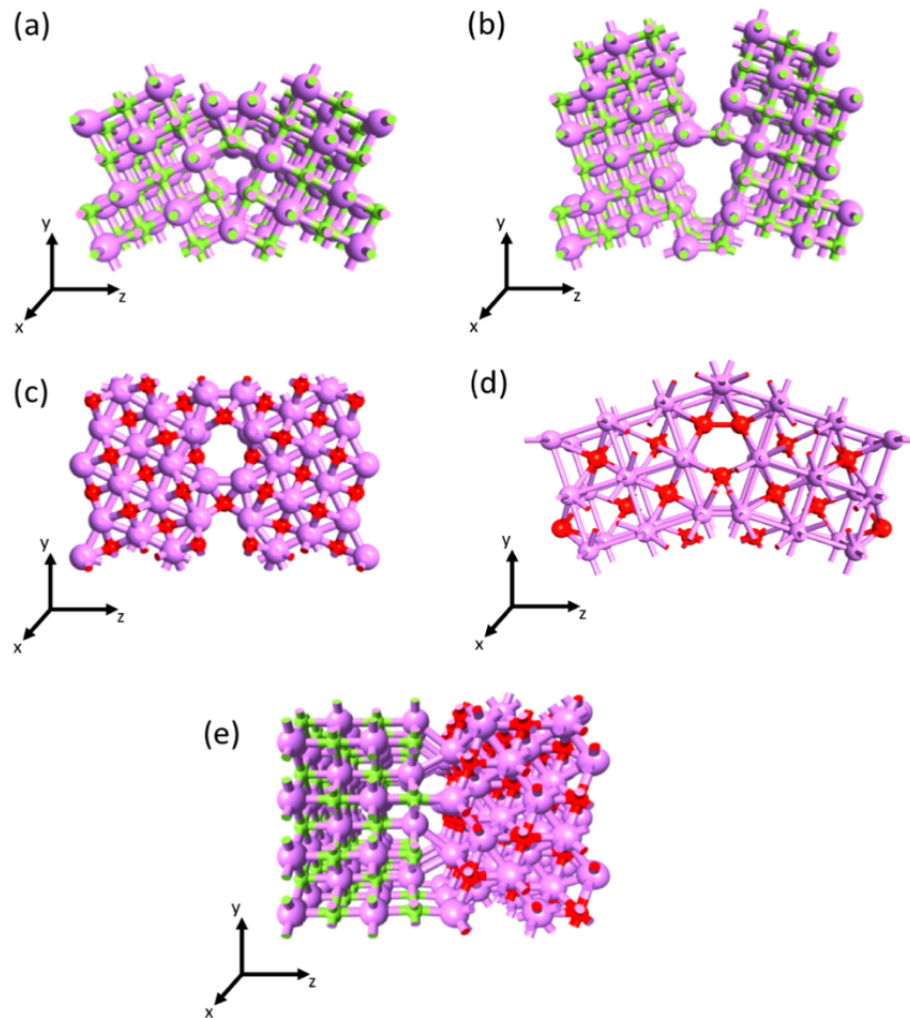


Figure 24. Grain boundary structures formed by LiF and Li<sub>2</sub>O grains. (a) Compact LiF/LiF (310) GB ( $\Sigma 3$ ), (b) open LiF/LiF (310) GB ( $\Sigma 5$ ). (c) Li<sub>2</sub>O/Li<sub>2</sub>O  $\Sigma 3$  GB with (111) oriented surface towards the interface, (d) Li<sub>2</sub>O/Li<sub>2</sub>O  $\Sigma 15$  GB with (210) surface. (e) LiF(001)/Li<sub>2</sub>O(111) GB structure. Pink colored spheres depict Li atoms, red colored spheres show F atoms, and red colored spheres illustrate O atoms.

#### 4.1.1.3 LiF/Li<sub>2</sub>O GB Creation

From the surface studies, we calculated the most stable surfaces of LiF and Li<sub>2</sub>O to be (001) and (111) respectively. The mixed LiF/Li<sub>2</sub>O boundaries are created by joining the two surfaces of a LiF (001) slab on to Li<sub>2</sub>O (111) slabs, as shown in Figure 24(e). The good lattice matching of these two surfaces allow cations (Li<sup>+</sup>) on one material surface to be coordinated to anions (F<sup>-</sup> or O<sup>-</sup>) on the other and form a GB with a low strain value of 2.1% on either slab. The GB is oriented perpendicular to the z direction and the ion positions are optimized as in the previous cases.

From Table V, we can infer that the elastic properties of the GBs have a direct correlation to the the elastic properties of materials. The GB density is evaluated as

$$\rho = \frac{2S}{abc} \quad (4.2)$$

where,  $S$  is the surface area of the interface and  $a$ ,  $b$  and  $c$  are the lattice lengths of the supercell structure. Since the grain boundary is oriented towards the x-direction the value of  $S$  becomes,  $S = ab$ , and the value of becomes,  $\rho = \frac{2}{c}$ . It can be observed that, as the GB density increases the thickness of the grain when compared to the GB is increased and stiffness of the material increases, but this value becomes significant only at very low GB densities (as low as 0.06 [86]). Lower values of GB energy,  $\gamma_{GB}$ , indicate a stronger cohesive bonding between the two grains in contact.

TABLE V

Summary of all the GB structure properties. First column shows the GB composition and notation, second column shows the stoichiometry, third column lists k-point used in the present DFT calculations, fourth column shows the calculated GB energies, fifth column reports the GB density and the last sixth column reports the calculated bulk modulus

Chemical System	Supercell Stoichiometry	K Points	$\gamma_{GB}$ (mJ/m <sup>2</sup> )	GB density (1/Å)	Bulk Modulus (GPa)
LiF/LiF ( $\Sigma 5$ GB)	Li <sub>112</sub> F <sub>112</sub>	5 × 3 × 1	380.79	0.130	76.88
LiF/LiF ( $\Sigma 3$ GB)	Li <sub>68</sub> F <sub>68</sub>	5 × 4 × 1	423.55	0.136	77.25
Li <sub>2</sub> O/Li <sub>2</sub> O ( $\Sigma 3$ GB)	Li <sub>126</sub> O <sub>63</sub>	5 × 5 × 1	688.72	0.166	65.79
Li <sub>2</sub> O/Li <sub>2</sub> O ( $\Sigma 15$ GB)	Li <sub>102</sub> O <sub>51</sub>	3 × 4 × 1	557.47	0.118	64.73
LiF/Li <sub>2</sub> O	Li <sub>120</sub> F <sub>48</sub> O <sub>36</sub>	3 × 3 × 1	288.62	0.124	64.22

From the GB energy,  $\gamma_{GB}$ , it can be clearly identified that the  $\text{Li}_2\text{O}/\text{Li}_2\text{O}(\Sigma 3 \text{ GB})$  structure is energetically much less favorable than the  $\text{Li}_2\text{O}/\text{Li}_2\text{O}(\Sigma 15 \text{ GB})$ . Furthermore, we also observed that the GB structure breaks apart when we add a Li ad-atom into the GB.

#### **4.1.2 Li Diffusion Through GB**

In this section classical DFT simulations are used to obtain the diffusion coefficients of Li-ion through the GBs of major components of the SEI found in LMBs. In addition, since the diffusion coefficients are fitted to the Arrhenius equation, the activation energies ( $E_{act}$ ) and pre-exponential factors  $D_0$  are obtained. These results are then compared against the available experimental data and other computational results. This provides us a better understanding on the interplay between the GBs in SEI compounds and their effect on direction dependent ion migration through GB interface.

##### **4.1.2.1 Li Diffusion Through LiF/LiF GB**

As shown in the previous section, there are two possible GB structures ( $\Sigma 3 \text{ GB}$  and  $\Sigma 5 \text{ GB}$ ) for the  $\text{LiF}/\text{LiF}$ . The migration of a Li atom in the vicinity of the  $\Sigma 3 \text{ GB}$  and  $\Sigma 5 \text{ GB}$  and parallel to the GB plane is studied. The simulation cell with the ad-atom is as shown in Figure 25(a) and Figure 25(b) for  $\Sigma 3 \text{ GB}$  and  $\Sigma 5 \text{ GB}$  respectively.

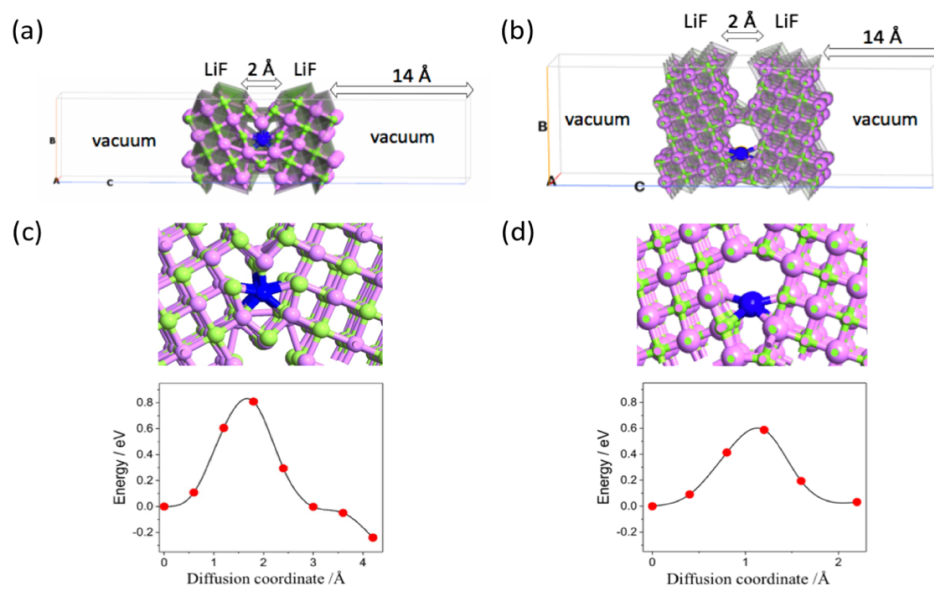


Figure 25. a) Compact LiF/LiF (310) GB ( $\Sigma 3$ ) with Li ad-atom (marked in blue). b) Open LiF/LiF (310) GB ( $\Sigma 5$ ) with Li ad-atom (marked in blue). c) migration barrier for Compact LiF/LiF (310) GB ( $\Sigma 3$ ). d) migration barrier for Open LiF/LiF (310) GB ( $\Sigma 5$ ).

From the migration barriers as shown in Figure 25(c) and (d), it could be seen that the barrier energy for Li to diffuse through the GB is lower in the case of open  $\Sigma 5$  GB than the dense  $\Sigma 3$  GB. and suggested that diffusion in LiF the cause rate limitations in Li ion diffusion. The energy barriers of 0.62 eV and 1.03 eV for open and dense structures show that the open structure allows for better diffusion through the GB than the dense structure. This might be due to lesser interaction from neighboring atoms in  $\Sigma 5$  GB.

### 4.1.3 Li Diffusion Through $\text{Li}_2\text{O}/\text{Li}_2\text{O}$ GB

This section examines Li diffusion in the simulation cell containing a  $\text{Li}_2\text{O}$  crystal with  $\Sigma 15$  GB system as shown in Figure 26. In Figure 26(a) the simulation cell used for the NEB calculation with the GB and the Li ad-atom placed at the GB region.

From Figure 26(b) it could be seen that the migration barrier for Li diffusion through the grain boundary structure is 0.78 eV which suggests that the diffusion through this grain boundaries in  $\text{Li}_2\text{O}$  is slightly more hindered when compared to that of GBs in LIF.

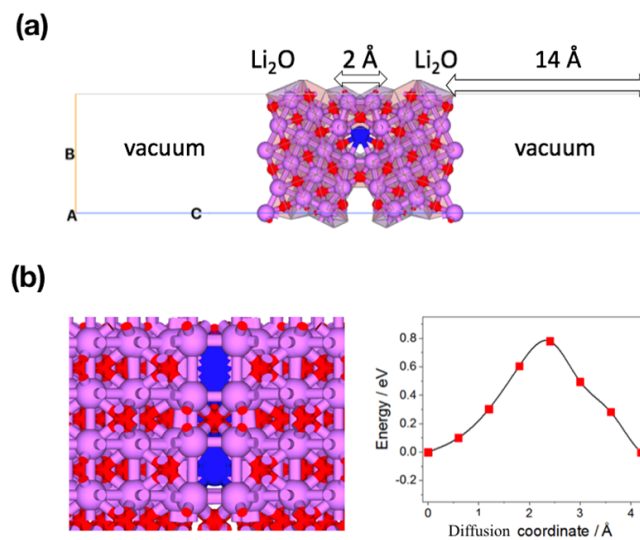


Figure 26. a)  $\text{Li}_2\text{O}/\text{Li}_2\text{O}$  (210) GB ( $\Sigma 15$ ) with Li ad-atom (marked in blue). b) diffusion direction and migration barrier for  $\text{Li}_2\text{O}/\text{Li}_2\text{O}$  (310) GB ( $\Sigma 15$ ).

#### 4.1.4 Li Diffusion Through LiF/Li<sub>2</sub>O GB

This section examines Li diffusion in the simulation cell containing a Li<sub>2</sub>O crystal on one side and LiF on the other with a GB interface. The migration of a Li atom in the vicinity of the GB and parallel to the GB plane is studied. But unlike the case of LiF/LiF GBs or Li<sub>2</sub>O/Li<sub>2</sub>O GBs, in this structure there are different channels that could act as possible minimum energy paths for Li diffusion.

From Figure 27(b), (c) and (d) it could be seen that the migration barrier for Li diffusion through the grain boundary structure ranges between 0.45 eV to 1 eV in the three paths and the minimum energy path is as shown in Figure 27 (c) and the migration barrier is 0.45 eV. Since diffusion is driven by the activation energy of the process, a small error in energy barriers translate into large uncertainties in the diffusion coefficients. And consideration of GBs and diffusion through GBs alters these migration barriers significantly. In the literature, Density functional theory (DFT) calculations have allowed comparison of Li-ion transport through the bulk structures of typical SEI materials [87]. One of the most reported inorganic component that is found in SEI is LiF [88–90]. This in-organic compound has been observed in Li metal anodes. Yildirim and co-workers [89] reported that its cation diffusivity is much lower than the other SEI inorganic compounds, and suggested that diffusion in LiF the cause rate limitations in Li ion diffusion; they used density functional theory (DFT) calculations to determine diffusion pathways and nudge elastic band (NEB) method to calculate energy barriers of diffusion; they found that in bulk LiF structures, diffusion of vacancies were energetically more favorable than interstitials, and reported energy barriers of 0.73 for the for neutral

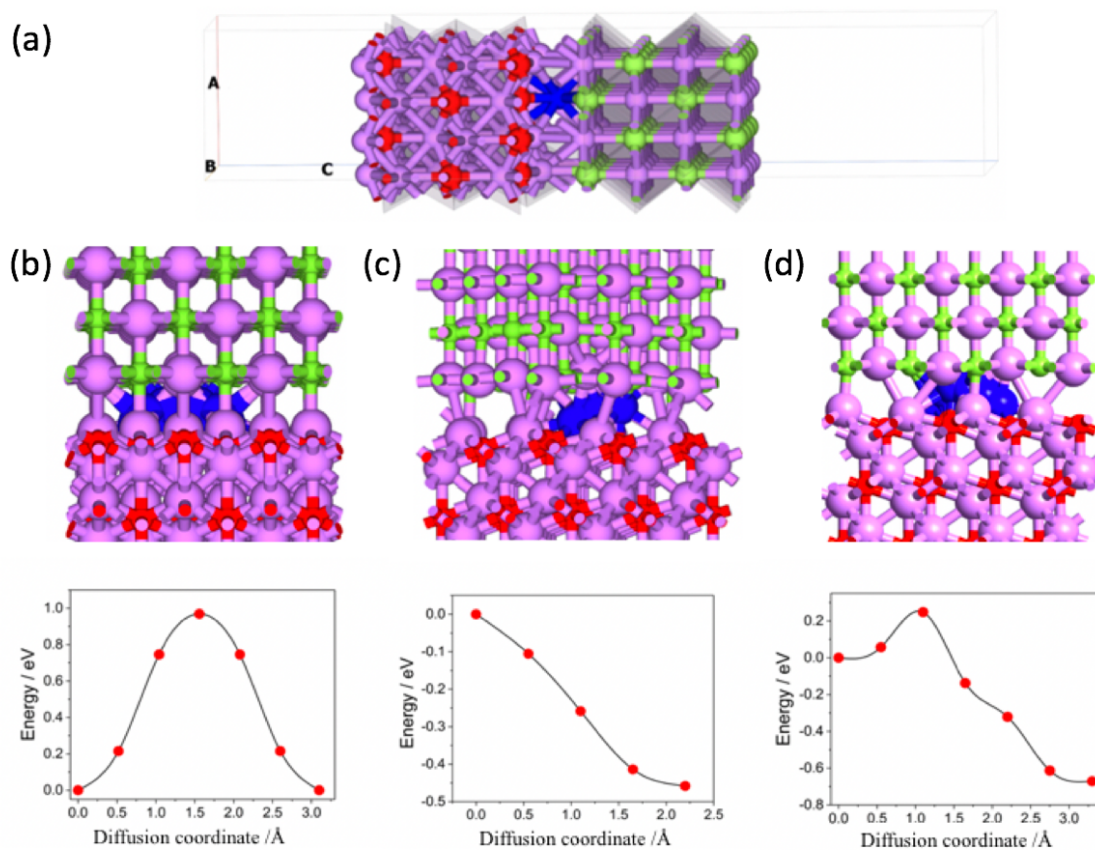


Figure 27. a) LiF/Li<sub>2</sub>O GB with Li ad-atom (marked in blue). b) c) Diffusion direction (path 1) and migration barrier for LiF/Li<sub>2</sub>O GB. d) Diffusion direction (path 2) and migration barrier for LiF/Li<sub>2</sub>O GB. e) Diffusion direction (path 3) and migration barrier for LiF/Li<sub>2</sub>O GB.

vacancies and 1.09 eV for the neutral Schottky vacancies. The diffusion coefficients associated to the energy barriers are in the range of  $10^{-26}$  to  $10^{-20}$   $\text{m}^2\text{s}^{-1}$ .

Only a very few theoretical studies reported diffusion barriers in  $\text{Li}_2\text{O}$  at battery operating temperatures [87, 91]. Chen et al. [87] investigated the electronic structure of  $\text{Li}_2\text{O}$  and using NEB analyzed the vacancy-assisted diffusion. In this work they showed that the electronic structure of  $\text{Li}_2\text{O}$  has an insulating character with a diffusion barrier of 0.15 eV. Also, Tasaki et. al, [92] studied diffusion in  $\text{Li}_2\text{O}$  and found the diffusion coefficients for Li diffusion in the range of  $1.7 \times 10^{-16} \text{m}^2/\text{s}$ .

Based on all the evaluated values of migration barriers, the diffusion coefficients though all the GB systems are evaluated and listed in Table VI. On comparing the energy barrier values and the computed diffusion coefficients, it could be seen that the diffusion through GBs act as a rate limiting step and is significantly faster (around 2 orders of magnitude) through certain GBs.

## **4.2 Stability of SEI GB on the Li Surface**

As shown in the previous section, the numerous defects and grain boundaries (GBs) in the SEI results in a significant anisotropic diffusion of Li towards the metal surface, leading to random electrodeposition and dendrites formation. However, it is also imperative to understand the stability of such GB structures on the electrode surface and the energy required to cleave across these defects to effectively understand the location of the nucleation of these dendrites.

TABLE VI

Summary of all activation energies and Diffusion coefficients

Chemical System	Activation energy ( $E_{act}$ ) eV	Pre-exponential factor $D_0 = ga^2\nu$ ( $m^2/s$ )	Diffusion coefficient ( $m^2/s$ )
LiF/LiF( $\Sigma 5$ GB)	0.68	$1.8 \times 10^{-15}$	$1.17 \times 10^{-17}$
LiF/LiF( $\Sigma 3$ GB)	1.03	$1.8 \times 10^{-15}$	$7.14 \times 10^{-25}$
Li <sub>2</sub> O/Li <sub>2</sub> O( $\Sigma 15$ GB)	0.78	$5.4 \times 10^{-13}$	$3.69 \times 10^{-19}$
LiF/Li <sub>2</sub> O	0.45	$3.6 \times 10^{-14}$	$3.87 \times 10^{-15}$

In recent years, lithium metal-based batteries (LMBs) have been regarded as the most attractive alternatives to lithium-ion batteries (LIBs). [4, 6] A lithium metal anode has a high theoretical capacity of 3860 mAh/g and the lowest electrochemical potential ( $-3.04$  V). [93, 94] However, their commercial application is severely hampered by dendrite growth and low Coulomb efficiency during the charging and discharging processes. Among these problems, growth of dendrites is regarded the most challenging. Lithium dendrites are responsible for thermal runaway, fires and explosions in lithium metal anodes. Thus in this work, the Li surface is chosen as the electrode surface.

First the GB structures of LiF/LiF, Li<sub>2</sub>O/Li<sub>2</sub>O, and LiF/Li<sub>2</sub>O, as shown and discussed in our previous sections, are created, and their total energies are calculated. Then the Li slabs

with different surface orientations (001 and 110) are created to identify the most stable surface for the GB interface. The interfaces are designed in such a way that the GB is oriented perpendicular to the Li slab, which renders only two possible orientations for the interface. It was identified that 001 surface of Li matches well with LiF/LiF, and LiF/Li<sub>2</sub>O GB and 110 surface of Li matches well with Li<sub>2</sub>O/Li<sub>2</sub>O GB. Since the SEI films are formed from the decomposition of electrolytes are kinetically controlled self-assembled structures, they are not necessarily the most energetically favorable. To obtain a metastable structure the Li interface with each of the SEI GB structures is then systematically analyzed by manually adding Li into these structures at specific locations close to the interface, specifically at the TPB and other open sites.

The Atomistic Tool Kit (ATK), is used to build the GB, where the Interface Builder tool allows to analyze all possible interfaces between two slabs. The algorithm searches all possible repetitions and rotations (with every 2° steps) of the two surfaces in order to find a common supercell with minimal strain. Since there are tens of possibilities between two different grains, we apply specific cut-off conditions, such as the interface width should be 2 Å, and the strain of each surface should not be more than 5%. In addition, the natural limitation of DFT method eliminates configurations with more than 350 atoms per structure.

#### **4.2.1 LiF/Li<sub>2</sub>O GB on Li Surface**

The LiF/Li<sub>2</sub>O GB on Li is first analyzed, as shown in Figure 28(a), as it gives the rate-determining step for Li diffusion across the SEI grain structure and provides a faster diffusion pathway for Li diffusion. The interfacial arrangement of the LiF/Li<sub>2</sub>O interface on Li, where the Li<sub>2</sub>O and

LiF layers are placed with the oxygen and fluorine facets exposed to the Li metal, provides a stable conformational structure.

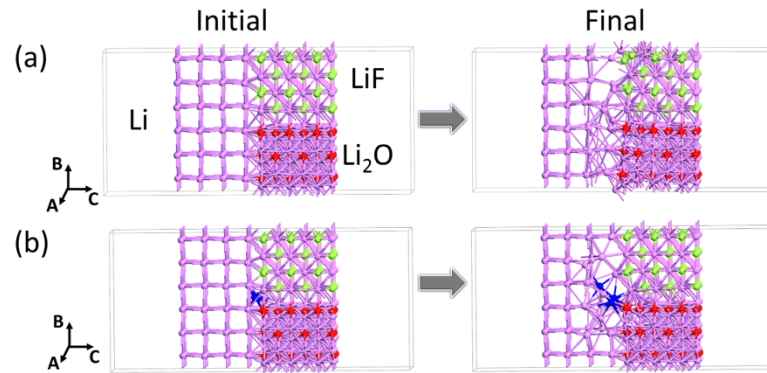


Figure 28. (a) Initial and final optimized structures of LiF/Li<sub>2</sub>O GB on Li surface with no added Li at the TPB, (b) Initial and final optimized structures of LiF/ Li<sub>2</sub>O GB on Li with added Li at TPB. Pink colored spheres depict Li atoms; red colored spheres show O atoms and green colored spheres show F atoms. The added Li atoms are shown in blue.

From the final optimized configuration, it could be seen clearly that the topmost Li-metal layer undergoes a significant amount of strain and becomes part of the LiF structure by shifting electronic charges into the LiF sublattice. The existence of GBs at the solid–solid interfaces allows electron transfer to the LiF or Li<sub>2</sub>O upon contact and significant rearrangement at the TPB and LiF/Li<sub>2</sub>O structures resulting in an unstable configuration.

The growth and stability of SEI are highly kinetically driven processes and to achieve a metastable state and systematically evaluate the nucleation of dendrites we attempt to insert Li incrementally at the TPB interfaces, starting with one Li ad atom as shown in Figure 37, (Appendix B). On addition of Li at the TPB sites, it can be observed that the rearrangement on the LiF/ Li<sub>2</sub>O slab is minimal and the stability of the structure is improved. In order to visualize the reduction of rearrangement on Li surface due to addition of Li, the case with 3 added Li ad atoms is shown in Figure 28(b)

#### **4.2.2 Li<sub>2</sub>O/Li<sub>2</sub>O GB on Li Surface**

For Li<sub>2</sub>O/Li<sub>2</sub>O GB, to achieve the TPB structure, the structure search method using ATK, as shown in the methodology section, is used and it resulted in a structure equivalent to a strained BCC Li structure for the Li slab, cleaved along its (110) plane, and has a surface energy closer to the (001) Li surface, as shown in Figure 29(a). Similar to LiF/Li<sub>2</sub>O GB structures, the Li<sub>2</sub>O/Li<sub>2</sub>O GB on Li interfaces show a significant distortion in the first layers of Li and the Li<sub>2</sub>O/Li<sub>2</sub>O GB, as shown in final configuration of Figure 29(a). On further addition of Li at the TPB sites, it can be observed that a similar trend to LiF/Li<sub>2</sub>O GB is followed and the rearrangement on the Li<sub>2</sub>O/Li<sub>2</sub>O GB slab is minimized resulting in improved stability of the structure, rendering it metastable.

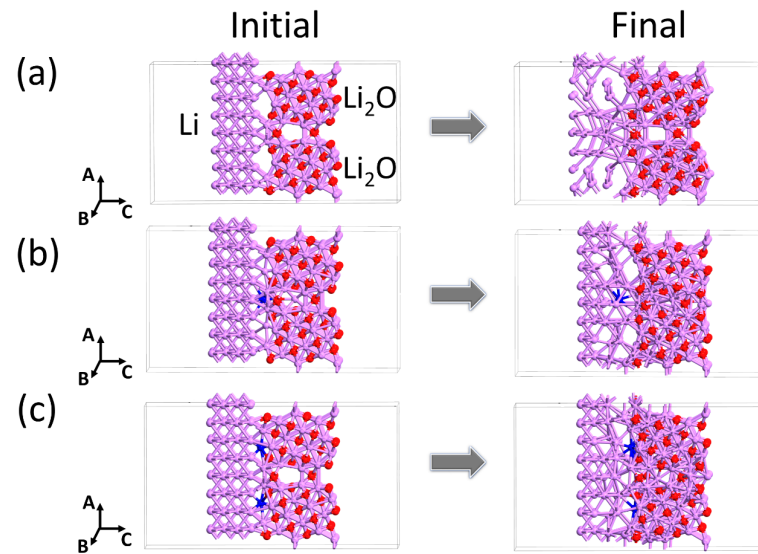


Figure 29. (a) Initial and final optimized structures of  $\text{Li}_2\text{O}/\text{Li}_2\text{O}$  GB on Li surface with no added Li atom at the TPB, (b) Initial and final optimized structures of  $\text{Li}_2\text{O}/\text{Li}_2\text{O}$  GB on Li with added Li at TPB, (c) Initial and final optimized structures of  $\text{Li}_2\text{O}/\text{Li}_2\text{O}$  GB on Li with added Li at other sites in the interface. Pink colored spheres depict Li atoms, and red-colored spheres show O atoms. The added Li atoms are shown in blue.

The increment of number of Li ad atoms and its effect on Li surface is shown in Figure 38 of the Appendix B. Since  $\text{Li}_2\text{O}/\text{Li}_2\text{O}$  GB has fractional surfaces of  $\text{Li}_2\text{O}$ , more possible locations for Li insertion are present in these TPB structures unlike  $\text{LiF}/\text{Li}_2\text{O}$  based TPB structures, as shown in Figure 29(b) & Figure 29(c)

### 4.2.3 LiF/LiF GB on the Li Surface

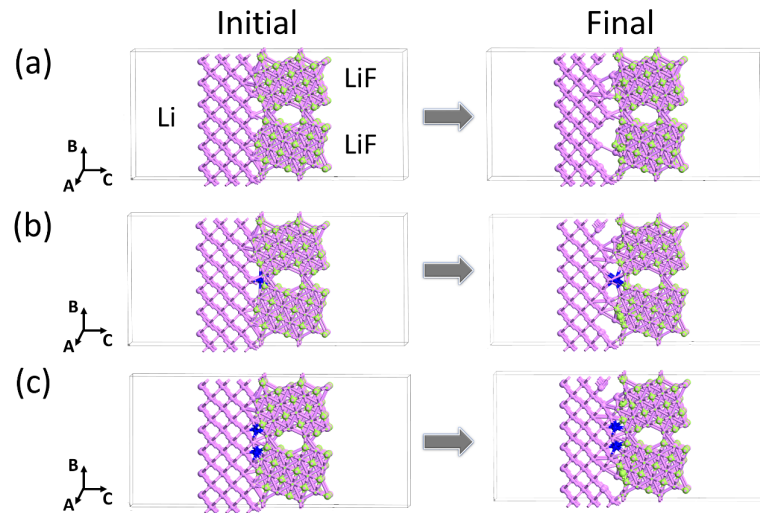


Figure 30. (a) Initial and final optimized structures of LiF/LiF GB on Li surface with no added Li at the TPB, (b) Initial and final optimized structures of LiF/LiF GB on Li with added Li at TPB (c) Initial and final optimized structures of LiF/LiF GB on Li with added Li at other sites in the interface. Pink colored spheres depict Li atoms, and green colored spheres show F atoms. The added Li atoms are shown in blue.

The initial as constructed and the final relaxed interfacial supercells of LiF/LiF GB structures on Li metal surface are as shown in Figure 30(a) (Initial and Final). In contrast to the LiF/Li<sub>2</sub>O GB and Li<sub>2</sub>O/Li<sub>2</sub>O GB, the relaxed LiF/LiF GB on Li interfaces experiences

lesser lattice distortion, and only a small bending of the atomic layer near interfacial region is observed. However, a similar trend of reduction in distortion with the SEI structures is observed when Li atoms are added near the interface at the TPB sites, as shown in Figure 30(b) & Figure 30(c).

#### 4.2.4 Stability of SEI Grain Structures on the Li Surface

To further analyze the stability of different SEI grain structures on Li surface and compare them against each other the per atom binding energy ( $E_B$ ) of Li in the TPB structures are calculated as computed overpotential ( $V$ ). The overpotential is computed as shown in Equation 4.3

$$V = -\frac{[E_B - n_i E_{Li}]}{n_i |e|} \quad (4.3)$$

We believe that the usage of per atom binding energy would be a good quantitative measure for comparison since it subtracts the energy of Li and removes the effect of averaging. In Table VII, the energetics of all the analyzed configurations are shown for all the three combinations of SEI components on Li surface. Although, by classical definitions, overpotentials arise from kinetic constraints, the overpotential,  $V$ , that is defined in this work is a numerical form of the insertion energy and broadly corresponds to that of broadly corresponds to that of the description provided in [95].

TABLE VII

Binding energy based overpotential for different SEI grain structures on Li surface			
Chemical System	Configuration	Total Energy per atom (eV/atom)	Overpotential (V)
LiF/ Li <sub>2</sub> O on Li	With no added Li	-3.632	NA
	With one added Li at TPB	-3.711	-1.51
	With two added Li at TPB	-3.763	-1.49
	With three added Li at TPB	-3.772	-1.47
Li <sub>2</sub> O/ Li <sub>2</sub> O on Li	With no added Li	-3.721	NA
	With one added Li at TPB	-3.770	-1.44
	With two added Li at TPB	-3.791	-1.42
	With two added Li at Li/SEI inter- face	-3.813	-1.40
LiF/ LiF on Li	With no added Li	-3.812	NA
	With one added Li at TPB	-3.880	-1.38
	With two added Li at TPB	-3.933	-1.37
	With two added Li at Li/SEI inter- face	-3.951	-1.36

The comparison of overpotentials due to Li addition at these interface structures illustrate that the LiF/LiF GB is the most stable structure on the Li surface of the three, followed by Li<sub>2</sub>O/Li<sub>2</sub>O and lastly the LiF/ Li<sub>2</sub>O grain structure on Li. This mechanical and electrochemical stability of LiF compared with Li<sub>2</sub>O could be essential in explaining the relative morphological stability and better cycling of Li metal anodes with electrolytes such as LiPF<sub>6</sub>, which are known to produce LiF during SEI formation.

From Table VII, it is also evident that by adding Li on to the interface at specific locations the stability of the SEI structure on the Li surface is improved. This is marked by the reduction in the overpotential values.

To qualitatively compare the improvement in the stability, the isosurfaces of charge densities are plotted, specifically close to the interface, and the interaction at the interface between the SEI and the Li slabs is observed. The isosurface scale is chosen to be 0.001 e/Å<sup>3</sup> for all the structures analyzed. In the charge density isosurface, yellow indicates regions of charge gain, and blue indicates regions of charge loss. Figure 31(a) and Figure 31(b) show the charge density isosurfaces of the optimized structures shown in Figure 28. The highly electronegative fluorine and oxygen lose charge and the Li closer to the interface moves towards the interface and gains the charge. From the structures shown in Figure 31 we observe more interaction at the interface after adding additional ad-atoms to the structure.

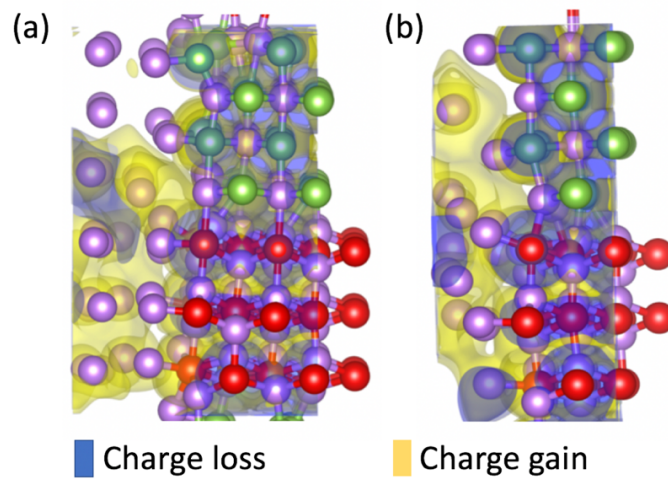


Figure 31. Charge density difference maps of LiF/Li<sub>2</sub>O GB on Li surface, (a) with no added Li (b) with added Li at the TPB. Purple colored spheres depict Li atoms; red colored spheres show O atoms and green colored spheres show F atoms. The isosurface scale is chosen as

$$0.001 \text{ e}/\text{\AA}^3$$

In Figure 32 (a-c) and Figure 33 (a-c) the electron density maps of the Li<sub>2</sub>O/ Li<sub>2</sub>O GB and LiF/LiF GB on the Li surface are shown, respectively. In these structures, addition of Li at the TPB improves the interaction and electron transfer at the interface making it more favorable. However, since the GB structures of SEI are made of fractional surfaces of LiF and Li<sub>2</sub>O, there is still lesser interaction near the top and bottom of the TPB, which is further improved by adding more Li into these sites.

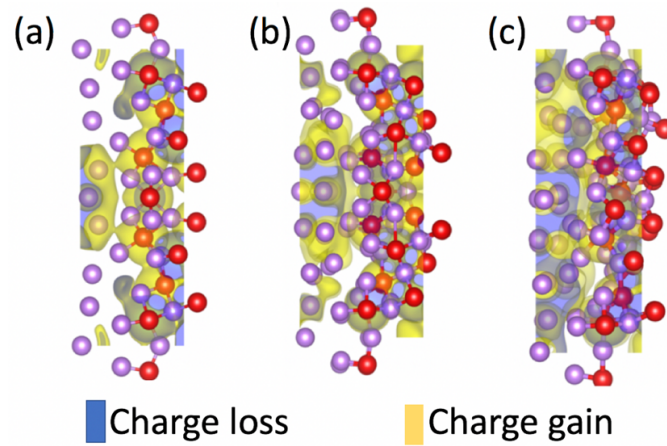


Figure 32. Charge density difference maps of  $\text{Li}_2\text{O}/\text{Li}_2\text{O}$  GB on Li surface (a) with no added Li (b) with added Li at the TPB (c) with added Li at other interfacial sites. Purple colored spheres depict Li atoms and red colored spheres show O atoms. The isosurface scale is chosen

as  $0.001 \text{ e}/\text{\AA}^3$ .

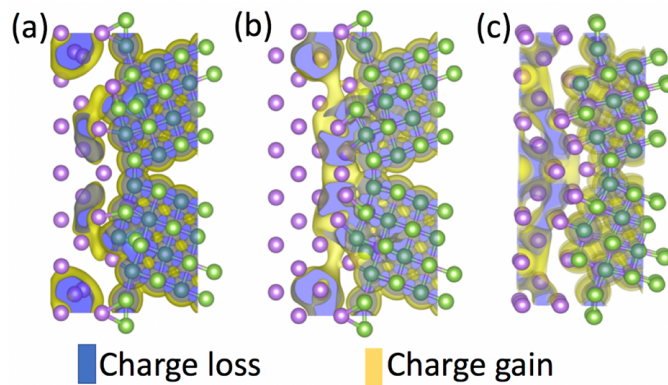


Figure 33. Charge density difference maps of  $\text{LiF}/\text{LiF}$  GB on Li surface (a) with no added Li (b) with added Li at other interfacial sites (c) with added Li at the TPB. Purple colored spheres show Li atoms and green colored spheres show fluorine atoms. The isosurface scale is

chosen as  $0.001 \text{ e}/\text{\AA}^3$ .

#### 4.2.5 Excess Energy and Stability of TPB

To evaluate the effect of the SEI layer on suppression of the Li dendrite, the favorability criterion for the Li dendrite growth along the TPB is defined based on the energy analysis.

When the Li dendrite grows along the grains of brittle SEI, work is needed to form new interface while the strain energy at the tip of the grain boundary will be released. Since, the TPBs are the weakest points in SEI structures the excess energy due to TPB is the energy required by the dendrites to nucleate through the SEI grain structures.

Since the minimum energy surfaces are generally the most stable and naturally formed surfaces in the grain structure, the surface energy per unit area of a slab is calculated. The surface energy is calculated as shown in Equation 2.18, in chapter 2. The calculated surface energies for the SEI grain structures is shown in Table IV and are used in this work to calculate the GB energies. Similarly, the GB energy density for all the interfaces in the TPB structure are evaluated. The GB energy density is calculated as shown in Equation 2.19, in Chapter 2. The interfacial GB energies for the interfaces between SEI and Li are calculated using the same relation as shown in Equation 2.19, by assuming the SEI (LiF/LiF, Li<sub>2</sub>O/Li<sub>2</sub>O or LiF/Li<sub>2</sub>O) as one slab and Li as the second slab. The GB interfacial energy for the SEI/Li interfaces are as shown in Table VIII. The GB energy densities, as shown in Table V and Table VIII, suggest that LiF/LiF GB has a much better stability when compared to Li<sub>2</sub>O/Li<sub>2</sub>O both as a GB and also on Li metal surface, To further enhance this understanding and address the energies specific to the TPB, the total excess energy due to the formation of the TPB is computed with respect to the energy of the pristine slabs. The excess energy of TPB and the sta-

TABLE VIII

Surface orientations and GB energies of different SEI GB on Li surface			
Chemical System	Li slab surface	GB Energy $\gamma_{GB}$ (mJ/m <sup>2</sup> )	GB density (1/Å)
LiF/LiF on Li	(001)	28.34	0.161
Li <sub>2</sub> O/Li <sub>2</sub> O on Li	(110)	75.42	0.153
LiF/Li <sub>2</sub> O on Li	(001)	11.65	0.148

bility of the interfaces are calculated based on the cohesive energies and the GB interface energies of the SEI components and Li metal. The excess energy due to the formation of TPBs is found using Equation 2.21, The greater is the value of  $\gamma_{TPB}$ , the higher is the stability of the SEI grain structure on Li.

On the basis of Equation 2.21, for a given SEI grain structure, the excess energy due to TPB decreases with the increase in GB energy densities of all the interfaces that form the TPB and the cohesive energies of the SEI components. The excess energy of TPB is calculated to be -20 eV/Å for LiF/LiF GB on Li surface, 4.08 eV/Å for Li<sub>2</sub>O/Li<sub>2</sub>O on Li surface and -7.13 eV/Å for LiF/ Li<sub>2</sub>O on Li surface. Although, based on the overpotential, as shown in Table VII, LiF/Li<sub>2</sub>O is less stable on Li surface than Li<sub>2</sub>O/Li<sub>2</sub>O, the excess energy of TPB in Li<sub>2</sub>O/Li<sub>2</sub>O on Li surface makes it more susceptible for dendritic nucleation. A strain energy

per unit length of  $4.08\text{eV}/\text{\AA}$  ( $\text{Li}_2\text{O}/\text{Li}_2\text{O}$  on Li TPB) is required at the tip of the dendrite to penetrate through the TPB and crack open the GB and form a stable dendrite.

A stronger cohesive bonding between the LiF/LiF slab and Li indicates that it is much more favorable to have LiF/LiF grain structures on the surface of Li than  $\text{Li}_2\text{O}/\text{Li}_2\text{O}$  and LiF/ $\text{Li}_2\text{O}$ . However, since there are various reduction processes that compete with each other on the formation of SEI, the formation and growth of SEI are kinetically driven and are often constrained due to the presence of other grains. They can result in some less stable  $\text{Li}_2\text{O}/\text{Li}_2\text{O}$  and LiF/ $\text{Li}_2\text{O}$  forming at the Li surface.

### **4.3 Summary and Conclusions**

The SEI growth rate, structure, composition, and resistance significantly depend upon the electrolyte composition. Furthermore, the distribution of intercalated/electrodeposited Li greatly depends on the SEI structure, which defines the subsequent electric potential gradient and the stress field. In this work, ab-initio DFT based calculations are implemented to understand the distribution of intercalated Li in the SEI grain structures and the stability of SEI grain structures on Li surface. This provides a detailed understanding on ions intercalation and dendritic nucleation on the electrode materials. Among the studied GBs, the fastest Li diffusion rate is observed for the heterogeneous LiF/ $\text{Li}_2\text{O}$  GB, comparing to the homogeneous LiF/LiF and  $\text{Li}_2\text{O}/\text{Li}_2\text{O}$ . This is due to the fact that Li multi-atoms coordination inside the GB is a very favorable structure leading to the multi-atom hopping mechanism more advantageous than any other mechanisms.

To understand the stability and the mechanical behavior of the SEI/Li interface, interfacial supercells were constructed by matching the two important inorganic SEI components, LiF and Li<sub>2</sub>O, to Li metal, and studied using DFT. Three different GB structures are studied, and their interface atomic and electronic structures are carefully analyzed. Also, the excess energies required for the SEI components to crack along their grain boundary (GB) defects are investigated. The initial observation of these structures suggests that there is a significant rearrangement in the interfacial layers (first few layers) of Li. The system reaches a meta-stable state when more Li is added to the GB and/or to the triple-phase boundary (TPB) between the GB and Li surface. The energetics from the DFT calculations vary significantly depending upon the grain structures, with LiF/LiF grain structures being the most stable and LiF/Li<sub>2</sub>O being the least stable. The calculated energies, with and without vacancies, The calculated interfacial energy and work of adhesion of each interface revealed that the LiF/LiF is the most stable on Li metal surface followed by Li<sub>2</sub>O/Li<sub>2</sub>O, and the least stable is LiF/Li<sub>2</sub>O GB.

## CHAPTER 5

### SUMMARY AND FUTURE WORKS

This work aims to gain a fundamental understanding of mechano-electrochemical processes occurring during Li interaction in LIBs by developing and applying numerical computational methods beyond the-state-of-the-art methodologies. Even though these processes are well-documented thanks to the prior large number of laboratory tests and field trials, the origin of each mechanism is still not well understood, especially those linked to the nano-scale. The interplay of mechanics, electrochemistry and multi-phase transport of Li ions in the electrode is rather complex and non-intuitive. Therefore, in the present work, a combination of multi-scale modeling with in-house experimental measurements to enhance a fundamental understanding of relevant processes is presented. This gives us an opportunity to fill a fundamental gap, and it is an important contribution to further LIBs technologies for robust and long-lasting operation.

At the particle scale, the design of new electrode materials depends greatly on how the lithiation reaction propagates into them. Therefore, this work helps in providing a detailed understanding of the lithiation mechanism which is central to improving the performance of electrode materials during the operation of LIBs through the developed continuum scale computational models. In this work, two widely used physics-based models are implemented to simulate ions intercalation and two different electrode materials (Si and SnO<sub>2</sub>) are analyzed. The analyzed stress and morphological changes are compared to TEM experimental measure-

ments to validate the models and the underlying hypothesis about the characteristics shown by these materials during Li insertion. The continuum models are compared against each other on the problem of the isotropic expansion in Si electrodes and are extended to more complicated cases with anisotropic intercalation. From a theoretical standpoint, in the CDSM model, thermally induced state in the form of stress or strain does not affect thermal diffusivity. The diffusivity only evolves due to concentration (temperature) gradient, whereas the PFM captures the effect of stresses on mobility through constitutive relations. Based on this comparison, the need to implement stress effects on diffusion in the CDSM model has been understood. Thus, the CDSM model is further extended to capture the effects of stress on diffusion using Sn-based electrode materials.

The results from the FE models have also provided very good insights regarding the mechanism of failure and design improvements for the growth of these nano sized electrodes for high-capacity Li-ion batteries. The origin of lithiation induced anisotropy requires further discussion. Lithium diffusion in Si is isotropic in amorphous phase. However, crystalline Si has a directional dependency on diffusion which leads to faster diffusion rates and slips across the different orientations. This marks the onset of failure in these electrodes. In case of Sn based electrodes, although there are no directional dependencies the dislocations (pipe dislocations forming the stripes) are generated due to the localized stresses on the surface due to surface defects and roughness.

At the interphase scale, the modeling work is done using the DFT method to capture the ion diffusion through the SEI. The understanding of Li diffusion mechanism and its energetics

through the SEI is of imperative importance to understand and improve the performance of Li batteries. For that reason, this work provides a detailed investigation on different aspects of Li atoms diffusion through the GB of the SEI. A series of NEB calculations are performed to evaluate the migration barrier of Li for different diffusion paths. Using these values the diffusion coefficients through the grain boundaries of these structures are evaluated and compared against the available data in literature for corresponding grains.

This critical insight can further be utilized in mesoscale modeling frameworks such as the phase-field model (PFM) to understand the diffusion, electrodeposition and stress generation through the grained structure SEI. The stability and the mechanical behavior of the SEI/Li interface is also analysed to calculate the interfacial energy and work of adhesion of each interfaces and quantify the energy required to cleave these interfaces due to dendrite nucleation. Since little is known about the actual structure and configuration of the GB in the SEI of operating cells, the presently investigated GB for the Li diffusion and stability might be simpler than the real-cell structures. For example, numerous defects and/or impurities could exist in the local structure of the SEI, which could potentially influence Li diffusivity. In addition, there are other external factors that could influence Li diffusivity in the SEI, such as an applied electric field and temperature. However, it is expected that these external factors would influence Li diffusion through the GB in the same way as through the respective grains.

Beyond the modeling insights and the extension of these modeling frameworks to mesoscale, these simulations also provide valuable insights to engineer the SEI with high strength, good

stability, and desirable Li mobility. The modeling results suggest that Li diffusion through GBs are faster than the bulk of the grains in SEI. If the SEI layers could be engineered to have smaller grain structures, the GB surface area is increased significantly. This leads to one of the most promising approaches in mitigating the dendritic growth in lithium anode and induce the uniform deposition of lithium. However, this could lead to concerns of stability, since the GBs are the weak spots in SEI and could be the probable locations of failure on the Li surface. In order to effectively control this phenomena, a fluorine rich SEI (LiF/LiF and LiF/Li<sub>2</sub>O) could be engineered on the surface of Li.

Although the relatively low DFT computational cost using 200-300 atoms GB configuration enables broad range of parametric studies that could suggest new and/or improved strategies to prevent Li dendrite formation and growth, these theories have to be tested experimentally. With the growth in experimental techniques such as cryo-TEM [96, 97], it will certainly be possible to extract some of these information and also test the theories that are drawn from the current research.

It is also common in the higher hierarchy cell-level models to represent the SEI as a constant resistance ignoring its chemistry and transport properties. However, incorporating the details of the ion diffusion and the detailed SEI chemistry into battery cell-level models, in a more fundamental manner, could enable the profound investigation of the SEI influence on battery performance and efficiency. Thus, the results from the present work, in addition to revealing the diffusion mechanism and the dendrite nucleation and growth mechanism of Li in the GB of the SEI, is a step forward towards more robust cell models and future efforts could be di-

rected towards utilizing these physics based models to identify more realistic parameters for cell level degradation studies.

## APPENDICES

## Appendix A

### PERMISSION TO USE JOURNAL ARTICLES

Ramasubramanian, A., Yurkiy, V., Najafi, A., Khounsary, A., Shahbazian-Yassar, R., Mashayek, F. "A Comparative Study on Continuum-Scale Modeling of Elasto-Plastic Deformation in Rechargeable Ion Batteries", *J. Electrochem. Soc.*



# Order Confirmation

Thank you, your order has been placed. An email confirmation has been sent to you. Your order license details and printable licenses will be available within 24 hours. Please access Manage Account for final order details.

This is not an invoice. Please go to manage account to access your order history and invoices.

## CUSTOMER INFORMATION

Payment by invoice: You can cancel your order until the invoice is generated by contacting customer service.

### Billing Address

Mr. AJAYKRISHNA RAMASUBARAMANIAN  
842 W Taylor St  
Chicago, IL 60607  
United States  
  
+1 (312) 478-9273  
aramas9@uic.edu

### Customer Location

Mr. AJAYKRISHNA RAMASUBARAMANIAN  
842 W Taylor St  
Chicago, IL 60607  
United States

### PO Number (optional)

N/A

### Payment options

Invoice

## PENDING ORDER CONFIRMATION

Confirmation Number: Pending

Order Date: 03-May-2020

### 1. Journal of the Electrochemical Society

0.00 USD

Order license ID	Pending	Publisher	Electrochemical Society	Special Terms Apply
ISSN	1945-7111	Portion	Chapter/article	
Type of Use	Republish in a thesis/dissertation			

### LICENSED CONTENT

Publication Title	Journal of the Electrochemical Society	Country	United States of America
Author/Editor	Electrochemical Society.	Rightholder	IOP Publishing, Ltd
Date	12/31/1947	Publication Type	e-Journal
Language	English	URL	http://www.scitation.org/JES

## REQUEST DETAILS

Portion Type	Chapter/article	Rights Requested	Main product
Page range(s)	A3418-A3425	Distribution	United States
Total number of pages	8	Translation	Original language of publication
Format (select all that apply)	Print	Copies for the disabled?	No
Who will republish the content?	Academic institution	Minor editing privileges?	Yes
Duration of Use	Life of current edition	Incidental promotional use?	No
Lifetime Unit Quantity	Up to 499	Currency	USD

## NEW WORK DETAILS

Title	Multi-scale Modeling of Rechargeable Ion Batteries	Institution name	University of Illinois at Chicago
Instructor name	Farzad Mashayek	Expected presentation date	2020-05-15

## ADDITIONAL DETAILS

Order reference number	N/A	The requesting person / organization to appear on the license	AJAYKRISHNA RAMASUBRAMANIAN
------------------------	-----	---	-----------------------------

## REUSE CONTENT DETAILS

Title, description or numeric reference of the portion(s)	Journal of Electrochemical Society	Title of the article/chapter the portion is from	A Comparative Study on Continuum-Scale Modeling of Elasto-Plastic Deformation in Rechargeable Ion Batteries
Editor of portion(s)	Ajaykrishna Ramasubramanian, Vitaliy Yurkiv, Ali Najafi, Ali Khounsary, Reza Shahbazian-Yassar, Farzad Mashayek	Author of portion(s)	Ajaykrishna Ramasubramanian, Vitaliy Yurkiv, Ali Najafi, Ali Khounsary, Reza Shahbazian-Yassar, Farzad Mashayek
Volume of serial or monograph	164	Issue, if republishing an article from a serial	N/A
Page or page range of portion	A3418- A3425	Publication date of portion	2017-11-07

## PUBLISHER TERMS AND CONDITIONS

These special terms and conditions are in addition to the standard terms and conditions for CCC's Republication Service and, together with those standard terms and conditions, govern the use of the Works. As the User you will make all reasonable efforts to contact the author(s) of the article which the Work is to be reused from, to seek consent for your intended use. Contacting one author who is acting expressly as authorised agent for their co-author(s) is acceptable. User will reproduce the following wording prominently alongside the Work: the source of the Work, including author, article title, title of journal, volume number, issue number (if relevant), page range (or first page if this is the only information available) and date of first publication. This information can be contained in a footnote or reference note; and a link back to the article (via DOI); and if practicable, and IN ALL CASES for new works published under any of the Creative Commons licences, the words "© IOP Publishing. Reproduced with permission. All rights reserved" Without the express permission of the author(s) and the Rightsholder of the article from which the Work is to be reused, User shall not use it in any way which, in the opinion of the Rightsholder, could: (i) distort or alter the author(s)' original intention(s) and meaning; (ii) be prejudicial to the honour or reputation of the author(s); and/or (iii) imply endorsement by the author(s) and/or the Rightsholder. This licence does not apply to any article which is credited to another source and which does not have the copyright line '© IOP Publishing Ltd'. User must check the copyright line of the article from which the Work is to be reused to check that IOP Publishing Ltd has all the necessary rights to be able to grant permission. User is solely responsible for identifying and obtaining separate licences and permissions from the copyright owner for reuse of any such third party material/figures which the Rightsholder is not the copyright owner of. The Rightsholder shall not reimburse any fees which User pays for a republication license for such third party content. This licence does not apply to any material/figure which is credited to another source in the Rightsholder's publication or has been obtained from a third party. User must check the Version of Record of the article from which the Work is to be reused, to check whether any of the material in the Work is third party material. Third party citations and/or copyright notices and/or permissions statements may not be included in any other version of the article from which the Work is to be reused and so cannot be relied upon by the User. User is solely responsible for identifying and obtaining separate licences and permissions from the copyright owner for reuse of any such third party material/figures where the Rightsholder is not the copyright owner. The Rightsholder shall not reimburse any fees which User pays for a republication license for such third party content. User and CCC acknowledge that the Rightsholder may, from time to time, make changes or additions to these special terms and conditions without express notification, provided that these shall not apply to permissions already secured and paid for by User prior to such change or addition. User acknowledges that the Rightsholder (which includes companies within its group and third parties for whom it publishes its titles) may make use of personal data collected through the service in the course of their business. If User is the author of the Work, User may automatically have the right to reuse it under the rights granted back when User transferred the copyright in the article to the Rightsholder. User should check the copyright form and the relevant author rights policy to check whether permission is required. If User is the author of the Work and does require permission for proposed reuse of the Work, User should select 'Author of requested content' as the Requestor Type. The Rightsholder shall not reimburse any fees which User pays for a republication license. If User is the author of the article which User wishes to reuse in User's thesis or dissertation, the republication licence covers the right to include the Accepted Manuscript version (not the Version of Record) of the article. User must include citation details and, for online use, a link to the Version of Record of the article on the Rightsholder's website. User may need to obtain separate permission for any third party content included within the article. User must check this with the copyright owner of such third party content. User may not include the article in a thesis or dissertation which is published by ProQuest. Any other commercial use of User's thesis or dissertation containing the article would also need to be expressly notified in writing to the Rightsholder at the time of request and would require separate written permission from the Rightsholder. User does not need to request permission for Work which has been published under a CC BY licence. User must check the Version of Record of the CC BY article from which the Work is to be reused, to check whether any of the material in the Work is third party material and so not published under the CC BY licence. User is solely responsible for identifying and obtaining separate licences and permissions from the copyright owner for reuse of any such third party material/figures. The Rightsholder shall not reimburse any fees which User pays for such licences and permissions. As well as CCC, the Rightsholder shall have the right to bring any legal action that it deems necessary to enforce its rights should it consider that the Work infringes those rights in any way. For STM Signatories ONLY (as agreed as part of the STM Guidelines) Any licence granted for a particular edition of a Work will apply also to subsequent editions of it and for editions in other languages, provided such editions are for the Work as a whole in situ and do not involve the separate exploitation of the permitted illustrations or excerpts.

## PUBLISHER SPECIAL TERMS AND CONDITIONS

When you transferred the copyright in your article to the Electrochemical Society, you were granted back certain rights, including the right to include the Final Published Version of the article within any thesis or dissertation. Please note you may need to obtain separate permission for any third party content you included within your article. Please include citation details, "© The Electrochemical Society. Reproduced with permission. All rights reserved" and for online use, a link to the Version of Record. The only restriction is that if, at a later date, you wanted your thesis/dissertation to be published commercially, further permission would be required.

---

**Total Items: 1****Total Due: 0.00 USD**

---

Accepted: All Publisher and CCC Terms and Conditions

**Appendix A (Continued)**

Ramasubramanian, A., Yurkiv, V., Nie, A., Najafi, A., Khounsary, A., Shahbazian–Yassar, R., Mashayek, F. “A Numerical Study on Striped Lithiation of Tin Oxide Anodes”, *Int. J. Solids Struct.*, 2019, 159, 163–170.

**RightsLink®**

Home



Help



Email Support



Sign in



Create Account



### A numerical study on striped lithiation of tin oxide anodes

**Author:**

Ajaykrishna Ramasubramanian, Vitaliy Yurkiv, Anmin Nie, Ali Najafi, Ali Khounsary, Reza Shahbazian-Yassar, Farzad Mashayek

**Publication:** International Journal of Solids and Structures**Publisher:** Elsevier**Date:** 1 March 2019*Published by Elsevier Ltd.*

Please note that, as the author of this Elsevier article, you retain the right to include it in a thesis or dissertation, provided it is not published commercially. Permission is not required, but please ensure that you reference the journal as the original source. For more information on this and on your other retained rights, please visit: <https://www.elsevier.com/about/our-business/policies/copyright#Author-rights>

BACK

CLOSE WINDOW

**Appendix A (Continued)**

Ramasubramanian, A., Yurkiv, V., Foroozan, T., Ragone, M., Shahbazian-Yassar, R., Mashayek, F., “Lithium Diffusion Mechanism through Solid-Electrolyte Interphase (SEI) In Rechargeable Lithium Batteries”, *J. Phys. Chem. C*, 2019.

**RightsLink®**

Home



Help



Email Support



Sign in



Create Account

### Lithium Diffusion Mechanism through Solid-Electrolyte Interphase in Rechargeable Lithium Batteries

**Author:** Ajaykrishna Ramasubramanian, Vitaliy Yurkiv, Tara Foroozan, et al**Publication:** The Journal of Physical Chemistry C**Publisher:** American Chemical Society**Date:** Apr 1, 2019*Copyright © 2019, American Chemical Society*

#### PERMISSION/LICENSE IS GRANTED FOR YOUR ORDER AT NO CHARGE

This type of permission/license, instead of the standard Terms & Conditions, is sent to you because no fee is being charged for your order. Please note the following:

- Permission is granted for your request in both print and electronic formats, and translations.
- If figures and/or tables were requested, they may be adapted or used in part.
- Please print this page for your records and send a copy of it to your publisher/graduate school.
- Appropriate credit for the requested material should be given as follows: "Reprinted (adapted) with permission from (COMPLETE REFERENCE CITATION). Copyright (YEAR) American Chemical Society." Insert appropriate information in place of the capitalized words.
- One-time permission is granted only for the use specified in your request. No additional uses are granted (such as derivative works or other editions). For any other uses, please submit a new request.

[BACK](#)[CLOSE WINDOW](#)

## Appendix B

### DFT STRUCTURES

The following supplementary information provides details of the bulk crystal structure, the slabs of minimum energy surfaces, the hopping mechanism of Li diffusion through the GB structures and the additional DFT calculation resulting of atomic rearrangements due to the addition of Li in TPB structures.

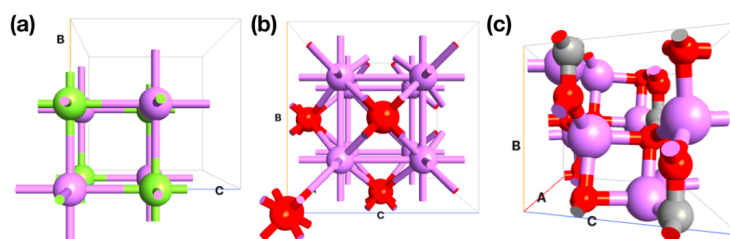


Figure 34. Bulk structures of individual components in the SEI. (a) LiF, (b) Li<sub>2</sub>O and (c) Li<sub>2</sub>CO<sub>3</sub> (Pink colored spheres depict Li atoms, red colored spheres show F atoms, and red colored spheres illustrate O atoms)

## Appendix B (Continued)

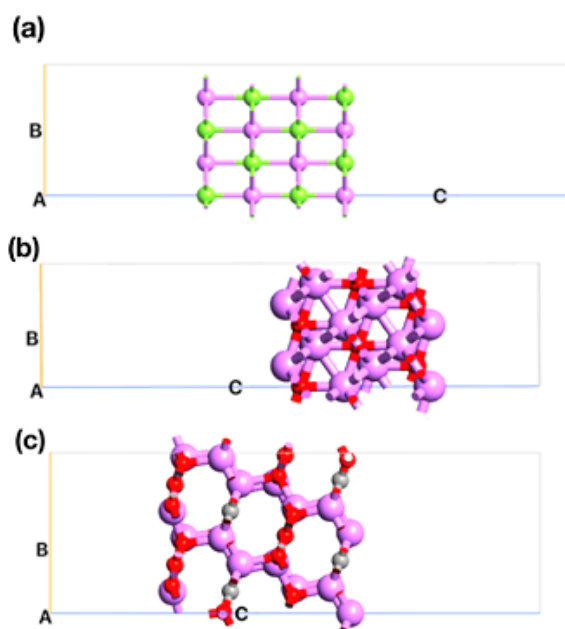


Figure 35. Vacuum slab structures of minimum energy surfaces: (a) LiF, (b) Li<sub>2</sub>O and (c) Li<sub>2</sub>CO<sub>3</sub> (Pink colored spheres depict Li atoms, red colored spheres show F atoms, and red colored spheres illustrate O atoms)

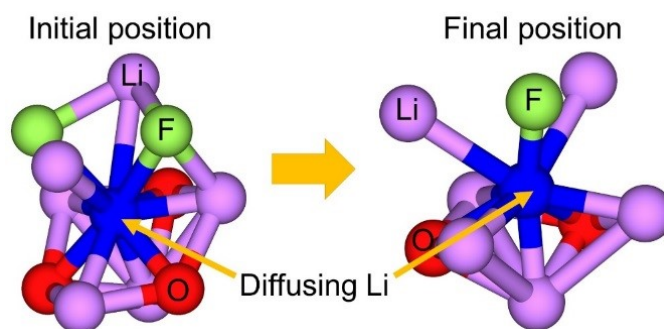


Figure 36. Multi-atom hopping mechanism of Li diffusion through the GB of LiF/Li<sub>2</sub>O.

## Appendix B (Continued)

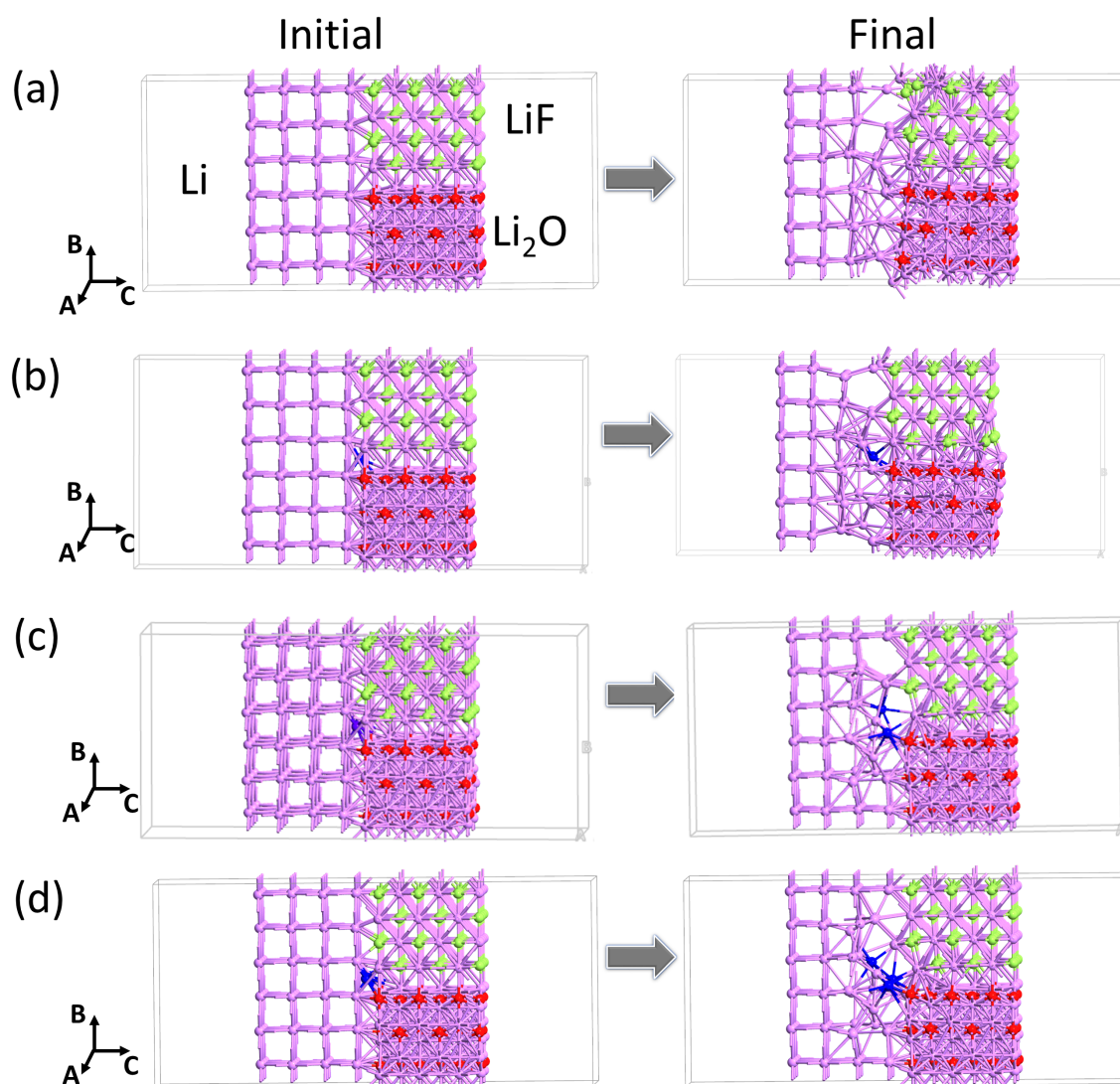


Figure 37. (a) Initial and final optimized structures of LiF/Li<sub>2</sub>O GB on Li surface with no added Li at the TPB. (b) Initial and final optimized structures of LiF/ Li<sub>2</sub>O GB on Li with one added Li at TPB. (c) Initial and final optimized structures of LiF/Li<sub>2</sub>O GB on Li with two added Li at TPB. (d) Initial and final optimized structures of LiF/Li<sub>2</sub>O GB on Li with two added Li at TPB. Pink colored spheres depict Li atoms; red-colored spheres show O atoms and green colored spheres show F atoms. The added Li atoms are shown in blue.

## Appendix B (Continued)

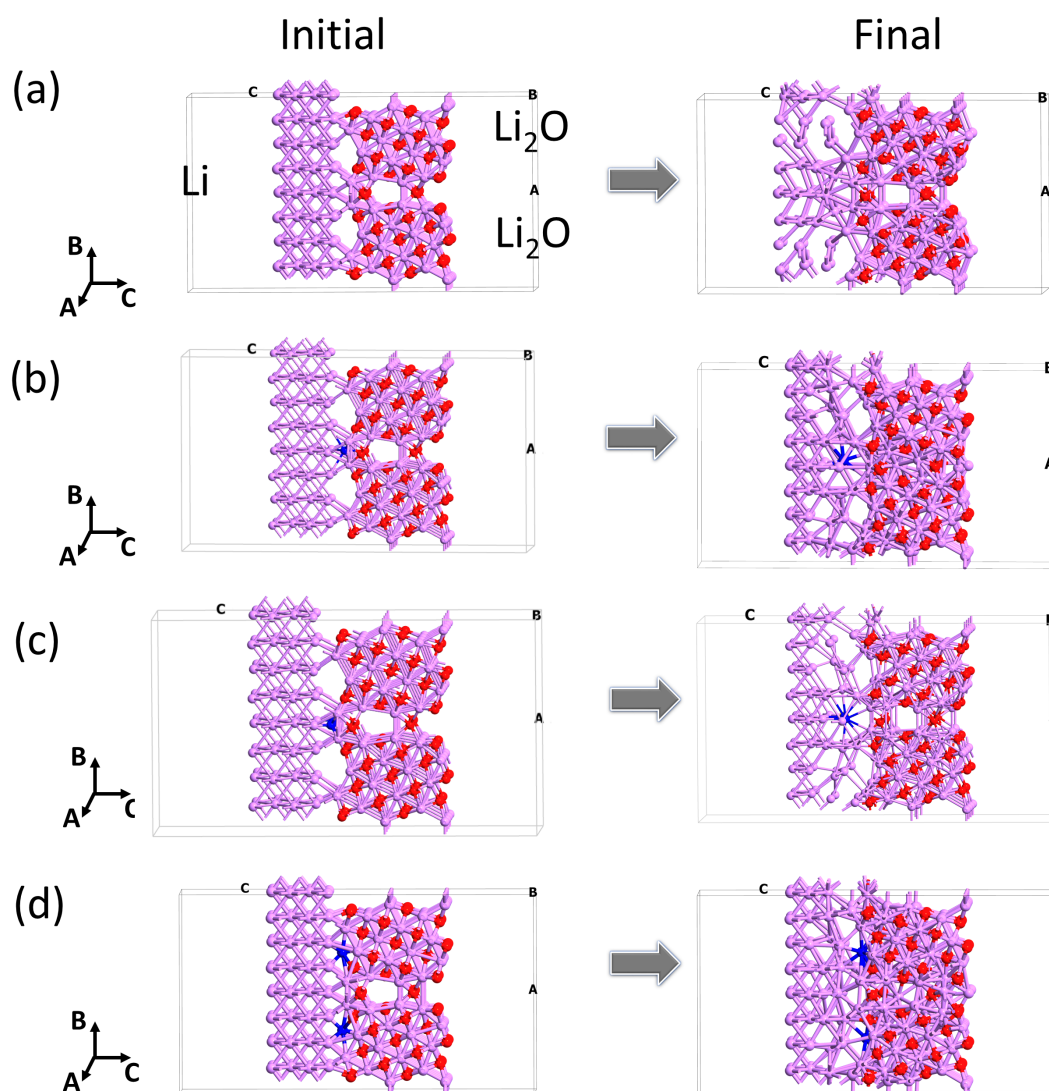


Figure 38. (a) Initial and final optimized structures of  $\text{Li}_2\text{O}/\text{Li}_2\text{O}$  GB on Li surface with no added Li atom at the TPB. (b) Initial and final optimized structures of  $\text{Li}_2\text{O}/\text{Li}_2\text{O}$  GB on Li with one added Li at TPB. (c) Initial and final optimized structures of  $\text{Li}_2\text{O}/\text{Li}_2\text{O}$  GB on Li with one added Li at TPB. (d) Initial and final optimized structures of  $\text{Li}_2\text{O}/\text{Li}_2\text{O}$  GB on Li with two added Li at other sites in the interphase. Pink colored spheres depict Li atoms, and red-colored spheres show O atoms. The added Li atoms are shown in blue.

## Appendix B (Continued)

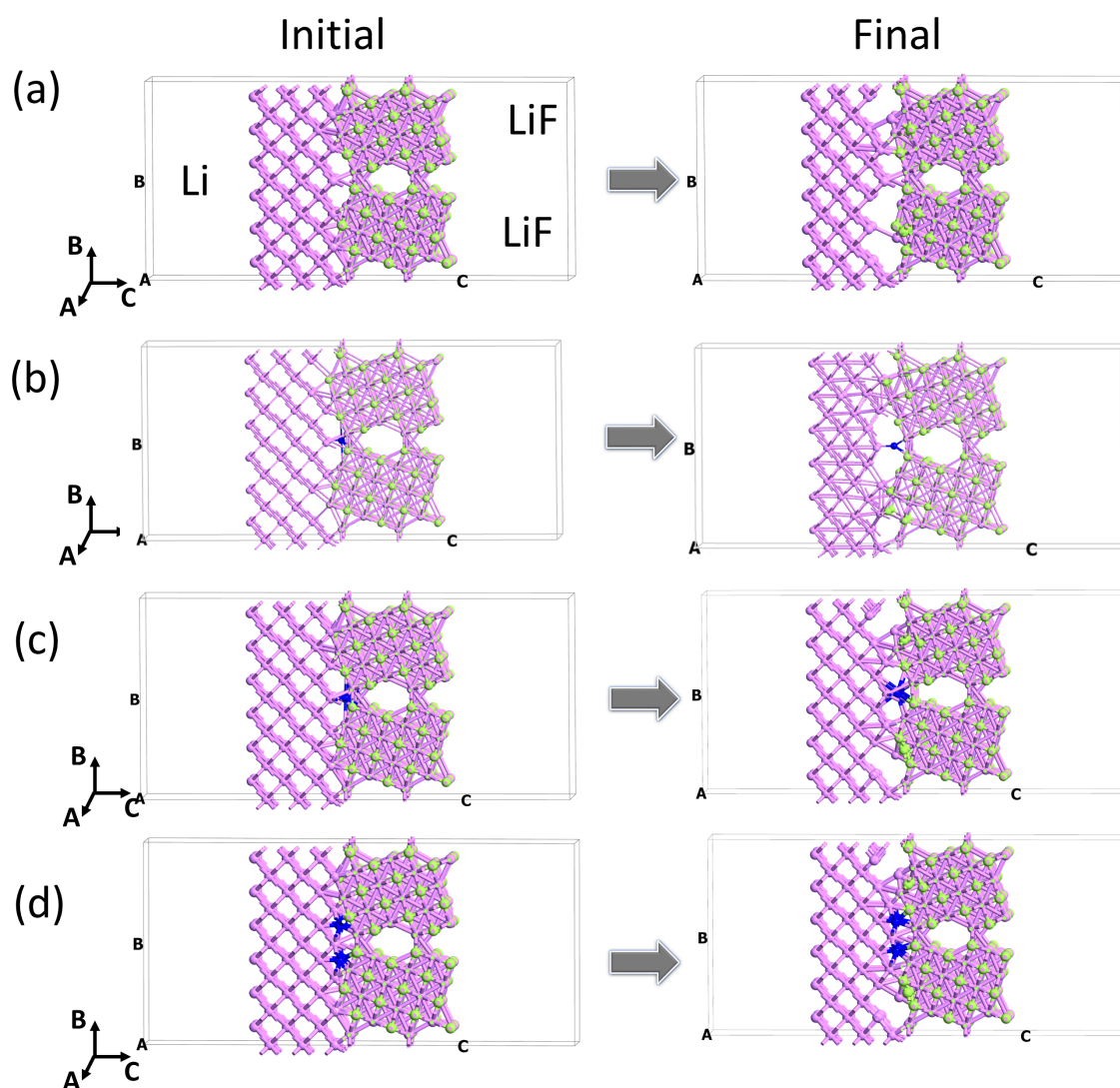


Figure 39. (a) Initial and final optimized structures of LiF/LiF GB on Li surface with no added Li at the TPB. (b) Initial and final optimized structures of LiF/LiF GB on Li with one added Li at TPB. (c) Initial and final optimized structures of LiF/LiF GB on Li with one added Li at TPB. (d) Initial and final optimized structures of LiF/LiF GB on Li with two added Li at other sites in the interphase. Pink colored spheres depict Li atoms, and green colored spheres show F atoms. The added Li atoms are shown in blue.

## Appendix C

## SAMPLE VASP INPUTS

Listing C.1. INCAR

```
1 # Basic setup:
2 SYSTEM = Li2O_compact
3 ISPIN = 1
4 LSORBIT = .FALSE. # not using Hubbard U
5 # Accuracy controls:
6 PREC = Accurate
7 ENCUT = 400
8 # Electronic loop controls:
9 ALGO = Normal # Normal (Davidson)
10 EDIFF = 0.000100
11 NELMIN = 2
12 NELM = 60
13 TIME = 0.400000
14 ISMEAR = 0 # Gaussian smearing
15 SIGMA = 0.200000 # eV
16 NBANDS = using default
17 # Relaxation control:
18 IBRION = 2 # Conjugate gradients
```

## Appendix C (Continued)

```
19 NSW = 100
20 POTIM = 0.500000
21 ISIF = 2      # Ions
22 EDIFFG = -0.010000
23 # Properties:
24 LCHARG = .FALSE.
25 LWAVE = .TRUE.
26 LELF = .FALSE.
27 LVTOT = .FALSE.
28 LVHAR = .FALSE.
29 # Custom options
30 NCORE=4
31 KPAR=1
```

## Listing C.2. KPOINTS

```
1 KPOINTS file
2 0
3 Gamma-centered
4 4 4 1
5 0 0 0
```

## Listing C.3. POSCAR

```
1 Li O
```

## Appendix C (Continued)

2	1.0			
3	6.588597131230	0.000000000000	0.000000000000	
4	-3.294298565620	5.705892490950	0.000000000000	
5	0.000000000000	0.000000000000	23.069350546100	
6	Li O			
7	24 12			
8	Selective dynamics			
9	Direct			
10	0.333333333333	0.166666666667	0.491773348149	F F F
11	0.500000000000	0.500000000000	0.783262212345	T T T
12	-0.000000000000	0.500000000000	0.783262212345	T T T
13	0.500000000000	0.000000000000	0.783262212345	T T T
14	0.000000000000	0.000000000000	0.783262212345	T T T
15	0.666666666667	0.833333333333	0.724964439506	T T T
16	0.166666666667	0.833333333333	0.724964439506	T T T
17	0.166666666667	0.333333333333	0.724964439506	T T T
18	0.833333333333	0.666666666667	0.666666666667	T T T
19	0.333333333333	0.666666666667	0.666666666667	T T T
20	0.833333333333	0.166666666667	0.666666666667	T T T
21	0.333333333333	0.166666666667	0.666666666667	T T T
22	0.666666666667	0.333333333333	0.724964439506	T T T
23	-0.000000000000	0.500000000000	0.608368893827	T T T
24	0.500000000000	0.000000000000	0.608368893827	T T T

## Appendix C (Continued)

25	0.000000000000	0.000000000000	0.608368893827	T T T
26	0.666666666667	0.833333333333	0.550071120988	F F F
27	0.166666666667	0.833333333333	0.550071120988	F F F
28	0.666666666667	0.333333333333	0.550071120988	F F F
29	0.166666666667	0.333333333333	0.550071120988	F F F
30	0.833333333333	0.666666666667	0.491773348149	F F F
31	0.333333333333	0.666666666667	0.491773348149	F F F
32	0.833333333333	0.166666666667	0.491773348149	F F F
33	0.500000000000	0.500000000000	0.608368893827	T T T
34	0.500000000000	0.000000000000	0.695815553086	T T T
35	0.000000000000	0.000000000000	0.695815553086	T T T
36	0.833333333333	0.666666666667	0.579220007408	T T T
37	0.333333333333	0.666666666667	0.579220007408	T T T
38	0.833333333333	0.166666666667	0.579220007408	T T T
39	0.166666666667	0.333333333333	0.462624461729	F F F
40	0.666666666667	0.833333333333	0.462624461729	F F F
41	0.166666666667	0.833333333333	0.462624461729	F F F
42	0.666666666667	0.333333333333	0.462624461729	F F F
43	-0.000000000000	0.500000000000	0.695815553086	T T T
44	0.333333333333	0.166666666667	0.579220007408	T T T
45	0.500000000000	0.500000000000	0.695815553086	T T T

## Appendix C (Continued)

Listing C.4. INCAR for NEB

```
1 # Basic setup:
2 SYSTEM = NEB.Li2O
3 ISPIN = 2
4 LSORBIT = .FALSE. # not using Hubbard U
5 # Accuracy controls:
6 PREC = Accurate
7 ENCUT = 400
8 # Electronic loop controls:
9 ALGO = Normal # Normal (Davidson)
10 EDIFF = 0.000100
11 NELMIN = 2
12 NELM = 60
13 TIME = 0.400000
14 ISMEAR = -4 # Tetrahedron method
15 # NBANDS - using default
16 # Relaxation control:
17 IBRION = 1 # Quasi-Newton (RMM-DIIS)
18 NSW = 100
19 POTIM = 0.500000
20 ISIF = 2 # Ions
21 EDIFFG = -0.010000
22 # NEB controls:
23 IMAGES = 5
```

## Appendix C (Continued)

```
24  SPRING = -5.000000
```

```
25  # Properties:
```

```
26  LCHARG = .FALSE.
```

```
27  LWAVE = .FALSE.
```

```
28  LELF = .FALSE.
```

```
29  LVTOT = .FALSE.
```

```
30  LVHAR = .FALSE.
```

## CITED LITERATURE

1. Chen, L., Fan, F., Hong, L., Chen, J., Ji, Y. Z., Zhang, S. L., Zhu, T., and Chen, L. Q.: A phase-field model coupled with large elasto-plastic deformation: Application to lithiated silicon electrodes. *Journal of The Electrochemical Society* , 161(11):F3164–F3172, 2014.
2. Annual energy outlook 2019-2020 url: <https://www.eia.gov/outlooks/aeo/>.
3. Peters, J. F., Baumann, M., Zimmermann, B., Braun, J., and Weil, M.: The environmental impact of li-ion batteries and the role of key parameters – a review. *Renewable and Sustainable Energy Reviews* , 67:491 – 506, 2017.
4. Whittingham, M. S.: Materials challenges facing electrical energy storage. *Mrs Bulletin* , 33(4):411–419, 2008.
5. Goodenough, J. B. and Kim, Y.: Challenges for rechargeable li batteries. *Chemistry of materials* , 22(3):587–603, 2009.
6. Tarascon, J.-M. and Armand, M.: Issues and challenges facing rechargeable lithium batteries. In *Materials For Sustainable Energy: A Collection of Peer-Reviewed Research and Review Articles from Nature Publishing Group* , pages 171–179. World Scientific, 2011.
7. Yamaki, J.: Secondary batteries – lithium rechargeable systems – lithium-ion — overview. In *Encyclopedia of Electrochemical Power Sources* , ed. J. Garche, pages 183 – 191. Amsterdam, Elsevier, 2009.
8. Thackeray, M. M., Thomas, J. O., and Whittingham, M. S.: Science and applications of mixed conductors for lithium batteries. *MRS Bulletin* , 25(3):39–46, 2000.
9. Shehzad, K., Xu, Y., Gao, C., and Duan, X.: Three-dimensional macro-structures of two-dimensional nanomaterials. *Chem. Soc. Rev.* , 45:5541–5588, 2016.
10. Magasinski, A., Dixon, P., Hertzberg, B., Kvit, A., Ayala, J., and Yushin, G.: High-performance lithium-ion anodes using a hierarchical bottom-up approach. *Nature materials* , 9(4):353–358, 2010.

11. Yin, J., Wada, M., Yamamoto, K., Kitano, Y., Tanase, S., and Sakai, T.: Micrometer-scale amorphous si thin-film electrodes fabricated by electron-beam deposition for li-ion batteries. *Journal of the Electrochemical Society* , 153(3):A472–A477, 2006.
12. Liu, J. and Xue, D.: Hollow nanostructured anode materials for li-ion batteries. *Nanoscale research letters* , 5(10):1525, 2010.
13. Huang, J. Y., Zhong, L., Wang, C. M., Sullivan, J. P., Xu, W., Zhang, L. Q., Mao, S. X., Hudak, N. S., Liu, X. H., Subramanian, A., Fan, H., Qi, L., Kushima, A., and Li, J.: In situ observation of the electrochemical lithiation of a single SnO<sub>2</sub> nanowire electrode. *Science* , 330(6010):1515–1520, dec 2010.
14. Li, J., Dozier, A. K., Li, Y., Yang, F., and Cheng, Y.-T.: Crack pattern formation in thin film lithium-ion battery electrodes. *Journal of The Electrochemical Society* , 158(6):A689–A694, 2011.
15. Peled, E.: Advanced model for solid electrolyte interphase electrodes in liquid and polymer electrolytes. *Journal of The Electrochemical Society* , 144(8):L208, 1997.
16. Peled, E., Menachem, C., Bartow, D., and Melman, A.: Improved graphite anode for lithium-ion batteries chemically bonded solid electrolyte interface and nanochannel formation. *Journal of The Electrochemical Society* , 143(1):L4–L7, 1996.
17. Pender, J. P., Jha, G., Youn, D. H., Ziegler, J. M., Andoni, I., Choi, E. J., Heller, A., Dunn, B. S., Weiss, P. S., Penner, R. M., and Mullins, C. B.: Electrode degradation in lithium-ion batteries. *ACS Nano* , 14(2):1243–1295, 2020. PMID: 31895532.
18. Beaulieu, L., Eberman, K., Turner, R., Krause, L., and Dahn, J.: Colossal reversible volume changes in lithium alloys. *Electrochemical and Solid-State Letters* , 4(9):A137–A140, 2001.
19. Chan, C. K., Peng, H., Liu, G., McIlwrath, K., Zhang, X. F., Huggins, R. A., and Cui, Y.: High-performance lithium battery anodes using silicon nanowires. *Nature nanotechnology* , 3(1):31, 2008.
20. Pedersen, A., Khomyakov, P. A., and Luisier, M.: The reversible lithiation of sno: a three-phase process. *arXiv preprint arXiv:1502.01110* , 2015.

21. Sethuraman, V. A., Chon, M. J., Shimshak, M., Srinivasan, V., and Guduru, P. R.: In situ measurements of stress evolution in silicon thin films during electrochemical lithiation and delithiation. *Journal of Power Sources* , 195(15):5062–5066, 2010.
22. Liu, X. H. and Huang, J. Y.: In situ tem electrochemistry of anode materials in lithium ion batteries. *Energy & Environmental Science* , 4(10):3844–3860, 2011.
23. Danner, T., Eswara, S., Schulz, V. P., and Latz, A.: Characterization of gas diffusion electrodes for metal-air batteries. *Journal of Power Sources* , 324:646–656, 2016.
24. Zhao, K., Tritsarlis, G. A., Pharr, M., Wang, W. L., Okeke, O., Suo, Z., Vlassak, J. J., and Kaxiras, E.: Reactive flow in silicon electrodes assisted by the insertion of lithium. *Nano letters* , 12(8):4397–4403, 2012.
25. Zhao, K., Pharr, M., Cai, S., Vlassak, J. J., and Suo, Z.: Large plastic deformation in high-capacity lithium-ion batteries caused by charge and discharge. *Journal of the American Ceramic Society* , 94:s226–s235, 2011.
26. Kang, M. K. and Huang, R.: A variational approach and finite element implementation for swelling of polymeric hydrogels under geometric constraints. *Journal of Applied Mechanics* , 77(6):061004, 2010.
27. Liu, X. H., Zheng, H., Zhong, L., Huang, S., Karki, K., Zhang, L. Q., Liu, Y., Kushima, A., Liang, W. T., Wang, J. W., et al.: Anisotropic swelling and fracture of silicon nanowires during lithiation. *Nano letters* , 11(8):3312–3318, 2011.
28. Yang, H., Fan, F., Liang, W., Guo, X., Zhu, T., and Zhang, S.: A chemo-mechanical model of lithiation in silicon. *Journal of the Mechanics and Physics of Solids* , 70:349–361, 2014.
29. Han, B., Van der Ven, A., Morgan, D., and Ceder, G.: Electrochemical modeling of intercalation processes with phase field models. *Electrochimica Acta* , 49(26):4691–4699, 2004.
30. Singh, G. K., Ceder, G., and Bazant, M. Z.: Intercalation dynamics in rechargeable battery materials: General theory and phase-transformation waves in lifepo4. *Electrochimica Acta* , 53(26):7599–7613, 2008.
31. Burch, D. and Bazant, M. Z.: Size-dependent spinodal and miscibility gaps for intercalation in nanoparticles. *Nano letters* , 9(11):3795–800, Nov 2009.

32. Wang, F.-M., Shieh, D.-T., Cheng, J.-H., and Yang, C.-R.: An investigation of the salt dissociation effects on solid electrolyte interface (sei) formation using linear carbonate-based electrolytes in lithium ion batteries. *Solid State Ionics* , 180(40):1660–1666, 2010.
33. De, S., Suthar, B., Rife, D., Sikha, G., and Subramanian, V. R.: Efficient reformulation of solid phase diffusion in electrochemical-mechanical coupled models for lithium-ion batteries: Effect of intercalation induced stresses. *Journal of The Electrochemical Society* , 160(10):A1675–A1683, 2013.
34. Peled, E.: The electrochemical behavior of alkali and alkaline earth metals in nonaqueous battery systems—the solid electrolyte interphase model. *Journal of The Electrochemical Society* , 126(12):2047, 1979.
35. Peled, E., Golodnttsky, D., Ardel, G., Menachem, C., Tow, D. B., and Eshkenazy, V.: The role of sei in lithium and lithium ion batteries. *MRS Proceedings* , 393, jan 1995.
36. Peled, E.: Improved graphite anode for lithium-ion batteries chemically. *Journal of The Electrochemical Society* , 143(1):L4, 1996.
37. Peled, E.: Advanced model for solid electrolyte interphase electrodes in liquid and polymer electrolytes. *Journal of The Electrochemical Society* , 144(8):L208, 1997.
38. Broussely, M., Biensan, P., Bonhomme, F., Blanchard, P., Herreyre, S., Nechev, K., and Staniewicz, R.: Main aging mechanisms in li ion batteries. *Journal of Power Sources* , 146(1-2):90–96, aug 2005.
39. Verma, P., Maire, P., and Novák, P.: A review of the features and analyses of the solid electrolyte interphase in li-ion batteries. *Electrochimica Acta* , 55(22):6332–6341, sep 2010.
40. Lu, M., Cheng, H., and Yang, Y.: A comparison of solid electrolyte interphase (SEI) on the artificial graphite anode of the aged and cycled commercial lithium ion cells. *Electrochimica Acta* , 53(9):3539–3546, mar 2008.
41. Ding, F., Xu, W., Graff, G. L., Zhang, J., Sushko, M. L., Chen, X., Shao, Y., Engelhard, M. H., Nie, Z., Xiao, J., Liu, X., Sushko, P. V., Liu, J., and Zhang, J.-G.: Dendrite-free lithium deposition via self-healing electrostatic shield mechanism. *Journal of the American Chemical Society* , 135(11):4450–4456, mar 2013.

42. Benitez, L., Cristancho, D., Seminario, J., de la Hoz, J. M., and Balbuena, P.: Electron transfer through solid-electrolyte-interphase layers formed on si anodes of li-ion batteries. *Electrochimica Acta* , 140:250–257, sep 2014.
43. Soto, F. A., Marzouk, A., El-Mellouhi, F., and Balbuena, P. B.: Understanding ionic diffusion through SEI components for lithium-ion and sodium-ion batteries: Insights from first-principles calculations. *Chemistry of Materials* , 30(10):3315–3322, apr 2018.
44. Liu, Z., Qi, Y., Lin, Y. X., Chen, L., Lu, P., and Chen, L. Q.: Interfacial study on solid electrolyte interphase at li metal anode: Implication for li dendrite growth. *Journal of The Electrochemical Society* , 163(3):A592–A598, 2016.
45. Chen, Y. C., Ouyang, C. Y., Song, L. J., and Sun, Z. L.: Electrical and lithium ion dynamics in three main components of solid electrolyte interphase from density functional theory study. *The Journal of Physical Chemistry C* , 115(14):7044–7049, mar 2011.
46. Yildirim, H., Kinaci, A., Chan, M. K. Y., and Greeley, J. P.: First-principles analysis of defect thermodynamics and ion transport in inorganic SEI compounds: LiF and NaF. *ACS Applied Materials & Interfaces* , 7(34):18985–18996, aug 2015.
47. Christensen, J. and Newman, J.: A mathematical model for the lithium-ion negative electrode solid electrolyte interphase. *Journal of The Electrochemical Society* , 151(11):A1977, 2004.
48. Leung, K. and Jungjohann, K. L.: Spatial heterogeneities and onset of passivation breakdown at lithium anode interfaces. *The Journal of Physical Chemistry C* , 121(37):20188–20196, sep 2017.
49. © ANSYS, I.: ANSYS, 2020.
50. Gaston, D. R., Permann, C. J., Peterson, J. W., Slaughter, A. E., Andrs, D., Wang, Y., Short, M. P., Perez, D. M., Tonks, M. R., Ortensi, J., Zou, L., and Martineau, R. C.: Physics-based multiscale coupling for full core nuclear reactor simulation. *Annals of Nuclear Energy* , 84:45–54, 2014.
51. Gaston, D. R., Peterson, J. W., Permann, C. J., Andrs, D., Slaughter, A. E., and Miller, J. M.: Continuous integration for concurrent computational framework and application development. *Journal of Open Research Software* , 2(1):1–6, 2014.

52. Yurkiv, V., Gutiérrez-Kolar, J. S., Unocic, R. R., Ramsubramanian, A., Shahbazian-Yassar, R., and Mashayek, F.: Competitive ion diffusion within grain boundary and grain interiors in polycrystalline electrodes with the inclusion of stress field. *Journal of The Electrochemical Society* , 164(12):A2830–A2839, 2017.
53. Ramasubramanian, A., Yurkiv, V., Najafi, A., Khounsary, A., Shahbazian-Yassar, R., and Mashayek, F.: A comparative study on continuum-scale modeling of elastoplastic deformation in rechargeable ion batteries. *Journal of The Electrochemical Society* , 164(13):A3418, 2017.
54. Jand, S. P. and Kaghazchi, P.: The role of electrostatic effects in determining the structure of LiF-graphene interfaces. *Journal of Physics: Condensed Matter* , 26(26):262001, may 2014.
55. Hohenberg, P. and Kohn, W.: Inhomogeneous electron gas. *Phys. Rev.* , 136:B864–B871, Nov 1964.
56. Perdew, J. P., Burke, K., and Ernzerhof, M.: Generalized gradient approximation made simple. *Physical Review Letters* , 77(18):3865–3868, oct 1996.
57. Perdew, J. P., Ruzsinszky, A., Csonka, G. I., Vydrov, O. A., Scuseria, G. E., Constantin, L. A., Zhou, X., and Burke, K.: Restoring the density-gradient expansion for exchange in solids and surfaces. *Physical Review Letters* , 100(13), apr 2008.
58. Blöchl, P. E.: Projector augmented-wave method. *Physical Review B* , 50(24):17953–17979, dec 1994.
59. Henkelman, G., Uberuaga, B. P., and Jónsson, H.: A climbing image nudged elastic band method for finding saddle points and minimum energy paths. *The Journal of Chemical Physics* , 113(22):9901–9904, dec 2000.
60. Mouhat, F. and Coudert, F.-X.: Necessary and sufficient elastic stability conditions in various crystal systems. *Physical Review B* , 90(22):224104, 2014.
61. Yu, R., Zhu, J., and Ye, H.: Calculations of single-crystal elastic constants made simple. *Computer physics communications* , 181(3):671–675, 2010.
62. Chang, S., Moon, J., and Cho, M.: Stress-diffusion coupled multiscale analysis of si anode for li-ion battery. *Journal of Mechanical Science and Technology* , 29(11):4807–4816, 2015.

63. Wang, M., Xiao, X., and Huang, X.: Study of lithium diffusivity in amorphous silicon via finite element analysis. *Journal of Power Sources* , 307:77 – 85, 2016.
64. Hüger, E. and Schmidt, H.: Lithium permeability increase in nanosized amorphous silicon layers. *The Journal of Physical Chemistry C* , 122(50):28528–28536, 2018.
65. Zhang, L., Liu, Y., Key, B., Trask, S. E., Yang, Z., and Lu, W.: Silicon nanoparticles: Stability in aqueous slurries and the optimization of the oxide layer thickness for optimal electrochemical performance. *ACS Applied Materials & Interfaces* , 9(38):32727–32736, 2017. PMID: 28853282.
66. Nie, A., Gan, L.-Y., Cheng, Y., Asayesh-Ardakani, H., Li, Q., Dong, C., Tao, R., Mashayek, F., Wang, H.-T., Schingenogal, U., et al.: Atomic scale observation of lithiation reaction front in nanoscale  $\text{SnO}_2$  materials. *Acs Nano* , 7(7):6203–6211, 2013.
67. Huang, J. Y., Zhong, L., Wang, C. M., Sullivan, J. P., Xu, W., Zhang, L. Q., Mao, S. X., Hudak, N. S., Liu, X. H., Subramanian, A., et al.: In situ observation of the electrochemical lithiation of a single  $\text{SnO}_2$  nanowire electrode. *Science* , 330(6010):1515–1520, 2010.
68. Zhong, L., Liu, X. H., Wang, G. F., Mao, S. X., and Huang, J. Y.: Multiple stripe lithiation mechanism of individual  $\text{SnO}_2$  nanowires in a flooding geometry. *Physical review letters* , 106(24):248302, 2011.
69. Gwak, Y., Moon, J., and Cho, M.: Multi-scale analysis of an electrochemical model including coupled diffusion, stress, and nonideal solution in a silicon thin film anode. *Journal of Power Sources* , 307:856 – 865, 2016.
70. Haftbaradaran, H., Song, J., Curtin, W., and Gao, H.: Continuum and atomistic models of strongly coupled diffusion, stress, and solute concentration. *Journal of Power Sources* , 196(1):361 – 370, 2011.
71. Liu, X. H., Zheng, H., Zhong, L., Huang, S., Karki, K., Zhang, L. Q., Liu, Y., Kushima, A., Liang, W. T., Wang, J. W., Cho, J.-H., Epstein, E., Dayeh, S. A., Picraux, S. T., Zhu, T., Li, J., Sullivan, J. P., Cumings, J., Wang, C., Mao, S. X., Ye, Z. Z., Zhang, S., and Huang, J. Y.: Anisotropic swelling and fracture of silicon nanowires during lithiation. *Nano Letters* , 11(8):3312–3318, aug 2011.

72. Yang, H., Fan, F., Liang, W., Guo, X., Zhu, T., and Zhang, S.: A chemo-mechanical model of lithiation in silicon. *Journal of the Mechanics and Physics of Solids* , 70:349–361, oct 2014.
73. Aziz, M. J., Sabin, P. C., and Lu, G.-Q.: The activation strain tensor: Nonhydrostatic stress effects on crystal-growth kinetics. *Physical Review B* , 44(18):9812–9816, nov 1991.
74. Haftbaradaran, H., Song, J., Curtin, W., and Gao, H.: Continuum and atomistic models of strongly coupled diffusion, stress, and solute concentration. *Journal of Power Sources* , 196(1):361–370, 2011.
75. Guan, C., Wang, X., Zhang, Q., Fan, Z., Zhang, H., and Fan, H. J.: Highly stable and reversible lithium storage in  $\text{SnO}_2$  nanowires surface coated with a uniform hollow shell by atomic layer deposition. *Nano letters* , 14(8):4852–4858, 2014.
76. Simon, G. K. and Goswami, T.: Improving anodes for lithium ion batteries. *Metallurgical and Materials Transactions A* , 42(1):231–238, 2011.
77. Zhang, L. Q., Liu, X. H., Liu, Y., Huang, S., Zhu, T., Gui, L., Mao, S. X., Ye, Z. Z., Wang, C. M., Sullivan, J. P., et al.: Controlling the lithiation induced strain and charging rate in nanowire electrodes by coating. *Acs Nano* , 5(6):4800–4809, 2011.
78. Ansys: Academic research mechanical, release 17.2.
79. Radin, M. D., Rodriguez, J. F., Tian, F., and Siegel, D. J.: Lithium peroxide surfaces are metallic, while lithium oxide surfaces are not. *Journal of the American Chemical Society* , 134(2):1093–1103, 2012. PMID: 22148314.
80. Jand, S. P. and Kaghazchi, P.: The role of electrostatic effects in determining the structure of  $\text{LiF}$ -graphene interfaces. *Journal of Physics: Condensed Matter* , 26(26):262001, 2014.
81. Bruno, M. and Prencipe, M.: Ab initio quantum-mechanical modeling of the  $(0\ 0\ 1)$ ,  $(1\ \bar{1}\ 0)$  and  $(1\ 1\ 0)$  surfaces of zabuyelite ( $\text{Li}_2\text{CO}_3$ ). *Surface science* , 601(14):3012–3019, 2007.
82. Nie, M., Chalasani, D., Abraham, D. P., Chen, Y., Bose, A., and Lucht, B. L.: Lithium ion battery graphite solid electrolyte interphase revealed by microscopy and spectroscopy. *The Journal of Physical Chemistry C* , 117(3):1257–1267, 2013.

83. Guan, P., Liu, L., and Lin, X.: Simulation and experiment on solid electrolyte interphase (sei) morphology evolution and lithium-ion diffusion. *Journal of The Electrochemical Society* , 162(9):A1798–A1808, 2015.
84. Zhang, J., Wang, R., Yang, X., Lu, W., Wu, X., Wang, X., Li, H., and Chen, L.: Direct observation of inhomogeneous solid electrolyte interphase on mmo anode with atomic force microscopy and spectroscopy. *Nano letters* , 12(4):2153–2157, 2012.
85. Jang, J. I., Lee, J. E., Kim, B.-S., Park, S.-D., and Lee, H. S.: Twinning and its formation mechanism in a binary mg<sub>2</sub>si thermoelectric material with an anti-fluorite structure. *RSC Advances* , 7(35):21671–21677, 2017.
86. Kim, H. and Windl, W.: Efficient ab-initio calculation of the elastic properties of nanocrystalline silicon. *Journal of Computational and Theoretical Nanoscience* , 4(1):65–70, 2007.
87. Chen, Y., Ouyang, C., Song, L., and Sun, Z.: Electrical and lithium ion dynamics in three main components of solid electrolyte interphase from density functional theory study. *The Journal of Physical Chemistry C* , 115(14):7044–7049, 2011.
88. Liu, Z., Qi, Y., Lin, Y., Chen, L., Lu, P., and Chen, L.: Interfacial study on solid electrolyte interphase at li metal anode: implication for li dendrite growth. *Journal of The Electrochemical Society* , 163(3):A592–A598, 2016.
89. Yildirim, H., Kinaci, A., Chan, M. K., and Greeley, J. P.: First-principles analysis of defect thermodynamics and ion transport in inorganic sei compounds: Lif and naf. *ACS applied materials & interfaces* , 7(34):18985–18996, 2015.
90. Fan, L., Zhuang, H. L., Gao, L., Lu, Y., and Archer, L. A.: Regulating li deposition at artificial solid electrolyte interphases. *Journal of Materials Chemistry A* , 5(7):3483–3492, 2017.
91. Koyama, Y., Yamada, Y., Tanaka, I., Nishitani, S. R., Adachi, H., Murayama, M., and Kanno, R.: Evaluation of migration energy of lithium ions in chalcogenides and halides by first principles calculation. *Materials Transactions* , 43(7):1460–1463, 2002.
92. Tasaki, K., Goldberg, A., Lian, J.-J., Walker, M., Timmons, A., and Harris, S. J.: Solubility of lithium salts formed on the lithium-ion battery negative electrode sur-

- face in organic solvents. *Journal of The Electrochemical Society* , 156(12):A1019–A1027, 2009.
93. Tikekar, M. D., Choudhury, S., Tu, Z., and Archer, L. A.: Design principles for electrolytes and interfaces for stable lithium-metal batteries. *Nature Energy* , 1(9):16114, 2016.
94. Xu, W., Wang, J., Ding, F., Chen, X., Nasybulin, E., Zhang, Y., and Zhang, J.-G.: Lithium metal anodes for rechargeable batteries. *Energy Environ. Sci.* , 7:513–537, 2014.
95. Leung, K. and Jungjohann, K. L.: Spatial heterogeneities and onset of passivation breakdown at lithium anode interfaces. *The Journal of Physical Chemistry C* , 121(37):20188–20196, 2017.
96. Zachman, M. J., Tu, Z., Choudhury, S., Archer, L. A., and Kourkoutis, L. F.: Cryo-stem mapping of solid–liquid interfaces and dendrites in lithium-metal batteries. *Nature* , 560(7718):345–349, 2018.
97. Li, Y., Li, Y., Pei, A., Yan, K., Sun, Y., Wu, C.-L., Joubert, L.-M., Chin, R., Koh, A. L., Yu, Y., et al.: Atomic structure of sensitive battery materials and interfaces revealed by cryo–electron microscopy. *Science* , 358(6362):506–510, 2017.

## VITA

**Ajaykrishna Ramasubramanian**

709 S. Loomis St., Chicago, Illinois 60607

312-478-9273 | aramas9@uic.edu |

**EDUCATION**

---

**University of Illinois at Chicago**, College of Engineering, Chicago, IL  
Doctor of Philosophy in Mechanical Engineering,

**GPA: 3.66/4.00****Aug 2014 – Current**

**Amrita University**, Amrita School of Engineering, Coimbatore, India

Bachelor of Science in Mechanical Engineering,

**GPA: 8.62/10.00****May 2014****SKILLS**

---

**Programming:** C, C++, Python, Fortran, Octave**Libraries:** Keras, Numpy, Scikit-learn, Tensorflow, Pytorch**Platforms/Software:** ANSYS, SOLIDWORKS, ABAQUS, MOOSE (phase-field),COMSOL, VASP (*ab-initio* DFT), MATLAB/Simulink**PROFESSIONAL EXPERIENCE**

---

**Computational Multiphase Transport Laboratory, Chicago, IL**  
Research Assistant

**2015- Current**

- Developed a continuum scale model to simulate lithium-ion intercalation in battery anode materials and resulting degradation mechanisms using finite element solver.

- Modeled the stress evolution in different classes of electrode materials at particle and interphase levels during Li insertion.
- Analyzed the stability of electrode/electrolyte interfaces (SEI) using *ab-initio* density functional theory calculations and provided feedback to the experimentalists to identify potential nucleation sites for Li dendrites and degradation mechanisms in Li-ion battery anodes.
- Identified potential replacements in Li-ion battery anode materials for high energy density and power density applications.

#### **University of Illinois at Chicago, Chicago, IL**

##### **Teaching Assistant**

**2015- Current**

- Designed the ANSYS labs and training materials on structural mechanics, fluid dynamics, steady-state and transient thermal analysis and fluid-structure interaction for the senior year students in preparation for their senior year capstone projects.
- Hired by the department of mechanical engineering as a summer teaching assistant (addnl. appointment) to train all the incoming teaching assistants and interested faculties on ANSYS Mechanical and ANSYS Fluent and add it into the curriculum.
- Trained almost 300 students on ANSYS Mechanical and ANSYS Fluent packages in their senior year.

- Mentored and assisted more than 30 student groups with their senior design projects in simulation-driven design using ANSYS in various physics domains such as structural mechanics, thermal, fluid mechanics, electrochemistry, and explicit dynamics.

## **ACADEMIC PROJECTS**

---

### **Fundamental Understanding of SEI Effects on Li Dendrite Formation and Growth**

- Developed a fundamental understanding of dendrite formation and growth mechanism at the surface of Li metal anodes under the influence of the SEI to enable the design of growth prevention mechanisms.

### **Physical Multi-Scale Modelling of Rechargeable Energy Storage Technologies**

- Developed a fundamental understanding of the chemo- mechanics involved in the ion transport through the high energy density electrode materials both at the particle level and at the interphase level through numerical frameworks.

### **Plastic Recovery and Self-Healing in Longitudinally Twinned SiGe Nanowires**

- Developed a Finite element model using ANSYS to capture the plastic recovery in lamellar twinned nanowires and analyzed how dislocations are blocked by twin boundaries.

### **Battery Thermal Management Strategies and Real-time State of Charge Estimation for Electric Vehicle Application**

- Developed a COMSOL live-link model using MATLAB Simulink to monitor the temperature and State of Charge of the batteries under different drive cycles.

**SELECTED PUBLICATIONS**

---

- **Ramasubramanian, A.**, Yurkiv, V., Foroozan, T., Ragone, M., Shahbazian-Yassar, R., Mashayek, F. Lithium Diffusion Mechanism through Solid–Electrolyte Interphase in Rechargeable Lithium Batteries. *J. Phys. Chem. C*, 123 (16), 10237–10245 (2019).
- Shikder, M. R. A., **Ramasubramanian, A.**, Maksud, M., Yurkiv, V., Yoo, J., Harris, C. T., Subramanian, A. Plastic recovery and self-healing in longitudinally twinned SiGe nanowires. *Nanoscale*, 11(18), 8959-8966 (2019).
- Yurkiv, V., Foroozan, T., **Ramasubramanian, A.**, Shahbazian-Yassar, R., Mashayek, F. The influence of stress field on Li electrodeposition in Li–metal battery. *MRS Communications*, 8(3), 1380-1380, (2018)
- Yurkiv, V., Foroozan, T., **Ramasubramanian, A.**, Shahbazian-Yassar, R. Mashayek, F. Phase-field modeling of solid electrolyte interface (SEI) influence on Li dendritic behavior. *Electrochem. Acta*, 265, 609–619 (2018).
- **Ramasubramanian, A.**, Yurkiv, V., Nie, A., Najafi, A., Khounsary, A., Shahbazian–Yassar, R., Mashayek, F. A numerical study on striped lithiation of tin oxide anodes. *Int. J. Solids Struct.* (2018).
- Yurkiv, V., Gutiérrez-Kolar, J. S., Unocic, R. R., **Ramsubramanian, A.**, Shahbazian-Yassar, R., & Mashayek, F. Competitive ion diffusion within grain boundary and grain interiors in polycrystalline electrodes with the inclusion of stress field. *J. Electrochem. Soc.*, 164(12), A2830-A2839 (2017).

- Yurkiv, V., Sharifi-Asl, S., **Ramasubramanian, A.**, Shahbazian-Yassar, R., & Mashayek, F. Oxygen evolution and phase transformation in LCO cathode: A phase-field modeling study. *Comp. Mat. Sci.*, 140, 299-306 (2017).
- **Ramasubramanian, A.**, Yurkiv, V., Najafi, A., Khounsary, A., Shahbazian-Yassar, R., Mashayek, F. A Comparative Study on Continuum-Scale Modeling of Elasto-Plastic Deformation in Rechargeable Ion Batteries. *J. Electrochem. Soc.* 164, A3418–A3425 (2017).

## **SYNERGISTIC ACTIVITIES**

---

### **Supercomputing**

- Co-Principal investigator in an NSF allocation on XSEDE Bridges and Comet supercomputing facility **TG-DMR180106**
- Experience with University of Illinois at Chicago supercomputing facility named “Dragon” and “Extreme” (2016- Current).

### **Honors and Awards:**

- B.S. Murthy Award for Outstanding Student Paper given by SAEINDIA (2013-14)
- Best Undergraduate Research Project Award presented by Indian Society for Technical Education, 2014.